DISSERTATIONES
PHYSICAE
UNIVERSITATIS
TARTUENSIS
103

ARTUR TAMM

High entropy alloys: study of structural properties and irradiation response

DISSERTATIONES PHYSICAE UNIVERSITATIS TARTUENSIS

103

DISSERTATIONES PHYSICAE UNIVERSITATIS TARTUENSIS
103

ARTUR TAMM

High entropy alloys: study of structural properties and irradiation response

UNIVERSITY OF TARTU
Press

This study was carried out at the Institute of Technology, University of Tartu, Estonia.

The dissertation was admitted on 10^{th} of June 2016 in partial fulfilment of the requirements for the degree of Doctor of Philosophy in physics, and was allowed for defence by the Council of the Institute of Physics, University of Tartu.

Supervisors:	Prof. Alvo Aabloo, Institute of Technology, University of Tartu, Estonia
	Prof. Mattias Klintenberg, Department of Physics and Astronomy, Uppsala University, Sweden
Opponent:	Prof. Kai Nordlund, Division of Materials Physics, Department of Physics, Helsinki Institute of Physics, University of Helsinki, Finland

The public defence will take place on 22^{nd} of August 2016 in the Institute of Physics, University of Tartu, W. Ostwaldi Str. 1.

ISSN 1406-0647
ISBN 978-9949-77-181-3 (print)
ISBN 978-9949-77-182-0 (pdf)

Copyright: Artur Tamm, 2016

University of Tartu Press
www.tyk.ee

This thesis is dedicated to my father,
who passed away in March 2015.

Contents

Abstract 9

List of publications 11

Authors contribution 12

Abbreviations and symbols 13

1 Introduction 15
1.1 Purpose of this work 17

2 Concept of high entropy alloy 18

3 Computational methods in materials science 21
3.1 Density functional theory 21
3.1.1 Time-dependent density functional theory 23
3.2 Molecular dynamics 24
3.2.1 Empirical potentials 25
3.2.2 Langevin dynamics 26
3.2.3 Non-adiabatic molecular dynamics 27
3.3 Monte Carlo method 28

4 Construction of empirical potentials suitable for radiation damage simulations of HEA 30
4.1 General concept 30
4.2 Short-range behaviour 31
4.3 Future concepts 35

5 Atomic-scale structure and properties of Ni-based HEAs 36
5.1 General concept 36
5.2 Short-range order parameter 37
5.3 Chemical-ordering in Ni-based HEA 37
5.4 Future concepts 40

6 Electronic stopping in Ni and NiFe alloy 42
6.1 General concept 42
6.2 Stopping power 43
6.3 Electron-phonon coupling 44

6.4 TDDFT study of electronic stopping 46
6.5 EPH model for classical simulations 48
6.6 Future concepts 52

7 Conclusions 53

8 Acknowledgements 55

9 Summary in Estonian 56

References 59

Publications 67

Curriculum Vitae 107

Abstract

The materials used in the next-generation nuclear power plants have to endure extreme environmental conditions, such as high doses of radiation, high temperature, and corrosion. Therefore, scientists are searching for novel material concepts that could perform in these conditions. High entropy alloys are new materials which consist of five or more principal elements in near equimolar concentrations. Furthermore, the material forms a single phase solid solution. Experiments have shown that high entropy alloys have better mechanical properties compared to pure single elements they consist of, are corrosion resistant, and their properties are stable in wide temperature range.

The properties of high entropy alloys are affected by four core effects: high entropy, sluggish diffusion, severe lattice distortion, and cocktail effect. The high entropy effect stabilises the random solid solution phase and therefore affects the atomic-scale structure of the material. Next, sluggish diffusion effect can trap various point-defects and hinder their clustering into larger defects. The severe lattice distortion effect increases the electron and phonon scattering within the material which affects the thermal properties. Finally, cocktail effect allows to modify material properties based on the concentration of ingredients.

The properties of high entropy alloys make them suitable candidates for use in nuclear applications. Until now, the radiation damage in high entropy alloys has not been extensively studied. Computer simulations are necessary to study the radiation response of the material, due to fast processes involved which cannot be measured directly experimentally. These methods rely on both the models used as well as the initial conditions. In the current work three aspects of computer simulations are investigated that can affect the results of radiation damage simulations.

First, the short-range interaction is studied with quantum mechanical methods. Based on this a new method for modifying the empirical potentials is proposed to correctly capture the interactions at short interatomic distances. The results obtained from quantum mechanical methods show that at very short distances, less than 0.7 Å, Ziegler, Biersack, and Littmark potential agrees well with the Ni-Ni dimer energy in host crystal, but at the intermediate distances, 0.7 - 2.2 Å, the results differ. Therefore, the empirical potential has to be modified in order to reproduce the quantum mechanical results. For this purpose a procedure was developed and applied to the case of Ni embedded atom method type potential. The comparison simulations

with potentials developed with the new proposed method and a commonly used method show that the number of stable Frenkel pairs produced in the collision cascade simulation depends on the fitting parameters in the latter method, but is stable with the new method.

Secondly, the chemical ordering is studied in two high entropy alloys, NiCrCo and NiCrCoFe, with Monte Carlo simulations coupled with density functional theory. Simulations are done at 500, 800 and 1200 K to investigate the temperature dependence of the atomic distribution. During the simulation atomic species are swapped randomly and a new state is accepted with probability based on Metropolis method. The results from simulations of NiCrCo alloy show that the chemical ordering in the alloy changes from the random solid solution to a slightly ordered state. The number of Cr-Cr pairs is decreased and Ni-Cr pairs increased. Next, the results for quaternary NiCrCoFe alloy show a similar trend, where the number of Cr-Cr pairs is decreased, but the number of Fe-Fe pairs is also decreased. The main reason behind the ordering is the magnetic frustration of antiferromagnetic Cr atoms where it is energetically preferable to scatter Cr atoms within the material to sites where the neighbouring atoms have opposite magnetic moments.

Thirdly, the time-dependent density functional theory calculations are done to investigate the density dependent electron-ion coupling parameter for Ni and Fe projectiles in Ni host crystal. The simulations show that the coupling of Fe is stronger than for Ni. This would result in larger phonon scattering due to electrons when additional Fe atoms are introduced into the alloy. Next, a new method for including electronic effects into classical molecular dynamics simulation was developed for LAMMPS software package and applied to the study of phonon normal mode lifetimes in Ni crystal and NiFe random alloys. The method is based on Langevin dynamics where the friction term depends both on the electronic density as well as on the type of the atom. The phonon lifetimes obtained from the simulations for pure Ni crystal are in good agreement with the quantum mechanics based perturbation theory calculations. Moreover, the new method is a significant improvement compared to the two-temperature model where the lifetimes do not depend on the wave vector of phonon modes at all. The results for phonon mode lifetimes in NiFe random alloy rapidly decrease with the increase of Fe content. This is mainly due to the scattering of phonon modes caused by the introduced disorder, but also due to the higher coupling parameter for Fe atoms.

In summary, all the studied aspects can severely influence the results of collision cascade molecular dynamics simulations in high entropy alloys. Therefore, the proposed methods and calculated properties will provide valuable input for further studies.

List of publications

Basis publications:

I R. E. Stoller, A. Tamm, L. K. Beland, G. D. Samolyuk, G. M. Stocks, A. Caro, L. V. Slipchenko, Yu. N. Osetsky, A. Aabloo, M. Klintenberg, and Y. Wang, The Impact of Short-range Forces on Defect Production from High-energy Collisions, *Journal of Chemical Theory and Computation* **12**, 2871-2879 (2016).

II A. Tamm, A. Aabloo, M. Klintenberg, M. Stocks, and A. Caro, Atomic-scale properties of Ni-based FCC ternary, and quaternary alloys, *Acta Materiala* **99**, 307-312 (2015).

III A. Caro, A. A. Correa, A. Tamm, G. Samolyuk, and M. Stocks, Adequacy of damped dynamics to represent the electron-phonon interaction in solids, *Physical Review B* **92**, 144309 (2015).

IV A. Tamm, G. Samolyuk, A. A. Correa, M. Klintenberg, A. Aabloo, and A. Caro, The electron-phonon interaction within classical molecular dynamics, *Physical Review B* (2016) **accepted**.

Other publications:

- L. Bläckberg, E. Metsanurk, A. Tamm, A. Aabloo, and M. Klintenberg, Molecular dynamics study of Xenon on an amorphous Al_2O_3 surface, *Nuclear Instruments and Methods in Physics Research A* **759**, 10-15 (2014).
- E. Metsanurk, A. Tamm, A. Caro, A. Aabloo, and M. Klintenberg, First-principles study of point defects at a semicoherent interface, *Scientific Reports* **4**, 7567 (2014).
- A. Tamm, E. Metsanurk, A. Caro, A. Aabloo, and M. Klintenberg, Vacancy clusters at the semicoherent CuNb metallic interface, *submitted to Physical Review B.*

Authors contribution

In Paper I the author planned and performed the initial DFT calculations, developed the potential fitting method and did the fitting of the potential to reproduce DFT input data. In addition, the author contributed to the writing process of the related sections. Next, in Paper II the author developed the software needed for the simulations and did all the calculations presented. Moreover, the author prepared the manuscript in its full length. The authors contribution in Paper III was mainly in performing a part of TDDFT simulations and analysis of the results. Finally, in Paper IV the author performed all the needed TDDFT simulations to study the electronic losses and developed a new method to include similar electronic losses into classical MD. Also, author implemented the method in LAMMPS software package. Furthermore, the author performed all the MD simulations, analysed the data, and prepared the manuscript in its full length.

Abbreviations and symbols

ASA	atomic-sphere approximation
BCC	body centred cubic
BO	Born-Oppenheimer approximation
BZ	Brillouin zone
CPA	coherent potential approximation
CVM	cluster variation method
DFT	density functional theory
e-ph	electron-phonon
EAM	embedded atom method
EOS	equation of state
EPH	a model for studying electronic losses in classical simulations
FCC	face centred cubic
FEM	finite element method
GAP	gaussian approximation potential
GGA	generalised gradient approximation
HCP	hexagonal close-packed
HEA	high entropy alloy
HF	Hartree-Fock method
KKR	Korringa-Kohn-Rostoker method
LAMMPS	Large-scale Atomic/Molecular Massively Parallel Simulator
LDA	local density approximation
LJ	Lennard-Jones potential
MC	Monte Carlo method
MD	molecular dynamics
MEAM	modified embedded atom method
NMMC	nano-scaled metallic multilayer composite
NPT	isothermal-isobaric ensemble
NVE	microcanonical ensemble
NVT	canonical ensemble

PBE	Perdew-Burke-Ernzerhof exchange-correlation functional
ph-ph	phonon-phonon
PKA	primary knock-on atom
SNAP	spectral neighbor analysis potential
SQS	special quasi-random structure
SRIM	the stopping and range of ions in matter
SRO	short-range order
TDDFT	time-dependent density functional theory
TTM	two temperature model
VASP	Vienna ab-initio simulation package
XC	exchange-correlation
ZBL	Ziegler, Biersack, and Littmark potential

Chapter 1

Introduction

The ever-growing demand for more energy has forced scientists to look for new ways to produce large quantities of energy from more abundant sources than fossil fuels. Although, renewable sources like wind, solar and hydro are easily accessible they are incapable of meeting the demand needed by the industry. For example in 2014 the amount of energy produced by renewable sources was around 10% of the total production [1]. This is mostly due to the low efficiency of renewable sources or because of the lack of scientific advances in these fields. Another limiting factor is related to the conditions imposed by the geographic locations where the energy consumption takes place. For example creating large wind parks or solar arrays close to the cities might be unfeasible as a result of the limited availability of the land. Also, northern regions might not be suitable for solar power production due to low intensity of sunlight throughout the whole year. Therefore, best alternatives for high power production are fission and fusion energy plants. Currently, the main concerns with nuclear power sources are related to the safety of the power plant and the negative attitude towards nuclear power in general.

The major safety concerns in nuclear reactors are related to the materials and fuels used in the power plant. The extreme conditions that the materials have to endure in a reactor are high doses of radiation, high temperature, and also highly corrosive environments. This is especially true in the next generation reactors (Gen-IV) [2], where the radiation dose is significantly higher than in the current systems. Furthermore, the substitution of water with liquid metals for heat transport creates a highly corrosive environment. Additionally, the materials used in fusion reactors, such as ITER [3], have even higher demands on the material due to very high temperatures of the plasma and high energy neutrons and He released in the process. This work will mainly focus on the radiation damage related issues in the material.

The main effects resulting in material degradation during irradiation is caused by the point-defect creation in the material by energetical particles. The fast neutrons initiate a collision cascade within the material by transferring most of its kinetic energy to a lattice atom. This primary knock-on atom will collide with the surrounding atoms and, also, excite the electrons. During such an event the lattice will heat and can even melt locally. Next, multiple point-defects, such as vacancies and interstitials, will be created and during the cool-down most of the created defects will annihilate leaving behind isolated Frenkel pairs. The remaining defects will migrate within the material, due to diffusion processes, and they could form clusters. The growing vacancy clusters can form voids and trap implanted He atoms. This causes the material to swell [4, 5, 6, 7] and eventually cause embrittlement [7]. These effects in term create stresses within the material and cause it to fail. Also, the sessile clusters of interstitial and vacancies act as obstacles for dislocation mobility and cause the hardening of the material [8, 9, 7]. Therefore, understanding and controlling the production of Frenkel pairs and clusters enables to create an optimised radiation resistant material.

A way to control the growth of clusters is by adding high efficiency sinks into the structure of the material which attract nearby point-defects. This is achieved, for example, in nano-scaled metallic multilayer composites where the nanometre thick layers of immiscible elements are stacked intermittently. Numerous experimental studies of Cu-Nb NMMC [10, 11, 12] have shown that the number of point-defects is lower than in the pure elements making up the compound. Furthermore, a void denuded zone was observed of around 20 nm thick near the interface [13]. Computer simulations have shown that the point defect creation at the metallic interface is significantly lower than in the bulk of the material [14, 15, 16]. Therefore, the created point-defects would migrate towards the interface where they can annihilate or escape the material. Finally, a recent study showed that the Cu-Nb metallic interface can accommodate vacancy clusters consisting of up to four vacancies [17], which could increase the sinks efficiency to capture interstitials.

Recently, a new group of materials called high entropy alloys has been proposed for radiation resistant applications [18]. These materials consist of five or more elements creating a single phase solid solution. Experimental studies have reported remarkable properties of these materials. Namely, HEAs have high hardness and compressive strength at both room and elevated temperatures [19, 20, 21]. Next, it has been shown that they are more resistant to wear than common steels [21, 22]. Also, a better corrosion resistance than in stainless steel has been observed for $Al_{0.5}CoCrCuFeNi$ HEA [21, 23].

However, only a few studies have been done to look at the radiation resistance of HEAs [24, 25, 26]. The computational study of such materials is challenging due to the multi-component nature of the alloy. But these methods are crucial in gaining information on the underlying mechanisms occurring during the radiation damage. Therefore, a framework for correctly doing collision cascade studies in HEAs is needed.

1.1 Purpose of this work

The purpose of this work is to describe the most important theoretical aspects of doing radiation damage studies of a HEA. First, we propose a novel method for modifying the empirical potentials to correctly describe the short-range interactions between all the elements making up an alloy. The method is demonstrated with an EAM type potential for pure Ni. Next, the atomic-scale properties of Ni-based HEAs are investigated using the MC method combined with DFT. This enables us to characterise the chemical ordering in these alloys and check whether the random solid solution assumption can be applied to all HEAs. Finally, we study the energy transfer from a moving projectile into the electronic system using TDDFT calculations. In order to apply the TDDFT results in classical MD simulations, a new method is developed to include electronic losses into the classical simulation in a precise and effective manner. All these aspects are crucial in the study of exact mechanisms of defect production and evolution during the irradiation process of HEAs.

Chapter 2

Concept of high entropy alloy

High entropy alloy [19] is a novel concept of designing materials with controllable properties. The HEAs are usually made of 5 or more elements each having atomic concentrations from 5 - 35% and forming a single phase solid solution alloy. Additionally, small quantities (less than 5%) of minor elements can be added to the HEA for alloying purposes. The HEAs are mostly in FCC and BCC crystal structures, but recently also HCP HEA has been experimentally confirmed [27]. The properties of a HEA are affected by four core effects: high-entropy, sluggish diffusion, severe lattice distortion and cocktail effect.

Due to the many elements making up a HEA the configurational entropy term has to be taken into account in determining the equilibrium phase diagram. A balance between entropy of mixing and enthalpy of mixing defines whether a system will separate into single element phases, create an intermetallic alloy or form a solid solution. A system with large positive enthalpy of mixing and low entropy of mixing will be driven towards the pure single element phase as this would lead to the lowest free energy. Therefore, a rapidly cooled multi-component solid solution would separate into regions with high concentration of single element. On the other hand, negative enthalpy of mixing and low entropy of mixing would have the lowest free energy when an intermetallic compound is formed. The intermetallic differs from a solid solution because of the presence of long range order. Finally, in a system with a near zero enthalpy of mixing the configurational entropy would contribute the most to the free energy and a random solid solution phase would be stabilised at relatively low temperatures. Furthermore, this assumption is often used when calculating the properties or when studying the phase stability of HEAs.

Next, the random nature of the HEA solid creates large fluctuations in the lattice potential. The high energy lattice potential sites will hinder the diffusion of atoms through those sites due to high energy penalty needed. On the other hand, the low energy sites will act as traps for diffusing atoms and; therefore, hinder their further mobility. Both, of these effects propose that the diffusion in a HEA should be lower than in the pure elements. In fact, experiments have shown that the self diffusion in CoCrFeMnNi HEA is an order of magnitude slower for most components than in pure element systems

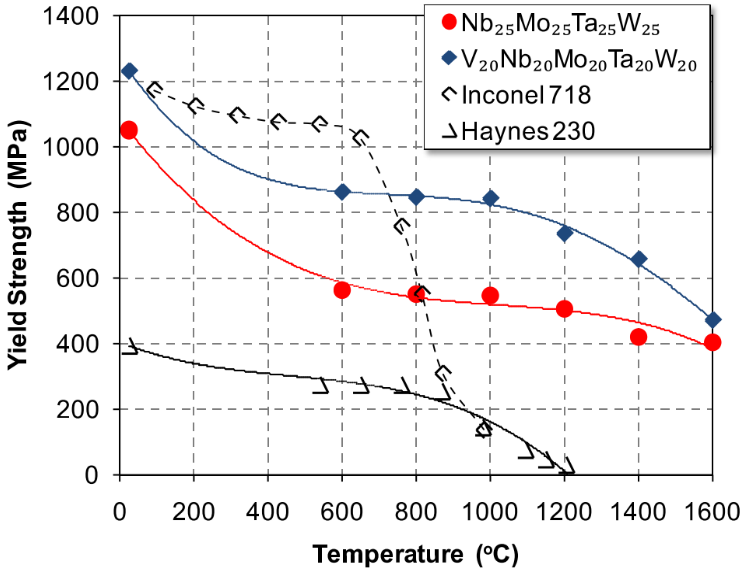

Figure 2.1: The temperature dependence of the yield stress of $Nb_{25}Mo_{25}Ta_{25}W_{25}$ and $V_{20}Nb_{20}Mo_{20}Ta_{20}W_{20}$ HEAs and two superalloys, Inconel 718 and Haynes 230. Reprinted from [29] with permission from Elsevier.

[28]. The sluggish diffusion effect could be advantageous for decreasing phase separation due to the growth of precipitates and point-defect cluster growth.

The large differences in atomic radii can cause a HEA have a highly distorted lattice. This will affect the scattering of electromagnetic waves, electrons, and phonons. The scattering in electromagnetic waves will result in difficulties of determining the crystal structure of the material because peaks that are usually associated with a crystal structure will become smeared. Also, the scattering of electrons and phonons will result in the lower free path. Therefore, multiple properties related to the energy transport could become affected. Indeed, in a recent work by Caro *et al.* [30] it was shown that thermal conductivity is always lowered when additional element types are included. Also, it has been shown that mechanical properties of HEA are insensitive to temperature due to the severe lattice distortion effect. For example, in the refractory NbMoTaW and VNbMoTaW HEAs the yield strength was relatively stable over a large temperature range (Fig. 2.1) [29].

Finally, the cocktail effect allows to construct a HEA based on properties of single components. For instance, the crystal structure of CuCoNiCrAlFe

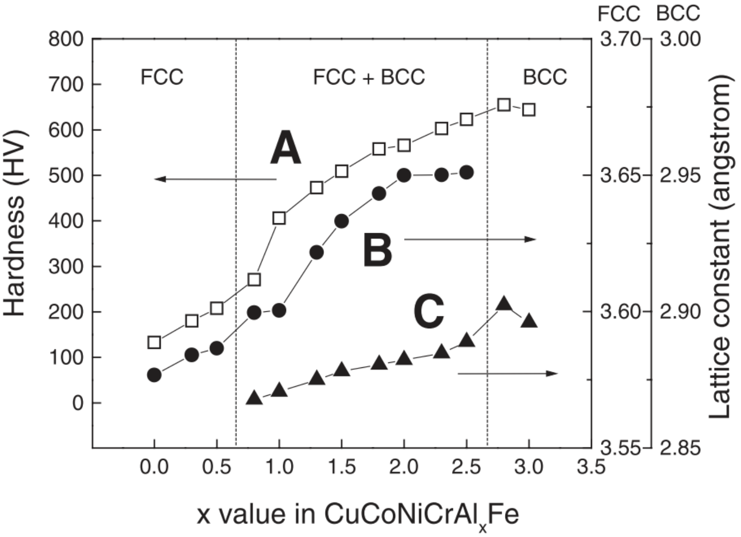

Figure 2.2: Hardness and lattice constants of CuCoNiCrAl$_x$Fe alloy system with different x values: A) hardness of CuCoNiCrAl$_x$Fe alloys, B) lattice constant of FCC phase, C) lattice constant of BCC phase. Reprinted from [19] by permission from John Wiley and Sons, Inc. .

HEA alloy can be tuned from FCC to BCC by tuning the concentration of Al in the alloy from low to high (Fig. 2.2) [19]. Similarly, other mechanical properties like strength can be modified.

These four main effects can be beneficial for the radiation tolerance of HEAs. For example, the sluggish diffusion effect would result in higher vacancy formation energy because an additional enthalpy of mixing penalty has to be added. Also, the low diffusivity would hinder the clustering of point-defects and; therefore, lower the swelling and hardening of the material. The high entropy effect will drive the irradiated material towards a random solid solution as its free energy is lowest at room temperatures. Additionally, during a cascade the melted crystal will intermix, but due to the randomness of the solution the mixed system will be random and; thus, be close to the equilibrium structure. This means that there would not be any accumulation of primary damage. So far the radiation resistance aspects of HEA have not been studied thoroughly and much of the research is being done.

Chapter 3

Computational methods in materials science

3.1 Density functional theory

The density functional theory is a method for solving the many-body time-independent Schrödinger equation (3.1) within the Born-Oppenheimer approximation [31]. Therefore, it is assumed that the electrons are always in the ground state for a particular configuration of atoms. The theory is based on the Hohenberg-Kohn theorems [32] which prove that the density of interacting particles $\rho(\mathbf{r})$ in an external potential $V_{ext}(\mathbf{r})$ is uniquely determined. Thus, the density of this system determines all properties of the system including the many-body wave function. The second theorem provides a method of determining the density based on a universal functional of the energy $E[\rho(\mathbf{r})]$. It states that for any particular $V_{ext}(\mathbf{r})$ the exact ground-state energy of the system is the global minimum of the functional $E[\rho(\mathbf{r})]$ and the density that minimises the functional is the exact ground state density $\rho_0(\mathbf{r})$. The main issue with the Hohenberg-Kohn theorems is that the exact form of the energy functional $E[\rho(\mathbf{r})]$ is not known. Nevertheless, if an approximate form for the energy functional would be known the problem of solving a $3N$-dimensional problem, where N is the number of electrons, would turn into a 3-dimensional problem. A common way to present the energy functional $E[\rho(\mathbf{r})]$ is shown in Eq. (3.2), where all the known terms are written explicitly and the unknown terms are contained within the exchange-correlation functional $E_{xc}[\rho(\mathbf{r})]$.

$$\hat{H}\Psi(\mathbf{r}) = E\Psi(\mathbf{r}) \tag{3.1}$$

$$E[\rho(\mathbf{r})] = T[\rho(\mathbf{r})] + \int d\mathbf{r} V_{ext}(\mathbf{r})\rho(\mathbf{r}) + \frac{1}{2}\int d\mathbf{r}\int d\mathbf{r}' \frac{\rho(\mathbf{r})\rho(\mathbf{r}')}{|\mathbf{r}-\mathbf{r}'|} + E_{xc}[\rho(\mathbf{r})] \tag{3.2}$$

Next, Kohn and Sham proposed a set of equations and a procedure to find a solution to the many-body Schrödinger equation by using the Hohenberg-Kohn theorems and non-interacting single-particle wave functions [33]. The proposed procedure is based on Eqs. (3.3) to (3.5). First, an initial guess for the total density $\rho_0(\mathbf{r})$ is made. Next, a potential $V_{KS}(\mathbf{r})$ is calculated based on this density. Then, the non-interacting single particle wave functions are obtained as the solutions to the one-particle Schrödinger Eq. (3.4). Finally, the solutions are used to construct a new density $\rho_1(\mathbf{r})$. If the initial density and the final density match a solution to the many-body Schrödinger equation is found as any density, and therefore wave function, which minimises the energy functional is the correct ground state of the system.

$$V_{KS}(\mathbf{r}) = V_{ext}(\mathbf{r}) + \int d\mathbf{r}' \frac{\rho(\mathbf{r}')}{|\mathbf{r} - \mathbf{r}'|} + V_{xc}[\rho(\mathbf{r})] \tag{3.3}$$

$$\left(-\frac{\hbar^2}{2m_e}\nabla^2 + V_{KS}(\mathbf{r})\right)\varphi_i(\mathbf{r}) = \epsilon_i\varphi_i(\mathbf{r}) \tag{3.4}$$

$$\rho(\mathbf{r}) = \sum_i \varphi_i^*(\mathbf{r})\varphi_i(\mathbf{r}) \tag{3.5}$$

The main source of discrepancies between the experimental and DFT results occurs from the selection of the exchange-correlation functional. The simplest exchange-correlation functional is the local density approximation and it depends only on the electronic density at any point in space. The numerical values for LDA are often obtained from quantum Monte Carlo simulations of the homogeneous electron gas and a commonly used parameterization is by Perdew *et al.* [34]. Often, the lattice parameters calculated with LDA are somewhat larger than in the experiments [35]. Also, the magnetic states of some of the elements are falsely predicted [36]. Another group of exchange-correlation functionals is called the generalised gradient approximation. In this case the energy functional term depends on both the electronic density and its gradient. As it is not possible to uniquely define GGA, multiple flavours of GGA exist (like PBE [37], PW91 [38], AM05 [39], etc.). These often tend to underestimate the lattice parameter, but many magnetic properties are correctly obtained using these functionals and, thus, they are often used. Final group of exchange-correlation functionals are called hybrid functionals and they are obtained by combining LDA, GGA and HF method. These are often used with molecular systems and are usually computationally more expensive than the previously mentioned functionals.

Many different codes for doing DFT calculations exist available both freely and commercially. The main groups are divided based on the wave function expansion basis. The most common variants are plane-waves, numerical orbitals, atomic like orbitals, gaussians, etc. The codes based on plane-waves are often used in solids due to the periodical nature of such systems. Additionally, to decrease the number of basis functions in plane-wave codes pseudopotentials are used. The fast oscillating wave functions near the core of the atoms are replaced by smooth functions. This in turn lowers the number of interacting electrons in the system to the valence electrons only which define most of the material properties in metals for example. Finally, the effectiveness of many codes allows to conduct molecular dynamics simulations based on DFT where the forces acting on atoms are obtained from the ground state electronic density by Hellmann-Feynman forces [40]. The atoms in DFT-MD are treated like classical objects and their motion is governed by Newton's laws of motion.

The major disadvantage of the DFT method, in addition to the approximations used, is its high computational cost. The systems are usually limited to about 500 atoms and the timescale is limited to a few picoseconds. Thus, it is not possible to investigate slow processes, like diffusion, using DFT. The method is often used to calculate static properties of the material that depend on either the total energy or the electronic system.

3.1.1 Time-dependent density functional theory

The DFT-MD simulations based on the BO approximation can not be applied to the processes where electronic excitations have to be taken into account, such as radiation damage where the electrons are excited by the passing projectile. The time-dependent density functional theory is an extension of DFT for solving the many-body time-dependent Schrödinger equation (3.6). This is achieved with the Runge-Gross [41] theorems where a one-to-one correspondence between time-dependent density $\rho(\mathbf{r}, t)$ and the one-particle potential $V_{ext}(\mathbf{r}, t)$ is showed for a specific initial state Ψ_0.

$$i\hbar\frac{\partial}{\partial t}\Psi(\mathbf{r}, t) = \hat{H}(t)\Psi(\mathbf{r}, t) \tag{3.6}$$

Similarly to DFT, time-dependent Kohn-Sham Eqs. (3.7) to (3.9) are used to find the time-dependent density $\rho(\mathbf{r}, t)$ from an initial ground-state $\rho_0(\mathbf{r})$. An important difference with DFT is that the XC functional depends not only on the current density, but also on the history of electronic densities. As the exact form for this functional is not known the LDA functional in adiabatic regime is used [42, 43]. Therefore, the XC functional depends only on the electronic density at the current time and only on the local value of the density. As the differential Eq. (3.8) is solved numerically, stable time integrators, such as fourth-order Runge-Kutta with an error of $O(\Delta t^4)$, have to be used to obtain correct results from the calculations [44].

$$V_{KS}(\mathbf{r},t) = V_{ext}(\mathbf{r},t) + \int d\mathbf{r}' \frac{\rho(\mathbf{r}',t)}{|\mathbf{r}-\mathbf{r}'|} + V_{xc}[\rho(\mathbf{r},t)] \tag{3.7}$$

$$i\hbar \frac{d}{dt}\varphi_i(\mathbf{r},t) = \left(-\frac{\hbar^2}{2m_e}\nabla^2 + V_{KS}(\mathbf{r},t)\right)\varphi_i(\mathbf{r},t) \tag{3.8}$$

$$\rho(\mathbf{r},t) = \sum_i \varphi_i^*(\mathbf{r},t)\varphi_i(\mathbf{r},t) \tag{3.9}$$

The TDDFT method allows to calculate the electronic stopping of various projectiles in different hosts from nonperturbative first-principles and has been shown to agree well with experimental results [45, 46, 47]. Therefore, the method should be applied to investigations of radiation damage in HEA, where no experimental results are readily available.

3.2 Molecular dynamics

The molecular dynamics approach enables to study systems containing millions of atoms and up to a period of couple ns. The trajectories are obtained by integrating the Newton's laws of motion (3.10).

$$\mathbf{f}_i = m_i \mathbf{a}_i \tag{3.10}$$

As the integration is done numerically the trajectories are highly dependent on the integration method used. LAMMPS [48] uses velocity-Verlet integrator which has a local error on position of the order of $O(\Delta t^4)$ and velocity $O(\Delta t^2)$. In all MD simulations an important user controlled parameter is the timestep used for the integration. If fast processes like collision cascades are simulated the timestep has to be selected accordingly. In such processes a very short timestep is needed in the beginning of the simulation where some atoms have high kinetic energy. During the next stages, this initial high energy is dispersed among other atoms and a larger timestep can be chosen. This dynamic timestep adaptation can shorten the total simulation time significantly.

Unless molecular statics calculations are done to find elastic properties, defect energetics, stable structures, etc. the trajectories themselves have very little practical value. In MD simulations thermodynamic averages of a system have to be measured. These can be pressure, temperature, diffusion, etc. This often means that doing a single simulation to measure a property can lead to wrong conclusions and in order to achieve trustworthy statistics many simulations have to be done. This can be often computationally very expensive and time consuming.

Another user controllable parameter is the choice of the thermodynamic ensemble for the MD simulation. The most common options are microcanonical, canonical and isothermal-isobaric ensemble. The NVE ensemble conserves the number of particles, volume of the system, and the total energy. The NVE simulations are used to study dynamical events, such as collision cascade. In the NVT ensemble the conserved quantities are number of particles, volume of the system, and the temperature of the system. The conservation of temperature is achieved through the use of a thermostat that is coupled with the current system through a coupling parameter. If a small system is simulated the ordinary Nose-Hoover thermostat can lead to incorrect statistics due to the limited number of degrees of freedom of the thermostat and therefore multiple thermostats have to be chained [49]. Also, the selection of the coupling parameter can influence the results significantly. The NVT ensemble is useful for the study of dynamic processes at a certain temperature, such as defect diffusion. In the NPT ensemble the number of particles, the pressure and the temperature of the system are conserved. The NPT ensemble can be used to study properties of the material at constant pressure, such as thermal expansion.

In MD only the motion of atom-like point-masses is analysed. Therefore, the system does not have any electrons explicitly. As the forces acting on atoms arise both from surrounding electrons and the nuclei of the neighbouring atoms, empirical potentials or force fields have to be used. The forces acting on atoms are defined by an empirical potential and can be calculated from the following equation:

$$\mathbf{f}_i = -\nabla_i U. \tag{3.11}$$

Therefore, the results of MD simulations are highly dependent on the empirical potential used for a specific system. In fact, wrong conclusions could be obtained when using a potential outside its fitting region [14, 17] and, therefore, the suitability of an empirical potential has to be analysed before doing any production runs. As it is not possible to have perfect empirical potentials a trade-off in the accuracy has to be made.

3.2.1 Empirical potentials

The easiest type of potentials depend only on the distance of neighbouring atoms and are called pair-potentials (3.12). Lennard-Jones is one of such potentials and its mathematical form is shown in Eq. (3.13). The parameters ϵ_{ij} and σ_{ij} describe the depth of the potential well and its location respectively for the interaction between atom types i and j. LJ potential is widely used to study liquids and gases. For example, in the work by Bläckberg *et al.* [50] the mobility of Xe atoms was studied on the amorphous surface of

Al_2O_3 with LJ potentials. The major advantage of pair-potentials is that they are computationally very cheap. In order to limit the interactions only to a few neighbouring shells the potentials are truncated with a cutoff function. Therefore, the computation can be easily parallelised and speeded. Although LJ potentials are also used to study solids, it has to be emphasised that pair-potentials are not able to contain all the needed information. For example, it is not possible to reproduce all the elastic coefficients using such a potential.

$$U_{LJ} = \frac{1}{2} \sum_{i}^{N} \sum_{j \neq i} \phi_{ij}^{LJ}(r_{ij}) \tag{3.12}$$

$$\phi_{ij}^{LJ}(r_{ij}) = 4\epsilon_{ij} \left[\left(\frac{\sigma_{ij}}{r_{ij}} \right)^{12} - \left(\frac{\sigma_{ij}}{r_{ij}} \right)^{6} \right] \tag{3.13}$$

Embedded atom type [51] potential formalism was developed to better describe solids. The energy of an atomic system is defined by Eq. (3.14), where $\phi_{ij}(r_{ij})$ is the pairwise interaction between atoms i and j, and F_i is the additional energy term arising due to embedding an atom into electronic background density $\bar{\rho}_i$. The site density is calculated with Eq. (3.15). Although the EAM potentials, developed initially, used the real electronic density, lately all functions making up a potential are fitted with analytic functions or cubic splines to reproduce the fitting parameters.

$$U_{EAM} = \frac{1}{2} \sum_{i}^{N} \sum_{j \neq i} \phi_{ij}(r_{ij}) + \sum_{i}^{N} F_i(\bar{\rho}_i) \tag{3.14}$$

$$\bar{\rho}_i = \sum_{j \neq i} \rho_j(r_{ij}) \tag{3.15}$$

3.2.2 Langevin dynamics

The Langevin dynamics is a model where the dynamics of the atomic system is characterised by Eq. (3.16). The first term on the right side of Eq. (3.16) is related to the adiabatic motion of atoms, where the forces acting on atoms depend on the many-body potential U. The next two terms are related to the energy removal from the system through the friction term $\beta\mathbf{v}$ and the equilibration of the system with an external energy reservoir at temperature T through the random force $\eta(t)$.

$$m_i \mathbf{a}_i = -\nabla_i U - \beta \mathbf{v}_i + \boldsymbol{\eta}(t) \tag{3.16}$$

The random force has to obey Eqs. (3.17) and (3.18) in order to have the correct statistics in the simulation. Additionally, in order to correctly describe the real systems the friction parameter β has to be selected with care. In a metallic system this can be viewed as the electron-phonon coupling parameter where the motion of atoms excites the electron bath. Therefore, the lattice vibrations are damped by electrons, which corresponds to a phonon being removed and an electron being excited. The random force $\boldsymbol{\eta}$, on the other hand, removes energy from an excited electron and excites a phonon in the crystal. Therefore, in the simulation an equilibrium is achieved through these two processes between the electron bath and the lattice both at temperature T.

$$\langle \boldsymbol{\eta}(t) \rangle = 0 \tag{3.17}$$

$$\left\langle \boldsymbol{\eta}(t)\boldsymbol{\eta}(t') \right\rangle = 2\beta k_B T \delta(t - t') \tag{3.18}$$

3.2.3 Non-adiabatic molecular dynamics

Early attempts to include electronic losses into classical MD were done by Caro *et al.* [52]. The Langevin equations of motion (3.16) were used to include interactions between the moving atoms and the electronic system. The friction coefficient was considered to be density dependent and have the following form:

$$\beta(\rho) = A \log_{10}(\alpha \sqrt[3]{\rho} + b), \tag{3.19}$$

where A and b are adjustable parameters and $\alpha = 3.09a_0$, where a_0 is the Bohr radius. Therefore, a single friction term was used for both the electron-phonon and electronic stopping regimes. As the projectiles with higher velocities explore shorter inter-atomic distances, then the average of the coupling parameter $\beta(\rho)$ will differ for lower and higher velocities. Unfortunately, the method is not being used actively, mostly due to the issues of acquiring the correct $\beta(\rho)$ parameter, and only recently interest to this formalism has arisen (Paper IV).

The two-temperature model is an extension of Langevin dynamics by Duffy *et al.* [53] to study the electronic effects within classical MD simulations. In this model the coupling parameter β is treated as a constant and has two separate values depending on the velocity of the atoms (3.20). Below a certain threshold velocity v_s only the electron-phonon coupling is considered through the parameter β_{e-ph}, indicating the regime where thermal vibrations excite the electrons. Above the threshold velocity the coupling parameter related to electronic stopping β_s is added. Thus creating a sharp change in the total coupling parameter. Both, of these parameters are obtained either from experimental data or from first-principle method calculations.

$$\beta_i = \begin{cases} \beta_{e-ph} & \text{if} \quad v_i \leq v_s \\ \beta_{e-ph} + \beta_s & \text{if} \quad v_i > v_s \end{cases} \tag{3.20}$$

Another part of the TTM model is the spatial and time evolution of energy within the electronic system. The energy removed from atoms is transferred into the electronic system at the specific site where it is redistributed within the electronic system through heat diffusion equation (3.21). The coefficients C_e and κ_e describe the heat capacitance and thermal conductivity of the electronic system and are properties of the material. The parameter g_p is the coupling constant for electron-phonon interaction and g_s describes the source term due to electronic stopping. Finally, T_e is the temperature of the electronic and T_a of the atomic systems. All these parameters are related to the parameters of the MD simulations by using the energy balance equations [53]. The heat diffusion equations can be solved numerically within an MD simulation with little computational overhead.

$$C_e \frac{\partial T_e}{\partial t} = \nabla(\kappa_e \nabla T_e) - g_p(T_e - T_a) + g_s T_a' \tag{3.21}$$

The TTM model can be used to study radiation damage, such as collision cascades, within the empirical classical MD simulations. The two main caveats of the method are, firstly, the use of two separate coupling constants that create a discontinuity in the total β and, secondly, the use of constant electronic heat capacity and conductivity which can change both due to temperature and spatial disruptions of the lattice. The former issue will be dealt with in Section 6.5 by our EPH model.

3.3 Monte Carlo method

Monte Carlo is a class of methods where a solution to a many-body problem is achieved through the random sampling of the variable space. In materials modelling MC methods are used to for example find the equilibrium phase of an alloy, study the evolution of defects, etc. Sometimes the atomic trajectories are of no importance and only thermodynamic averages are needed. The Metropolis sampling algorithm [54] can be used to sample the phase space with correct probabilities and; therefore, statistics are gathered throughout the simulation. In a MC simulation the phase space is sampled by doing certain changes to the system. These can include for example removal or addition of an atom, swapping of the element types between two atoms, small displacement of an atom, etc. After every such an event the change in the Hamiltonian $\Delta H_{A \to B}$ is computed. If the total energy is decreased during such an event then the new state is always accepted. If the energy increases, then the new state is accepted with the probability $p_{A \to B}$ given by Eq. (3.22). The term k_B is Boltzmann constant and the temperature T is the temperature of the system in the the MC simulation.

$$p_{A \to B} = \exp\left(-\frac{\Delta H_{A \to B}}{k_B T}\right) \tag{3.22}$$

The energy difference between different states of the system can be obtained from various methods. Also, this is the most time-consuming part of the MC method. For example, by using an empirical potential, large systems can be used in MC calculations where a single step could take seconds of computational time, but at the cost in the accuracy of the results. On the other hand, if energy would be calculated from DFT a single step for a 128 atom simulation could take hours. Therefore, the number of total steps would be significantly lower and; thus, the sampling of the phase-space could be not sufficient. In addition, in the object MC simulation only energy tables for various events, such as defect migration, defect clustering or splitting, are used and only the motion of such objects are studied.

Chapter 4

Construction of empirical potentials suitable for radiation damage simulations of HEA

4.1 General concept

The MD simulations of HEA require empirical potentials that can describe the properties of multiple pure element equilibrium phases as well as mixtures made from them. The usual way of constructing such a potential begins with the creation of pure element potentials or finding them from the literature. It is important that the quality of these potentials is high as the errors will carry over to the alloy potential and will influence the obtained results.

Most of the potentials are created to reproduce a limited set of input parameters, such as cohesive energy, elastic coefficients, point-defect formation energies, etc. These properties often involve interatomic distances near equilibrium atomic positions. Therefore, the potentials have to be verified for the use outside the fitting region either with experimental data or with higher quality methods, such as QM calculations.

The pure element potentials have to be renormalised, due to the non-unique nature of EAM formalism, using the effective transformation method as described in Caro *et al.* [55]. This allows the properties of an alloy to be corrected by defining the pairwise potential only. In the study of alloy interaction with noble gases like Xe an LJ potential could be used for the pairwise term as was done in the work by Bläckberg *et al.* [50]. But, as the single components of HEA depend also on the electronic neighbourhood of the host, a more complex function would have to be used. Because the EAM formalism is an approximation, creating a potential that could cover all possible alloys correctly could become a rather challenging problem. Therefore, a set of potentials is created instead for each study case. For example, a four component potential would be used for NiCrCoFe alloy and a three component one for NiCrCo where the former one could have considerable errors when using it on the three component system.

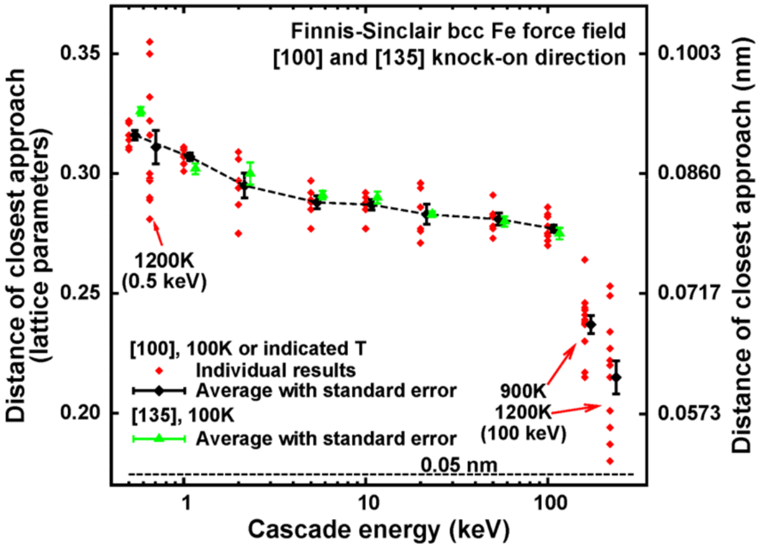

Figure 4.1: Closest distance between atoms in a PKA simulation of BCC Fe at various cascade energies (Paper I).

4.2 Short-range behaviour

Commonly, the potentials are fitted against materials equilibrium properties. Therefore, using such a potential outside the fitting region could produce arbitrary results. In a collision cascade simulation atoms can approach each other very close. In fact, the distance between atoms in a BCC Fe can be as small as 0.75 Å for a 100 keV PKA energy as can be seen on Fig. 4.1 (Paper I). Therefore, in such simulations the potential has to be modified to include the correct behaviour.

A common approach for making the potential suitable for radiation damage studies has been the linking of the original potential with ZBL at a predefined cutoff (around 2.0 Å) [56]. The selection of the cutoff has been arbitrary and the linking function often selected is a polynomial that connects the original potential with ZBL smoothly in the intermediate region. The method has been successfully compared to QM calculations [57, 58], but the comparison has mostly been made with the dimer energy in vacuum only. This method could work relatively well with elements that depend on pairwise interactions only, such as He [59, 60], but could fail if the host crystal also affects the interaction. In our study we have found that the creation of the Frenkel pairs in a collision cascade depends both on the method of the linking as well as the selected cutoff distance (Fig. 4.2) (Paper I).

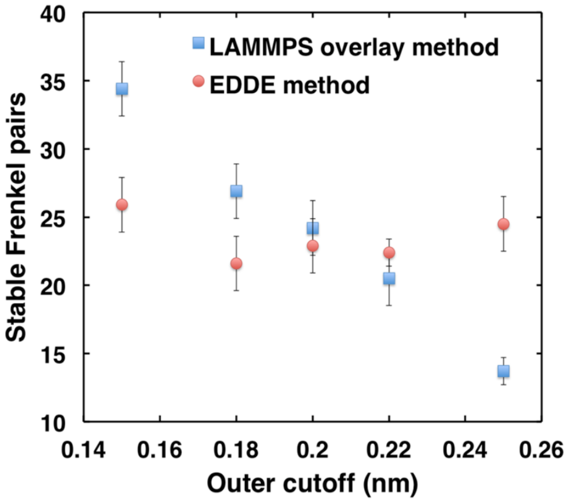

Figure 4.2: The average number of Frenkel pairs produced in a 10 keV cascade with different ZBL linking methods at various cutoff distances (Paper I).

The dimer energy of a Ni pair within a crystal as well as in vacuum was studied thoroughly with DFT as well as HF methods and compared to the ZBL potential (Fig. 4.3). It was found that at short distances the results follow ZBL potential relatively well. Thus, linking a potential with ZBL at these short distances would produce correct results. Nevertheless, at intermediate distances a discrepancy between dimer in vacuum and in a host crystal arises. This indicates that the potential can not be joined with ZBL arbitrarily, but instead the joining should follow the DFT energies.

Based on these results a recipe for connecting the initial potential with the ZBL was developed in order to obtain the desired results. The method was developed for the EAM potential, but can be used with appropriate modifications with other types as well. First, the density part of the original potential is modified to reduce the effects of the embedding term due to increasing density. This allows the potential to be fitted in two different regions by changing the pair-potential part and embedding function separately. Next, two cutoffs have to be chosen, where one is used for the connection to ZBL and the other for connection to the original potential. The cutoff distance for switching to ZBL is related to the quality of DFT calculations. As DFT calculations often use pseudopotentials, there exists a distance where the frozen core electrons start to overlap. This usually causes errors in the obtained results, where the resulting interaction is harder than it should be. Therefore, ZBL function should be used in that case instead.

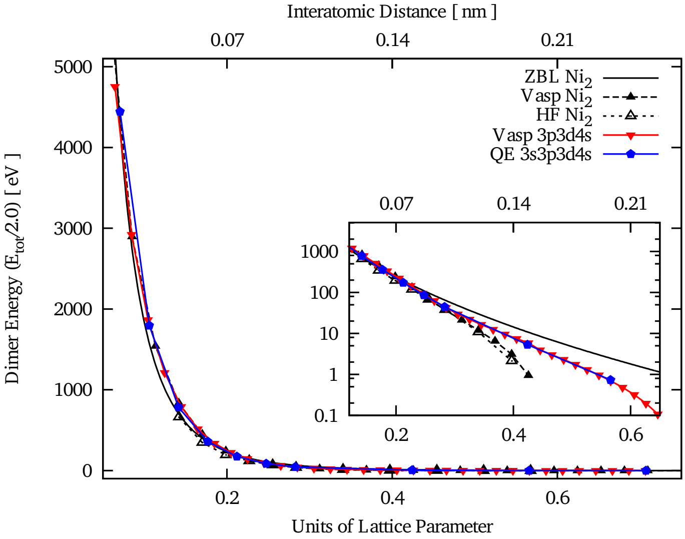

Figure 4.3: The dimer energy of the Ni-Ni pair as the function of the interatomic distance within the host Ni FCC crystal and in vacuum as calculated from DFT and HF methods and compared with ZBL potential (Paper I).

The longer cutoff is related to the equilibrium properties of the original potential. If a too large cutoff is selected the energetics of interstitials will be affected and; therefore, the resulting potential will become unusable for equilibrium properties. This intermediate region is fitted to reproduce the DFT dimer energies in the host crystal in the corresponding region using either an analytic function or, as in our case, cubic splines. The fitted curve is joined smoothly with ZBL function in the small distance region and with the original function at the other end. Finally, the equation of state is modified for the short-range part by refitting the embedding function for high densities. This procedure can be readily applied to multi-component alloys which are needed, for example, to study HEA.

By using the described procedure five potentials were constructed for FCC Ni. In all cases the smaller cutoff of 0.2 Å was used and the larger cutoff was varied to look at the effects of the cutoff on the Frenkel Pair generation. As a comparison, LAMMPS overlay method was used to generate additional five potentials with the same cutoffs. The latter method represents the traditional way of generating empirical potentials for the radiation damage studies. The outer cutoffs used were 1.5, 1.8, 2.0, 2.2, and 2.5 Å, where cutoffs smaller than 2.2 Å ensure that the interstitial properties of the original potential are left unchanged. In all cases the target function for

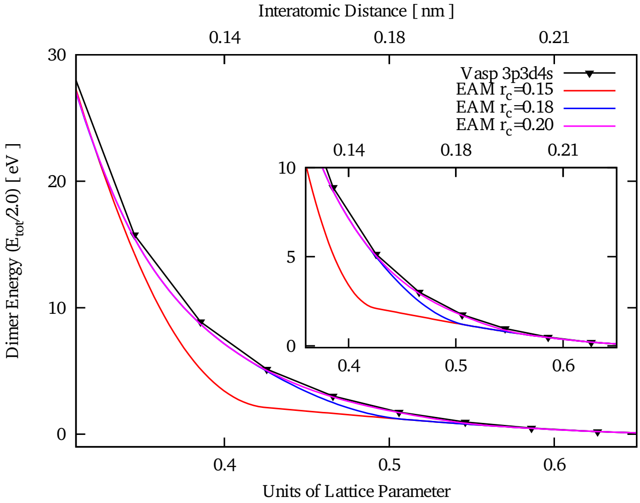

Figure 4.4: The dimer energy of the Ni-Ni pair as the function of the interatomic distance within the host Ni FCC crystal as calculated with the propesed fitting method in comparison with DFT results (Paper I).

the fitting was Ni dimer energies in Ni host crystal and the EOS of FCC Ni as calculated from DFT with VASP. The dimer energies calculated by using the newly fitted potentials along with the DFT target function are shown on Fig. 4.4. It can be seen that the fitting is only able to reproduce the DFT values within the fitting region. Thus, if the original potential deviates from DFT energies too much the largest cutoff possible should be used.

Finally, the cascade simulations with a 10 keV PKA were done to study the stable number of Frenkel pairs. The results showed that when using the traditional method the number of generated defects depends on the outer cutoff radius used (Fig. 4.2). This clearly indicates that the results are not trustworthy and the correct cutoff has to be selected by comparison with either experiments or other methods. On the contrary, when using our proposed method the results are less sensitive to the outer cutoff radius as can be seen from Fig. 4.2. This result shows clearly that our proposed method should be used when modifying the potentials for use in radiation damage studies and ensures stable defect production which can be directly compared with experimental results.

4.3 Future concepts

In the case when high quality potentials are not available from the literature, they have to be created from scratch. The traditional method of generating potentials involves the fitting of analytic functions to reproduce energetic properties such as cohesive energy, EOS, elastic parameters and point-defect formation energies. The major issue with this method is that only a limited set of phase-space is sampled and; thus, the properties of intermediate regions are determined by the form of the analytic function and can be somewhat arbitrary.

A much better approach is to use the force-matching method. In this case a large database of forces for different configurations are created by running DFT MD simulation at various temperatures and volumes. This database is used as the target function in the fitting where spline based functions are fitted to reproduce all the forces as closely as possible. Although, the method is powerful the major limitation for using it for many component alloys is the formalism of the potential used underneath. The EAM potentials do not have enough freedom to reproduce all desired properties simultaneously and; thus, the quality of the resulting potential might not be good enough. Therefore more complex potentials like MEAM have to be used.

The force-matching method was tested to create a Cu MEAM potential. The forces in the input database were reproduced by the fitted potential with great precision. Additionally, many energetic properties that were not used in the fitting were reproduced correctly. Despite that, the same procedure was not able to fit the forces for Nb system. This clearly indicates that the success of the method depends strongly on the potential formalism used.

In order to use MD for complex systems novel approaches such as GAP [61] and SNAP [62] have to be developed and used. As the computation power grows, doing DFT based MD simulations are probably still too slow to simulate even simple processes, but creating a large database of different configurations with correct forces and the interpolating between different phase-points might become feasible. Therefore, high quality results of large systems can be obtained by using such methods to investigate complex systems outside the reach of experiments.

Chapter 5

Atomic-scale structure and properties of Ni-based HEAs

5.1 General concept

The atomic-scale structure of a material can significantly influence both mechanical and electronic properties of the material. Therefore, an understanding about the structure of the HEA has to be obtained before doing any simulations. Currently, experimental methods are not able to obtain such information. Thus, other computational methods, such as DFT, have to be used.

The KKR-CPA method [63, 64, 65, 66] allows to calculated the electronic and mechanical properties of an alloy consisting of many elements effectively and fast. The main assumption for the method relies on the random solid solution composition of the material. Therefore, all the calculated properties are correct for the random alloy. If the equilibrium structure differs from the random solid solution, the results obtained for the random alloy will not be comparable with the experimental measurements. For example, the work by Lin *et al.* [67] showed that the electron-phonon coupling constant depends strongly on the density of states near the Fermi energy. Therefore, changes in the DOS can significantly affect processes mediated by e-ph interactions.

Also, the initial structure of a HEA in a collision cascaded simulation with MD could affect significantly the creation of stable Frenkel pairs as the lattice potential will be affected by the configuration. In addition, the lattice and electronic heat transport will be affected by the new structure. Therefore, the results obtained, when starting a simulation from a random alloy, could differ from experimental measurements and incorrect conclusions could be drawn.

It is commonly assumed that HEA forms a random solid solution due to large contribution of the configurational entropy in the free energy. Deviations from a random solid solution can substantially change the energetic properties of point defects as well as change thermodynamic quantities in general.

5.2 Short-range order parameter

The chemical-ordering in a material can be studied with the Warren-Cowley short-range order parameter [68]

$$\alpha_{ij}^{\nu} = 1 - \frac{p_{ij}^{\nu}}{c_j}, \tag{5.1}$$

where i and j denote the element types, p_{ij} is the probability of finding atom j near atom i in the atomic shell ν and c_j is the concentration of type j. If the atoms are randomly distributed within the material, then the SRO parameter α_{ij}^{ν} for all types i and for all neighbours j for all neighbouring shells ν is zero. If SRO parameter for element pairs i and j is larger than zero, then the number of pairs is lower than for the random solid solutions, and if the SRO parameter is smaller than zero, then the number of pairs is higher.

If the system is not in the random solid solution configuration, then the configurational entropy equation $S = k_B \sum c_i \ln c_i$ can not be used. Instead, it can be estimated by using the cluster variation method in the pair approximation [69]

$$S = k_B \left[(z-1) \sum_i (c_i \ln c_i - c_i) - \frac{z}{2} \sum_{ij} (y_{ij} \ln y_{ij} - y_{ij}) + \left(\frac{z}{2} - 1 \right) \right], \tag{5.2}$$

where z is the number of nearest-neighbours, c_i is the concentration of type i, and y_{ij} is the probability of finding a pair of atoms i and j.

5.3 Chemical-ordering in Ni-based HEA

To assess the random solid solution assumption and gain further insight into the exact structure of Ni-based NiCrCo ternary and NiCrCoFe quaternary alloys the configurational space was explored using DFT combined with MC sampling.

Due to the high computation cost of DFT the studied samples contained 128 atoms. The starting configuration was selected to be SQS structure which corresponds to the random solid solution within the small simulation box used. The SQS samples were constructed by interchanging the elements so that the SRO of each individual atom would be zero up to the third shell. Next, a series of MC simulations was conducted at three temperatures (500, 800 and 1200K) for both alloys. During the simulation the SRO of each individual atom as well as the potential energy was monitored. The simulations were run for 1500 steps in the case of NiCrCo and 2000 steps in

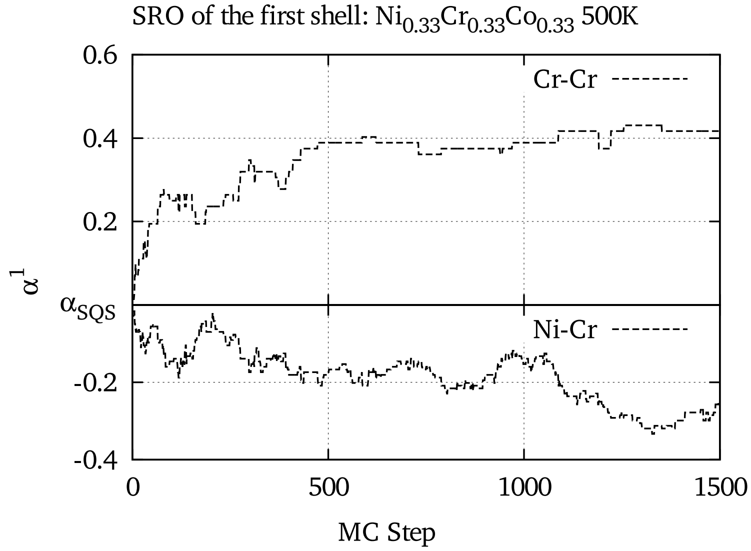

Figure 5.1: Evolution of SRO during a MC simulation combined with DFT at 500K for NiCrCo ternary alloy (Paper II).

the case of NiCrCoFe. During the simulation both the potential energy as well as SRO obtained a stable value (Paper II).

The main result of the MC simulation shows that the SRO does not remain zero as it would be expected for a HEA. In fact a rather large parameter for Cr-Cr pairs emerges (Fig. 5.1). This indicates that it is energetically preferable to have Cr atoms farther away from each other rather than next to each other. Additionally, the Ni-Cr pairs have a negative SRO indicating a larger number of such pairs than in a random alloy. A similar behaviour was also present, but somewhat smaller, in simulations at higher temperatures.

There are probably two main causes for such type of behaviour. First, as the Cr atoms are antiferromagnetic and both Ni and Co ferromagnetic then the spreading of Cr atoms would minimise the magnetic frustration of Cr and; therefore, the overall energy would be minimised. This is evident from the individual magnetic moments of atoms in SQS and structure with the SRO (Fig. 5.2). In the SQS sample the magnetic moments of Cr have both positive and negative moments. Whereas, in the structure with the SRO most of the Cr atoms have a negative moments of about 2 μ_B. Additionally, the spread in magnetic moments is reduced considerably with the SRO. Secondly, it is known that Ni and Cr atoms form an alloy with SRO [70, 71, 72]. Therefore, the increase in the SRO of Ni-Cr pairs might indicate the

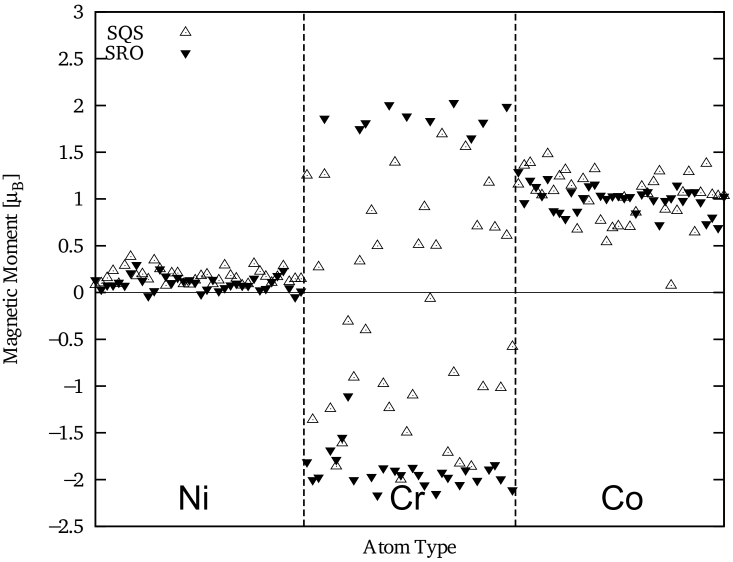

Figure 5.2: Magnetic moments of individual atoms in a SQS and a structure with SRO of NiCrCo ternary alloy (Paper II).

segregation of that phase. Due to the small sample used it is not possible to confirm this and simulation with larger sample size have to be done.

After relaxing the initial and final structures the atomic displacements from their initial positions remained rather small (about 0.04 Å) which indicates that in NiCrCo alloy the severe lattice displacement effect is missing. This is mostly due to the relatively similar atomic sizes of the elements used and therefore this effect cannot be assumed before hand and should be checked for each HEA individually. Moreover, the configurational entropy is lowered due to the SRO by 10% per atom.

The NiCrCoFe quaternary alloy undergoes a similar evolution in MC simulations as was the case for NiCrCo ternary alloy. Again, the Cr-Cr pairs have a large and positive SRO parameter value indicating the reduced number of such pairs. Next, the number of Ni-Cr pairs is larger than in the case of a SQS. Additionally, the number of Fe-Fe pairs has a positive SRO showing that Fe atoms are also spread within the sample (Fig. 5.3). By visual inspection of the final structure an ordered structure with simple cubic Cr sublattice could be seen implying an intermetallic phase. To verify this a simulation with a larger cell would have to be made.

The main reason for such a behaviour is due to the complex magnetic structure of NiCrCoFe quaternary alloy. The addition of ferromagnetic Fe atoms creates an even larger magnetic frustration of antiferromagnetic Cr

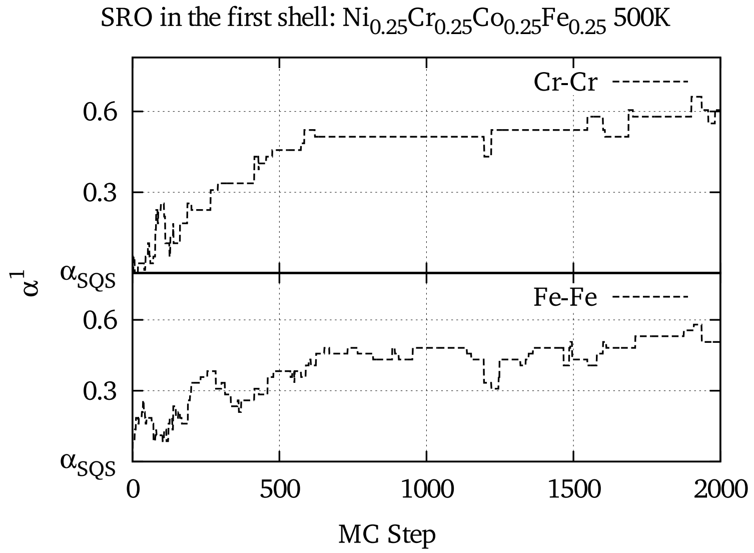

Figure 5.3: Evolution of SRO during a MC simulation combined with DFT at 500K for NiCrCoFe quaternary alloy (Paper II).

atoms. As in the case of NiCrCo ternary alloy the individual magnetic moments of atoms are mostly negative for Cr atoms and positive for all others (Fig. 5.4). When the sample is in SQS configuration there exists a rather large spread in individual moments. Whereas, the SRO removes that spread.

The atoms in the relaxed structures of both SQS and with a SRO did not move far from their initial positions and; thus, the crystal structure retains its pristine FCC structure. The atomic displacements were around 0.05 Å. This means that X-Ray diffraction studies of such a material would have sharp peaks and it would be impossible to see any difference between these two structures. In addition, the configurational entropy is reduced by about 25% (Paper II) and could significantly change the locations of phase boundaries.

5.4 Future concepts

Our results clearly show that the NiCrCo ternary and NiCrCoFe quaternary alloys do not form a perfect random solid solution, but instead contains SRO. This could significantly affect the point-defect formation energies and also their diffusion properties.

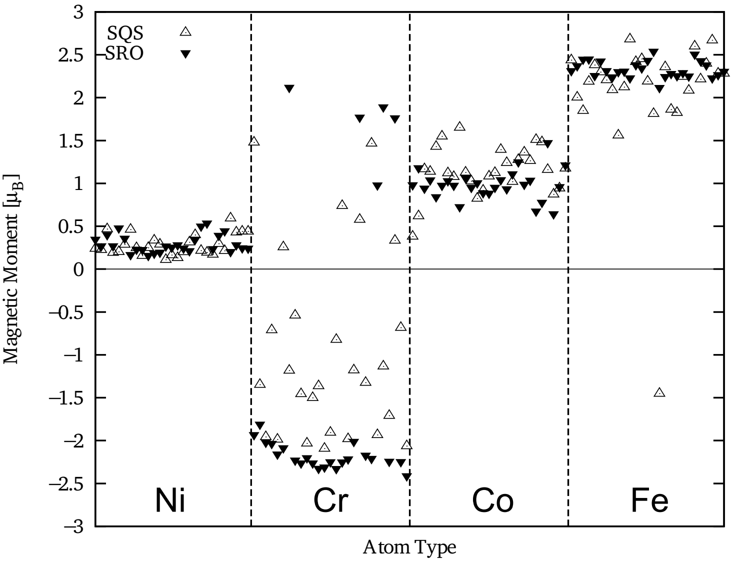

Figure 5.4: Magnetic moments of individual atoms in a SQS and a structure with SRO of NiCrCoFe quaternary alloy (Paper II).

A preliminary study was done to investigate the formation energy of vacancies at each individual site in NiCrCoFe quaternary alloy for SQS and the structure with SRO. It was found that in the SQS the vacancy formation energies have a relatively large spread and are about the same value of 2 eV. In contrast the spread is lower in the case of the structure with SRO. Moreover, the individual elements have slightly differing vacancy formation energies. Therefore, the vacancies would be created at specific sites through removing certain elements instead of being spread over all locations and elements.

Finally, many other atomic-scale properties should be analysed for both the SQS and SRO structures for these Ni-based alloys to investigate the effect of SRO and confirm or disconfirm the validity of common HEA assumptions. All of this could impact the results of large scale radiation damage simulations of HEAs.

Chapter 6

Electronic stopping in Ni and NiFe alloy

6.1 General concept

The collision cascade simulations of HEA needed to assess the damage production at doses predicted in next-generation power plants will use projectile energies of 100 keV and higher. At these high energies it is insufficient to handle atoms only ballistically as the interactions with electrons start contributing into the damage production mechanism. Therefore, electronic stopping has to be included into the classical simulation. The inclusion of electronic effects needs to take into account the many-component nature of HEA, where different elements could have different stopping, which in term could depend on the local environment. Indeed, it has been shown that the e-ph coupling depends strongly on the density of states [67] of the host material.

As the experimental measurement of stopping power in HEA is challenging it has to be acquired from computational methods. The stopping power of a projectile in an average medium could be assessed by using SRIM software package [73]. It is a widely used software for calculating, for example, the implantation depth of a projectile and is fitted to reproduce many experimental measurements. The main limitations with SRIM are related to the many approximations used in the software. Therefore, SRIM results have to be used with care [74]. Also, the perturbative QM method could be used to investigate the electron-phonon coupling in a single element material [75]. Recently, the KKR-CPA method [63, 64, 65, 66] was used to calculate the e-ph coupling parameter in pure Ni and random equimolar Ni binary alloys [76]. Unfortunately, the applicability of these results depends on the random alloy assumption of HEA. Therefore, new approaches like TDDFT are needed to calculate the exact environment dependent energy loss of the projectile in a HEA due to electronic effects.

Currently, the two-temperature model is capable of only handling the electronic stopping in a material as an average constant friction force acting on all atoms. The radiation damage simulations of HEA require different electronic stopping related terms for different elements as well as for different

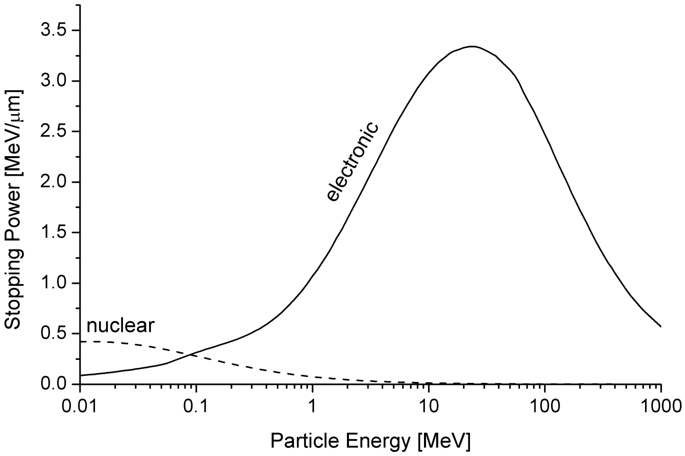

Figure 6.1: Schematic diagram of nuclear and electronic stopping as a function of projectile velocity [77].

local environments. Therefore, a new model has to be developed to include all these effects.

6.2 Stopping power

The stopping power shows how much energy is transferred from the moving projectile to the medium it passes.

$$S = -\frac{dE}{dx} \tag{6.1}$$

Stopping can be divided into two parts S_e and S_n (Fig. 6.1), where the first describes the electronic losses (energy scattered due to the electrons in the medium), and the second describes the nuclear losses which are related to the energy transfer to the kinetic energy of the surrounding atoms.

At low particle velocities the nuclear stopping dominates and the behaviour is mostly ballistic. At higher velocities the electronic terms dominate and energy is mostly transferred into electronic system, where it spreads and will eventually be transferred into the lattice. As the heat conduction through the lattice is much slower, then nuclear stopping is confined in a much smaller region than in the case of the electronic stopping. Therefore, the nuclear stopping will create lattice defects along the trajectory of the projectile. On the other hand electronic stopping will create lattice heating and melting over a much larger region and depending on the homogeneity of the material create defects in various regions in the material.

$$\beta = \frac{S}{v} \tag{6.2}$$

The coupling parameter is defined as the stopping power divided by the velocity of the projectile. This term can be viewed as a constant for the electronic system and; thus, is a property of the material. Namely, the electron-phonon coupling parameter can be used to describe both the phonon lifetime decays as well as the energy transfer from a moving projectile into the electronic decay.

6.3 Electron-phonon coupling

The lattice vibrations of a material scatter the electrons due to the distortions in the lattice. This gives rise to the electron-phonon coupling, where an electron can be excited by a phonon mode or an excited electron can create a phonon mode. The probability of these events can be calculated from the Golden rule of the first-order perturbation theory. The probability of the transition from state $|i\rangle$ to final state $|f\rangle$ due to the interaction Hamiltonian H' is given by the matrix element $\langle f| H' |i\rangle$.

For small atomic displacements the interaction Hamiltonian can be written phenomenologically as

$$H_{ep} = \sum_{\boldsymbol{l},\boldsymbol{b}} \boldsymbol{x}_{\boldsymbol{l},\boldsymbol{b}} \cdot \left[\nabla_{\boldsymbol{x}_{\boldsymbol{l},\boldsymbol{b}}} U(\boldsymbol{r}_e)\right]. \tag{6.3}$$

The summation goes over all lattice cells $\boldsymbol{l}$ and atoms within the cell $\boldsymbol{b}$. The potential is expanded around the ionic equilibrium positions $\boldsymbol{x}_{\boldsymbol{l},\boldsymbol{b}} = 0$ and $\boldsymbol{r}_e$ represents the electronic coordinates. Next, assuming that initial and final states are those of an unperturbed system, i. e. phonon normal modes $|n_{\boldsymbol{q},p}\rangle$ and one-electron eigenfunctions $|\psi_{\boldsymbol{k}}\rangle$, the following formula for transition matrix elements can be derived [78]:

$$\left|T_{\boldsymbol{k},\boldsymbol{k}'}\right| = \sqrt{\frac{\hbar N n_{\boldsymbol{q},p}}{2\omega_{\boldsymbol{q},\boldsymbol{b}}}} \delta^{\boldsymbol{G}_n}_{\boldsymbol{k}'-\boldsymbol{k}-\boldsymbol{q}} \left|H^{\boldsymbol{k},\boldsymbol{k}'}_{\boldsymbol{q},p}\right|, \tag{6.4}$$

where

$$\left|H^{\boldsymbol{k},\boldsymbol{k}'}_{\boldsymbol{q},p}\right| = \left|\int_{\Omega_{BZ}} \psi^*_{\boldsymbol{k}} \sum_{\boldsymbol{b}} \frac{1}{\sqrt{m_{\boldsymbol{b}}}} \boldsymbol{e}^*_{\boldsymbol{q},\boldsymbol{b},p} \cdot \left[\nabla_{\boldsymbol{x}_{\boldsymbol{l},\boldsymbol{b}}} U\right] \psi_{\boldsymbol{k}'} d^3 r\right|. \tag{6.5}$$

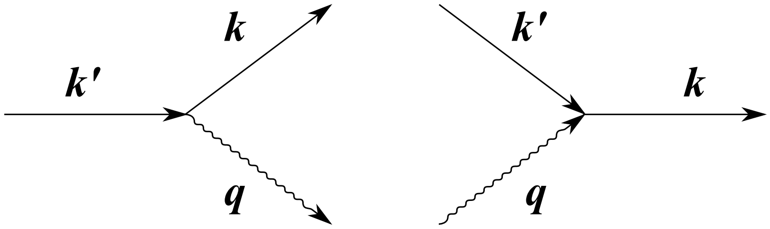

Figure 6.2: Schematic diagrams of electron-phonon scattering within first-order perturbation theory.

Therefore, the selection rules for all allowed electron-phonon processes are related to the conservation of the momentum:

$$\boldsymbol{k}' - \boldsymbol{k} - \boldsymbol{q} = \boldsymbol{G}_n, \tag{6.6}$$

where the $\boldsymbol{G}_n$ is the multiple of the reciprocal cell vector. If in the transition $\boldsymbol{G}_n \neq 0$ then the transition is called umklapp process and normal process otherwise. Due to the energy conservation the number of processes is limited by

$$E_{\boldsymbol{k}'} = E_{\boldsymbol{k}} + \hbar\omega_{\boldsymbol{q},p}. \tag{6.7}$$

As the typical phonon energies are relatively low, most of the transitions occur near the Fermi energy. Also, only the first-order processes are described by Eq. (6.5) and; therefore, higher-order perturbation theory should be used to investigate more complicated processes. The schematic diagrams of the electron-phonon processes that are allowed within current approximations are shown on Fig. 6.2. These processes can be measured directly with slow neutron diffraction.

The dependence of the electron-phonon coupling strength on the polarisation of a phonon mode can be qualitatively investigated by using the rigid-ion approximation where the magnitude of the electron-phonon coupling is proportional to the dot product of the phonon mode polarisation and the difference between of electron initial and final state wave vectors as shown in Eq. (6.8). Therefore, in a normal process there is no electron scattering with the transverse phonon mode. Although the rigid-ion model is a very rough approximation, experimental measurements have shown that for example in Nb crystal the phonon lifetimes of longitudinal modes are shorter than for transverse modes [79] and therefore the electron-phonon coupling of transverse modes is smaller.

$$\left| H_{\boldsymbol{q},p}^{\boldsymbol{k},\boldsymbol{k}'} \right| \propto \boldsymbol{e}_{\boldsymbol{q},p} \cdot (\boldsymbol{k} - \boldsymbol{k}') \tag{6.8}$$

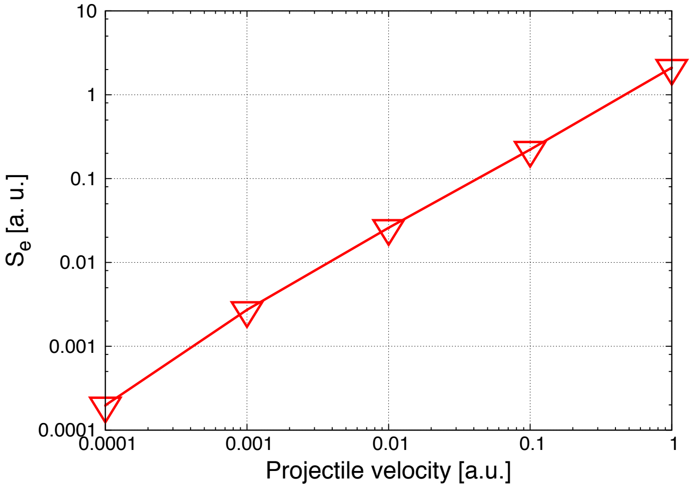

Figure 6.3: The electronic stopping corresponding corresponding to Ni projectile in jellium at metallic electron density for different velocities. The velocities cover the kinetic energies of the electronic stopping regime to the typical thermal phonon regime (Paper III).

6.4 TDDFT study of electronic stopping

The TDDFT simulations allow to capture the energy transfer from a moving projectile into the electronic system. This enables the calculation of electron-ion coupling parameter for various HEA systems with different projectiles. In addition, the exact behaviour of the coupling parameter as a function of local density could be found and used in large scale simulations. In our study we investigated the dependence of this parameter with various velocities and for different local environments for Ni projectile (Paper III).

A major finding was that the stopping power was found to be proportional to the velocity of the projectile (Fig. 6.3). This indicates that the underlying mechanism behind the electronic stopping is the same as the one causing the phonon decay due to electron-phonon scattering. Therefore, the electron-phonon coupling parameter can be obtained from high-velocity TDDFT simulations and be used for simulations of cascade simulations over a wide range of PKA energies.

Next, the coupling parameter of Ni projectile in Ni crystal as a function of local density $\beta(\rho)$ was obtained by moving a projectile across a vacancy. Two

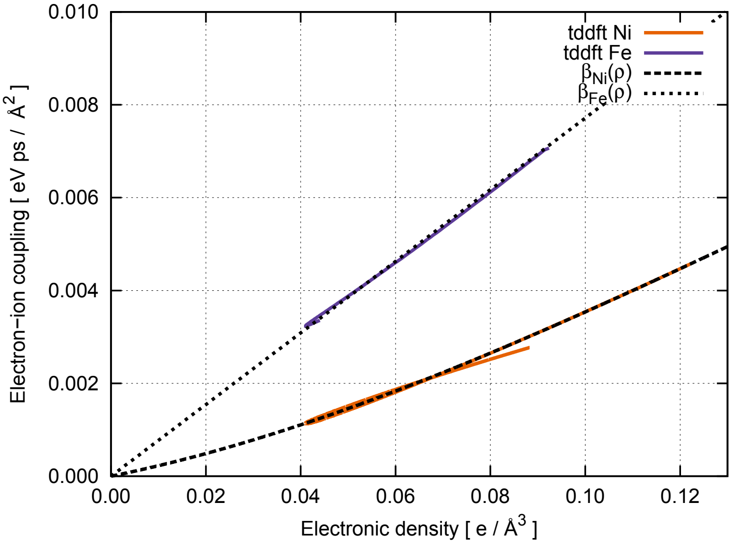

Figure 6.4: The electron-ion coupling parameter as a function of local electronic density calculated using TDDFT for Ni and Fe projectiles moving across a vacancy site in FCC Ni. The dashed lines are fitted quadratic functions used in the MD simulations (Paper IV).

types of simulations were done: first, a simulation with no dissipative terms was conducted to map the variations in the potential energy landscape, next, a TDDFT simulation was done to find the the energy of the whole system with energy transfer to the electronic system. By combining the results of these two functions the stopping power was calculated and the coupling parameter as a function of projectile coordinate was obtained. Finally, the $\beta(\rho)$ term was found by mapping the coordinate of the projectile to the local electronic density at a specific site of the projectile. The same procedure was repeated for a Fe projectile in Ni crystal. The resulting $\beta(\rho)$ function is plotted on Fig. 6.4.

We found that the coupling parameter between Ni atoms is lower than that for Fe atom at the same electronic densities. This indicates that the energy transfer is significantly larger for a Fe projectile and it would slow down faster than Ni projectile. Therefore, the Fe projectile would excite electrons along a smaller path and cause a relatively local heating of the electronic system and eventually heat the lattice within that region. In the case of a Ni projectile the electrons would be excited over a much longer path and; therefore, cause a much lower heating of the lattice but in a larger volume than Fe would cause. This clearly shows that in order to study the radiation damage in a HEA $\beta(\rho)$ functions for all individual components would have to be obtained and taken into account.

6.5 EPH model for classical simulations

Using TDDFT method for large scale collision cascade simulations is unfeasible due to the high computation cost of the method. Therefore, approaches based on classical simulations have to be used. So far the main method for including electronic losses into classical MD simulation has been the two-temperature model proposed by Duffy *et al.* [53]. The main disadvantage of the method is that it uses two separate coupling parameters in the formalism, one for electron-phonon interaction and one for the stopping power regime. Moreover, the latter term is turned off and on with a step function that depends on the velocity of the projectile. Additionally, the coupling parameters are constants that do not depend on the local environment of an atom and they are same for all elements involved in the simulation. This method is not suitable to study the collision cascades in a HEA. Due to the many elements and different local environments, the coupling parameter has to be different for different elements as well as for different electronic densities.

$$m_i \boldsymbol{a}_i = -\nabla_i U - \beta_i(\bar{\rho}_i)\boldsymbol{v}_i^* + \boldsymbol{\eta} \tag{6.9}$$

$$\bar{\rho}_i = \sum_{j \neq i} \rho_j(r_{ij}) \tag{6.10}$$

$$\boldsymbol{v}_i^* = \frac{1}{\bar{\rho}_i} \sum_{j \neq i} \rho_j(r_{ij})(\boldsymbol{v}_i - \boldsymbol{v}_j) \tag{6.11}$$

For this purpose a new method was developed based on the work by Caro *et al.* [52]. The proposed method was implemented into LAMMPS [48] code which was also used for all simulations. In the proposed method the Langevin dynamics governs the motion of individual atoms as shown in Eq. (6.9). The first term in the equation is the force contribution due to the emprirical potential used. The second term describes the dissipation of energy from ions to the electronic system and the final term is the random force that equilibrates the electronic and ionic systems. The e-ph coupling parameter calculated from TDDFT are used for the $\beta(\rho)$. A second-order polynomial was fitted through the calculated values and used as the e-ph coupling parameter at various densities.

The density of a specific site was calculated with Eq. (6.10). Here we assume that each atom contributes to the total density with a spherically

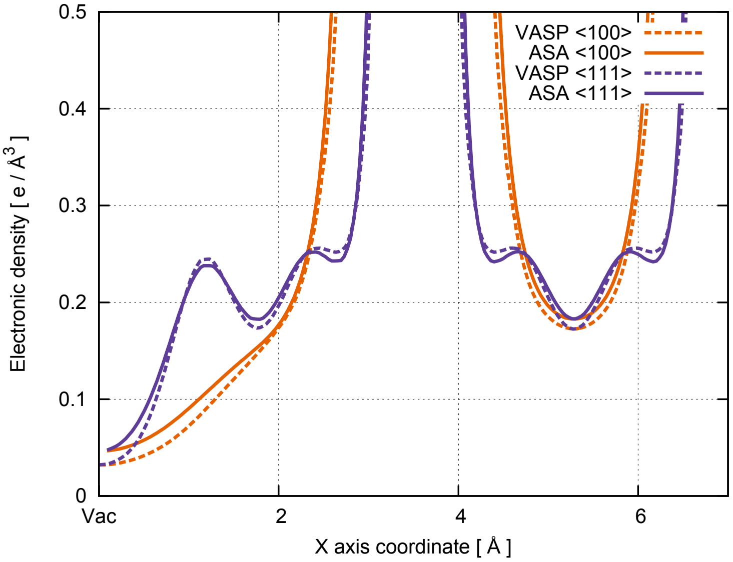

Figure 6.5: Electronic density in FCC Ni crystal with a monovacancy along <100> and <110> directions. The dashed lines are obtained from DFT calculation and the solid line by using ASA approximation (Paper IV).

symmetric function $\rho(r)$ and the total density $\bar{\rho}$ is the superposition of all individual components. This atomic sphere approximation is similar to the method used in the embedding term of EAM potential type. The comparison of ASA method with actual densities obtained from DFT are shown on Fig. 6.5. Although, a rather crude approximation is used the results are in relatively good agreement with DFT results. The ASA method will have more issues in the complex systems where the electronic density is spread in space.

The velocity correction term in Eq. (6.11) was added to give atoms farther away smaller weight in the friction terms and atoms closer larger contribution based on the amount of density contributed to the specific site. Moreover, the correction also removes a major flaw in the current TTM implementation where a crystal with a linear momentum will lose energy and eventually slow down.

The decay of Ni phonon normal modes was selected to test the applicability of the proposed EPH model. In the simulations an initial phonon mode with wave vector $\mathbf{q}$ was created by modulating the displacements of individual atoms with the selected wave vector. The amplitude of the displacements was selected to be 0.0018 Å which is small enough not to have any ph-ph scattering due to anharmonicity of the atomic interactions. Twenty

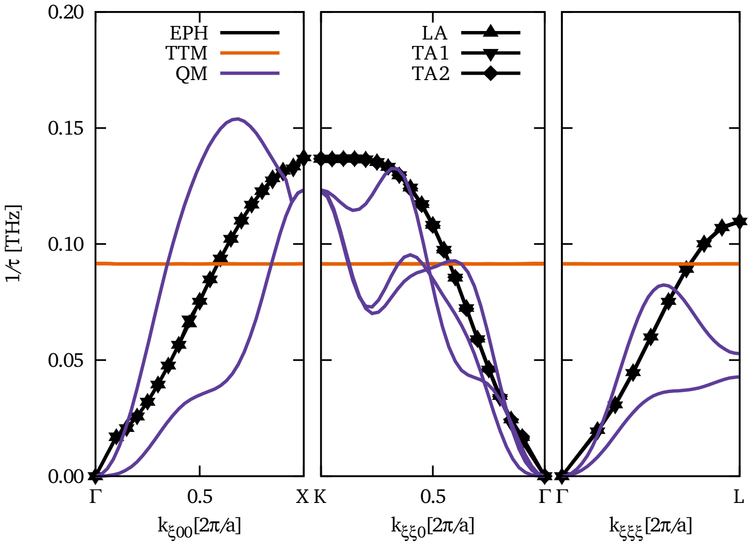

Figure 6.6: Inverse phonon lifetimes in FCC Ni crystal along <100>, <110> and <111> directions. Results are shown for the EPH and TTM models and compared to perturbative QM calculation (Paper IV).

q vectors in <100> and <110> directions and ten in <111> direction were created in the Ni crystal. The size of the system was 20x20x20 conventional FCC cells which limits the number of modes that can be created in the box.

Next, MD simulations were done with and without the dissipative term (the random force term was turned off in all cases). The simulations without the dissipative term would result to simulations in the micro-canonical ensemble and; therefore, the normal modes should not decay at all. Now if the EPH simulations are done the normal mode will decay due to the energy transfer from oscillating atoms to the electronic system. The same type of simulations were also done with TTM model for comparison. Additionally, perturbative QM calculations (Paper IV) were done to see if our approach agrees with the higher level methods. It must be noted that the $\beta(\rho)$ term, although obtained from TDDFT and; thus, being QM in nature, looks only at the local neighbourhood around an atom and; therefore, does not contain any information related to the phonon **q** vector which on the other hand is at the basis of the perturbative QM method. Therefore, all the results are obtained due to the local effects only.

The calculated inverse lifetimes of normal modes in Ni FCC crystal are plotted on Fig. 6.6. It can be clearly seen that phonon modes closer to the edge of the BZ have smaller lifetimes than for the ones closer to the

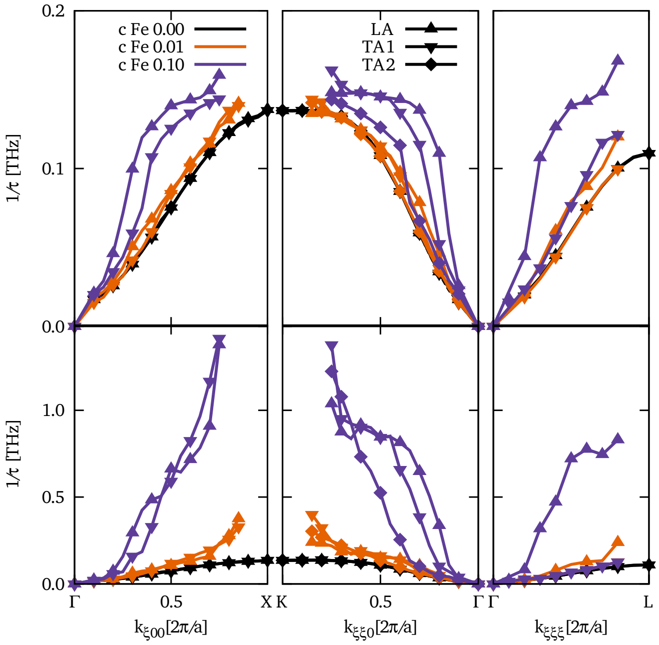

Figure 6.7: Inverse phonon lifetimes for normal modes in a NiFe FCC random solid solution obtained with EPH model. The upper plot shows the interaction of e-ph interactions only and the lower one of both e-ph and ph-ph interactions (Paper IV).

Γ-point. Our results agree relatively well with the ones obtained from QM calculations. The TTM model, on the contrary, predicts a constant phonon lifetime for all the modes. This is mainly caused by the use of the absolute velocity term of individual atoms. The EPH model is not able to predict the splitting in the lifetimes of longitudinal and transverse modes. This could be related to the local angular momentum at each specific site, which currently is not eliminated. Indeed, when eliminating the local angular momenta similarly as done in the work by Mason *et al* [80], the splitting occurs naturally. Unfortunately, the method cannot be used due to other issues that emerge. Therefore, further research has to be conducted.

The proposed method was also applied to study the same phonon modes, as used in pure Ni FCC, in a NiFe FCC random solid solution at various number concentrations of Fe. The e-ph coupling term obtained from TDDFT was used for Fe atoms (Fig. 6.4). The phonon modes should decay faster in this random alloy due to two effects. First, as the Fe atom has a higher coupling parameter than Ni, more energy will be transferred into the electronic system and; therefore, the atoms will slow down faster. Second, due to the introduced disorder the normal modes of pure Ni crystal will not be normal modes for the alloy and; therefore, the initial modes will scatter and the mode will decay into the normal modes of the random alloy.

The inverse phonon lifetimes for NiFe alloy using the EPH method are shown on Fig. 6.7. The e-ph interaction is increased when the concentration of Fe atoms is increased showing that the higher coupling parameter indeed influences the lifetime of the phonon mode. Additionally, when comparing e-ph result to the combined e-ph and disorder effects it can be seen that the disorder has quite a large effect on the decay of the initial mode. Nevertheless, in the radiation damage studies the e-ph interaction part will be higher due to higher velocities and; therefore, should not be neglected. Also, the transferred energy will eventually excite the lattice. Finally, the EPH method should be used in collision cascade simulations of a HEA as it is able to readily handle many-component alloys as well as cover a large region of kinetic energies of the projectile.

6.6 Future concepts

The EPH model has to be modified in order to correctly predict the splitting of longitudinal and transverse modes. Additionally, high energy and density regions have to be explored with EPH model and compared to either TDDFT simulations or to the experiments directly. This in turn would validate the EPH model for use in the collision cascade simulations. Another part of the model that needs to be modified is the heat diffusion equations for the electronic system. Currently a homogeneous electronic density, heat capacitance, and heat conduction is assumed over the whole material. Although this does not affect the results of our simulations it could affect the results of real cascade simulations. In a HEA the density as well as other properties might fluctuate within the crystal and; therefore, the heat dissipation might not be uniform. This in term would affect the heating of the crystal lattice.

As a HEA has five or more elements, a set of five $\rho(r)$ and $\beta(\rho)$ functions is needed in order to use the EPH model. Therefore, a way of calculating the methods in a straightforward way has to be developed. Moreover, a comparison needs to be done on the dependence of the coupling parameter on the host material. Currently, we calculated the $\beta(\rho)$ for both Ni and Fe projectiles in the host FCC Ni crystal. The coupling parameters might, be significantly different for same type of calculations in BCC Fe and should be analysed further. Finally, the magnetic effects might have an impact on the coupling-parameter.

Chapter 7

Conclusions

To sum up, multiple aspects of doing radiation simulations of HEA were studied. First, the recipe for modifying the empirical potentials was proposed. The DFT calculations were done to find the dimer energy of Ni both in vacuum and in the host Ni crystal. It was observed that at interatomic distances smaller than 0.7 Å dimer energies for both vacuum and host crystal match relatively well with ZBL potential and; thus, ZBL should be used at these distances. At intermediate distances (0.7 - 2.2 Å) the discrepancies between the dimer energies in vacuum and in the host crystal arise. Therefore, if collision cascades are to be studied in a host crystal the empirical potential used has to be modified so that the DFT results would be reproduced. The proposed recipe for modification is applied to an EAM type potential for Ni system. Next, the comparative radiation damage simulations in Ni FCC crystal showed that the number of stable Frenkel pairs depends on the modification region and; thus, obtained results are untrustworthy. On the other hand when using our proposed method the number of defects does not depend on the modification region. Also, the proposed method can be readily applied to multi-component systems like HEA.

Secondly, the chemical ordering in Ni-based FCC NiCrCo ternary and NiCrCoFe quaternary HEAs was studied with MC simulations coupled with DFT. It was observed that despite the common random solid solution assumption of HEA the studied systems showed a significant ordering at various temperatures. The most salient results were, that the number of Cr-Cr pairs in both alloys was lower than for the case of a random alloy. In NiCrCoFe quaternary alloy also the number of Fe-Fe pairs was lower than in a random alloy. This is mostly due to the complex magnetic structure of Ni-based alloys where the magnetic frustration of antiferromagnetic Cr results in the spreading of Cr atoms within the system. Therefore, when doing radiation damage studies with HEA alloys the exact atomic structure has to be established, as the chemical ordering could significantly impact the defect production.

Finally, TDDFT calculations were done to study the energy transfer from a moving projectile into the electronic system. It was found that the electronic stopping depends linearly on the velocity. Furthermore, a direct relation between the stopping power and the local electronic density was obtained. This, suggests that both the electron-phonon coupling parameter as well as the interaction due to the electronic stopping can be related to a single density dependent coupling parameter. A new model for including the electronic losses in classical simulations was developed based on the Langevin dynamics. This model was applied to study the phonon lifetimes in Ni FCC crystal and was compared to perturbative QM calculations. The results from both methods agreed relatively well, as opposed to the TTM method currently used. The main discrepancy with QM method was related to the lifetimes of phonon modes with different polarisations, which will be addressed in future work. The proposed method is readily extended to multi-component systems and, therefore, could be used to study the electronic losses with classical MD in HEA.

Chapter 8

Acknowledgements

Part of the research leading to these results has received funding from the European Union Seventh Framework Programme (FP7/2007–2013) under grant agreement nu 263273 and Svenskt Kärntekniskt Centrum (SKC). Computational resources were provided by Swedish National Infrastructure for Computing. Also, part of the work was supported by the Energy Deposition to Defect Evolution (EDDE), an Energy Frontier Research Center funded by the U.S. Department of Energy, Office of Science, Basic Energy Sciences (Award Number 2014 ORNL 1026) at Oak Ridge and Los Alamos National Laboratories.

In addition, resources were provided by European Social Fund's Doctoral Studies and Internationalization Programme DoRa, which is carried out by Foundation Archimedes and Estonian Research Council grant IUT20-24. Moreover, part of this work has been supported by graduate school „Functional materials and technologies“ receiving funding from the European Social Fund under project 1.2.0401.09-0079 in Estonia.

Finally, I would like to thank my supervisors, Alvo Aabloo and Mattias Klintenberg, for their support. Also, I want to thank Alfredo Correa and Arko Kesküla for their important comments related to the thesis. Next, I want to thank Alfredo Caro for many important discussions and for the central role in the making of this thesis. At last, I want to thank my mother and brother and my wife for all the support they provided.

Chapter 9

Summary in Estonian

Kõrge entroopiaga sulamid: struktuuriomadused ja kiirituskoste

Järgmise põlvkonna tuumaelektrijaamades kasutatavad materjalid peavad töötama ekstreemsetes keskkonnatingimustes. Seetõttu otsitakse ja arendatakse uusi materjale, mis oleksid kiirituskindlad, termiliselt stabiilsed ning korrosioonikindlad. Kõrge entroopiaga sulamid on uudne materjalide klass, mis koosneb viiest või enamast põhielemendist ning moodustab ühefaasilise tahke lahuse. Eksperimentidest on leitud, et kõrge entroopiaga sulamitel on paremad mehaanilised omadused kui lähteelementidel, on korrosioonikindlamad ning nende omadused on stabiilsed laias temperatuurivahemikus.

Kõrge entroopiaga sulamite omadusi mõjutavad neli põhilist effekti: kõrge entroopia efekt, aeglase difusiooni efekt, tugev kristallvõre moondumise efekt ning kokteiliefekt. Kuna kõrge entroopiaga sulam koosneb paljudest elementidest, siis maksimaalne konfiguratsioonientroopia saavutatakse aatomite juhusliku jaotuse korral. Selle entroopia panus vabaenergiasse võib olla kõrgematel temperatuuridel piisavalt suur ning seetõttu stabiliseerib selline juhuslik jaotus kristalli võrestruktuuri. Kuna erinevad elemendid on materjalis jaotunud juhuslikult, varieerub kirstallvõre potentsiaal materjalis oluliselt. Madala energiaga pontentsiaalipiirkonnad töötavad lõksudena ning seetõttu on kõrge entroopiaga sulamis difusioon aeglasem kui puhastes elementides. Erinevus aatomi tüüpide suurustes moonutab perfektset kristallvõret, mistõttu on elektronide ning foononite hajumine võimendatud. Selle tulemusel muutuvad mitmed kõrge entroopiaga sulami omadused temperatuurist mittesõltuvaks. Kokteiliefektist lähtudes on võimalik kõrge entroopiaga sulami omadusi mõjutada lisades sobivate omadustega individuaalseid elemente. Näiteks alumiiniumihulga varieerimisega on võimalik muuta CuCoNiCrAlFe kõrge entroopiaga sulami tahkkeskendatud kirstallstruktuuri ruumkeskendatuks.

Kõrge entroopiaga sulamite omadused muudavad nad sobivateks kasutamaks neid kiiritusrohketes keskkondades, kuid hetkeseisuga on vastavaid sulameid vähe uuritud kiirituskindluse seisukohalt. Kiiritustoime uurimiseks on vajalikud arvutisimulatsioonid, sest eksperimentaalsete meetoditega ei ole võimalik mõõta kiireid protsesse nagu põrkekaskaadid. Arvutisimulatsioonid sõltuvad oluliselt kasutatavatest mudelitest ning lähtetingimustest. Käesoleva töö raames uuritakse kolme aspekti, mis mõjutavad kiiritussimulatsioonide tulemusi.

Esiteks uuritakse kvantmehaaniliste meetoditega aatomitevahelist lähimõju interaktsiooni ning pakutakse välja metoodika, kuidas muuta esialgset empiirilist potentsiaali kiiritussimulatsioonide jaoks sobilikuks. Kvantmehaanilistel meetoditel põhinevatest arvutustest selgub, et väikestel kaugustel langeb dimeeri energia kristallis kokku Ziegler, Biersack, ja Littmark potentsiaaliga, kuid vahemikus 0.7 - 2.2 Å erinevus kasvab. Seetõttu peab simulatsioonis kasutatav empiiriline potentsiaal reprodutseerima kvantmehaaniliste arvutuste tulemusi. Muudatuste tegemiseks loodi metoodika, mille tulemusel viiakse empriiriline potentsiaal kvantmehaaniliste tulemustega vastavusse. Protseduuri illustreerimiseks rakendatakse seda nikkli empiirilise potentsiaali parendamiseks ning seda kasutatakse põrkekaskaadide uurimiseks. Võrdluseks korratakse samu simulatsioone potentsiaaliga, mille muutmine toimub siiani levinud meetodil. Tulemustest selgub, et väljapakutud uue protseduuri korral ei sõltu stabiilsete Frenkeli paaride arv sobitamise parameetritest. Samas korreleerus vana meetodi puhul stabiilsete paaride arv otseselt parameetrite valikuga. Lisaks on pakutud meetod rakendatav mitmekomponendiliste süsteemidele nagu näiteks kõrge entroopiaga sulamid.

Teiseks uuritakse kahe kõrge entroopiaga sulami, NiCrCo ja NiCrCoFe, lähikorrastust Monte Carlo meetodil, mis on sidestatud tihedusfunktsionaali teooriaga. Simulatsioone tehakse temperatuuridel: 500, 800 ja 1200 K ning simulatsioonide tulemustest on võimalik hinnata aatomite jaotuse sõltuvust temperatuurist. Simulatsioonide käigus vahetatakse juhuslikult aatomite tüüpe ning seisundite aktsepteerimise tõenäosust määrab Metropolise mudel. Simulatsioonidest järeldub, et NiCrCo sulamis ei ole erinevad elemendid juhuslikult jaotunud. Kroomiumi aatomipaaride arv osutus väiksemaks kui juhuslikult jaotunud sulamis ning nikkli ja kroomiumi paaride arv suuremaks. Neljakomponendilise NiCrCoFe sulami simulatsioonid näitavad, et materjalis ei ole elemendid juhuslikult jaotunud. Sarnaselt kolmekomponendilise süsteemiga on kroomiumipaaride arv väiksem kui juhuslikus süsteemis, kuid lisaks on rauapaaride arv oluliselt väiksem. Tõenäoliselt on selle põhjuseks kroomiumiaatomite antiferromagneetiline olemus, mille puhul on energeetiliselt eelistatum materjalipiirkond, milles on naaberaatomite magnetmoment antiparalleelne kroomiumiaatomi momendiga.

Kolmandaks kasutatakse ajast sõltuvat tihedusfunktsionaali teooriat, et määrata lokaalsest tihedusest sõltuv aatomite ja elektronide sidestusparameeter. Leitud parameetri kasutamiseks klassikalistes simulatsioonides, arendatakse uus meetod LAMMPS tarkvarapaketi jaoks. See meetod baseerub Langevini dünaamikal, kus hõõrdeparameeter asendatakse tihedusest sõltuva sidestusparameetriga. Loodud meetodit rakendatakse foononite kustumise uurimiseks puhtas niklis ning nikli-raua sulamis. Simulatsiooni tulemustest saadi, et pakutud meetodiga arvutatud foononite kustumised on kooskõlas kvantmehaanilistest häiritusarvutustest saadud tulemustega. Lisaks on väljapakutud meetod oluliselt täpsem kui seni kasutatav kahe-temperatuuri mudel. Nimelt esineb uues mudelis foononite kustumisel sõltuvus footoni lainearvust, kuid kahe-temperatuuri korral on footoni kustumine konstante ning seetõttu lainearvust sõltumatu. Põhiliseks probleemiks on hetkel foononite eluea polarisatsioonist sõltuvuse puudumine, mis loodetakse sisse viia edasise töö käigus. Foononite kustumine kiireneb raua koguse suurendamisel nikli-raua sulamis. See tuleneb suuremas osas foononite hajumisest korrapäratuse tõttu ning osaliselt raua suuremast sidestusparameetrist.

Käesolevas töös näidatakse, et kõrge entroopiaga sulamite kiiritussimulatsioonide puhul tuleb empiirilises potentstiaalis teha muudatusi, selleks et väiksetel kaugustel toimuvad protsessid oleksid füüsikaliselt korrektselt kirjeldatud. Lisaks ei pruugi simulatsioonide lähtekonfiguratsioonis olla elemendid juhuslikult jaotunud ning seetõttu tuleb eelnevalt veenduda materjali kristallstruktuuri korrapäras. Lõpetuseks tuleb kõrge entroopiaga sulamite kiiritussimulatsioonides arvestada elektroonsete kadudega, mida võimaldab uurida väljapakutud uudne mudel.

References

[1] *BP statistical review of world energy* (British Petroleum Co., London, 2015).

[2] *GEN-IV*, `http://www.gen-4.org/`.

[3] *ITER*, `http://www.iter.org/`.

[4] F. A. Garner, Recent insights on the swelling and creep of irradiated austenitic alloys, *J. Nucl. Mater.* **122**, 459 (1984).

[5] D. S. Gelles, Void swelling in binary FeCr alloys at 200 dpa, *J. Nucl. Mater.* **225**, 163 (1995).

[6] T. Okita, T. Sato, N. Sekimura, F. A. Garner, and L. R. Greenwood, The primary origin of dose rate effects on microstructural evolution of austenitic alloys during neutron irradiation, *J. Nucl. Mater.* **307-311**, 322 (2002).

[7] S. J. Zinkle, Radiation-Induced Effects on Microstructure, in *Compr. Nucl. Mater.* (Elsevier, 2012), pp. 65–98.

[8] W. J. Phythian and C. A. English, Microstructural evolution in reactor pressure vessel steels, *J. Nucl. Mater.* **205**, 162 (1993).

[9] H. Watanabe, S. Masaki, S. Masubuchi, N. Yoshida, and Y. Kamada, Radiation induced hardening of ion irradiated RPV steels, *J. Nucl. Mater.* **417**, 932 (2011).

[10] X. Zhang, N. Li, O. Anderoglu, H. Wang, J. Swadener, T. Hochbauer, A. Misra, and R. Hoagland, Nanostructured Cu/Nb multilayers subjected to helium ion-irradiation, *Nucl. Instruments Methods Phys. Res. Sect. B Beam Interact. with Mater. Atoms* **261**, 1129 (2007).

[11] N. A. Mara, T. Tamayo, A. V. Sergueeva, X. Zhang, A. Misra, and A. K. Mukherjee, The effects of decreasing layer thickness on the high temperature mechanical behavior of Cu / Nb nanoscale multilayers, *Thin Solid Films* **515**, 3241 (2007).

[12] K. Hattar, M. J. Demkowicz, A. Misra, I. M. Robertson, and R. G. Hoagland, Arrest of He bubble growth in Cu-Nb multilayer nanocomposites, *Scr. Mater.* **58**, 541 (2008).

[13] W. Han, M. J. Demkowicz, N. A. Mara, E. Fu, S. Sinha, A. D. Rollett, Y. Wang, J. S. Carpenter, I. J. Beyerlein, and A. Misra, Design of Radiation Tolerant Materials Via Interface Engineering, *Adv. Mater.* **25**, 6975 (2013).

[14] E. Metsanurk, A. Tamm, A. Caro, A. Aabloo, and M. Klintenberg, First-principles study of point defects at a semicoherent interface, *Sci. Rep.* **4**, 7567 (2014).

[15] C. González, R. Iglesias, and M. J. Demkowicz, Point defect stability in a semicoherent metallic interface, *Phys. Rev. B* **91**, 1 (2015).

[16] C. González and R. Iglesias, Energetic analysis of He and monovacancies in Cu/W metallic interfaces, *Mater. Des.* **91**, 171 (2016).

[17] A. Tamm, E. Metsanurk, A. Caro, A. Aabloo, and M. Klintenberg, Vacancies at CuNb semicoherent interface, *submitted to Phys. Rev. B* (2016).

[18] *Energy Dissipation to Defect Evolution*, `http://edde.ornl.gov/`.

[19] J.-W. Yeh, S.-K. Chen, S.-J. Lin, J.-Y. Gan, T.-S. Chin, T.-T. Shun, C.-H. Tsau, and S.-Y. Chang, Nanostructured High-Entropy Alloys with Multiple Principal Elements: Novel Alloy Design Concepts and Outcomes, *Adv. Eng. Mater.* **6**, 299 (2004).

[20] J.-W. Yeh, Alloy Design Strategies and Future Trends in High-Entropy Alloys, *JOM* **65**, 1759 (2013).

[21] Y. Zhang, T. T. Zuo, Z. Tang, M. C. Gao, K. A. Dahmen, P. K. Liaw, and Z. P. Lu, Microstructures and properties of high-entropy alloys, *Prog. Mater. Sci.* **61**, 1 (2014).

[22] M.-H. Chuang, M.-H. Tsai, W.-R. Wang, S.-J. Lin, and J.-W. Yeh, Microstructure and wear behavior of AlxCo1.5CrFeNi1.5Tiy high-entropy alloys, *Acta Mater.* **59**, 6308 (2011).

[23] C. P. Lee, Y. Y. Chen, C. Y. Hsu, J. W. Yeh, and H. C. Shih, The Effect of Boron on the Corrosion Resistance of the High Entropy Alloys $Al_{0.5}CoCrCuFeNiB_x$, *J. Electrochem. Soc.* **154**, C424 (2007).

[24] F. Granberg, K. Nordlund, M. W. Ullah, K. Jin, C. Lu, H. Bei, L. M. Wang, F. Djurabekova, W. J. Weber, and Y. Zhang, Mechanism of Radiation Damage Reduction in Equiatomic Multicomponent Single Phase Alloys, *Phys. Rev. Lett.* **116**, 135504 (2016).

[25] M. W. Ullah, D. S. Aidhy, Y. Zhang, and W. J. Weber, Damage accumulation in ion-irradiated Ni-based concentrated solid-solution alloys, *Acta Mater.* **109**, 17 (2016).

[26] K. Jin, C. Lu, L. M. Wang, J. Qu, W. J. Weber, Y. Zhang, and H. Bei, Effects of compositional complexity on the ion-irradiation induced swelling and hardening in Ni-containing equiatomic alloys, *Scr. Mater.* **119**, 65 (2016).

[27] A. Takeuchi, K. Amiya, T. Wada, K. Yubuta, and W. Zhang, High-Entropy Alloys with a Hexagonal Close-Packed Structure Designed by Equi-Atomic Alloy Strategy and Binary Phase Diagrams, *Jom* **66**, 1984 (2014).

[28] K.-Y. Tsai, M.-H. Tsai, and J.-W. Yeh, Sluggish diffusion in Co–Cr–Fe–Mn–Ni high-entropy alloys, *Acta Mater.* **61**, 4887 (2013).

[29] O. Senkov, G. Wilks, J. Scott, and D. Miracle, Mechanical properties of Nb25Mo25Ta25W25 and V20Nb20Mo20Ta20W20 refractory high entropy alloys, *Intermetallics* **19**, 698 (2011).

[30] M. Caro, L. Béland, G. Samolyuk, R. Stoller, and A. Caro, Lattice thermal conductivity of multi-component alloys, *J. Alloys Compd.* **648**, 408 (2015).

[31] M. Born and R. Oppenheimer, Zur Quantentheorie der Molekeln, *Ann. Phys.* **389**, 457 (1927).

[32] P. Hohenberg and W. Kohn, Inhomogeneous Electron Gas, *Phys. Rev.* **136**, B864 (1964).

[33] W. Kohn and L. J. Sham, Self-Consistent Equations Including Exchange and Correlation Effects, *Phys. Rev.* **140**, A1133 (1965).

[34] J. P. Perdew and Y. Wang, Accurate and simple analytic representation of the electron-gas correlation energy, *Phys. Rev. B* **45**, 13244 (1992).

[35] P. Haas, F. Tran, and P. Blaha, Calculation of the lattice constant of solids with semilocal functionals, *Phys. Rev. B* **79**, 085104 (2009).

[36] A. van de Walle and G. Ceder, Correcting overbinding in local-density-approximation calculations, *Phys. Rev. B* **59**, 14992 (1999).

[37] J. P. Perdew, K. Burke, and M. Ernzerhof, Generalized Gradient Approximation Made Simple, *Phys. Rev. Lett.* **77**, 3865 (1996).

[38] J. P. Perdew, J. A. Chevary, S. H. Vosko, K. A. Jackson, M. R. Pederson, D. J. Singh, and C. Fiolhais, Atoms, molecules, solids, and surfaces: Applications of the generalized gradient approximation for exchange and correlation, *Phys. Rev. B* **46**, 6671 (1992).

[39] R. Armiento and A. E. Mattsson, Functional designed to include surface effects in self-consistent density functional theory, *Phys. Rev. B* **72**, 085108 (2005).

[40] R. P. Feynman, Forces in Molecules, *Phys. Rev.* **56**, 340 (1939).

[41] E. Runge and E. K. U. Gross, Density-functional theory for time-dependent systems, *Phys. Rev. Lett.* **52**, 997 (1984).

[42] A. Zangwill and P. Soven, Resonant Photoemission in Barium and Cerium, *Phys. Rev. Lett.* **45**, 204 (1980).

[43] A. Zangwill and P. Soven, Resonant two-electron excitation in copper, *Phys. Rev. B* **24**, 4121 (1981).

[44] A. Schleife, E. W. Draeger, Y. Kanai, and A. A. Correa, Plane-wave pseudopotential implementation of explicit integrators for time-dependent Kohn-Sham equations in large-scale simulations, *J. Chem. Phys.* **137**, 0 (2012).

[45] J. M. Pruneda, D. Sánchez-Portal, A. Arnau, J. I. Juaristi, and E. Artacho, Electronic Stopping Power in LiF from First Principles, *Phys. Rev. Lett.* **99**, 235501 (2007).

[46] A. A. Correa, J. Kohanoff, E. Artacho, D. Sánchez-Portal, and A. Caro, Nonadiabatic forces in ion-solid interactions: The initial stages of radiation damage, *Phys. Rev. Lett.* **108**, 1 (2012).

[47] A. Schleife, Y. Kanai, and A. A. Correa, Accurate atomistic first-principles calculations of electronic stopping, *Phys. Rev. B* **91**, 014306 (2015).

[48] S. Plimpton, Fast Parallel Algorithms for Short-Range Molecular Dynamics, *J. Comput. Phys.* **117**, 1 (1995).

[49] G. J. Martyna, M. L. Klein, and M. Tuckerman, Nosé–Hoover chains: The canonical ensemble via continuous dynamics, *J. Chem. Phys.* **97**, 2635 (1992).

[50] L. Bläckberg, E. Metsanurk, A. Tamm, A. Aabloo, and M. Klintenberg, Molecular dynamics study of xenon on an amorphous Al_2O_3 surface,

Nucl. Instruments Methods Phys. Res. Sect. A Accel. Spectrometers, Detect. Assoc. Equip. **759**, 10 (2014).

[51] M. S. Daw and M. I. Baskes, Embedded-atom method: Derivation and application to impurities, surfaces, and other defects in metals, *Phys. Rev. B* **29**, 6443 (1984).

[52] A. Caro and M. Victoria, Ion-electron interaction in molecular-dynamics cascades, *Phys. Rev. A* **40**, 2287 (1989).

[53] D. M. Duffy and A. M. Rutherford, Including the effects of electronic stopping and electron–ion interactions in radiation damage simulations, *J. Phys. Condens. Matter* **19**, 016207 (2007).

[54] W. K. Hastings, Monte Carlo sampling methods using Markov chains and their applications, *Biometrika* **57**, 97 (1970).

[55] A. Caro, D. Crowson, and M. Caro, Classical Many-Body Potential for Concentrated Alloys and the Inversion of Order in Iron-Chromium Alloys, *Phys. Rev. Lett.* **95**, 1 (2005).

[56] A. F. Calder and D. J. Bacon, A molecular dynamics study of displacement cascades in α-iron, *J. Nucl. Mater.* **207**, 25 (1993).

[57] K. Nordlund, J. Keinonen, and A. Kuronen, Effect of the interatomic Si-Si-potential on vacancy production during ion implantation of Si, *Phys. Scr.* **1994**, 34 (1994).

[58] K. Nordlund, N. Runeberg, and D. Sundholm, Repulsive interatomic potentials calculated using Hartree-Fock and density-functional theory methods, *Nucl. Instruments Methods Phys. Res. Sect. B Beam Interact. with Mater. Atoms* **132**, 45 (1997).

[59] N. Juslin and K. Nordlund, Pair potential for Fe–He, *J. Nucl. Mater.* **382**, 143 (2008).

[60] N. Juslin and B. D. Wirth, Interatomic potentials for simulation of He bubble formation in W, *J. Nucl. Mater.* **432**, 61 (2013).

[61] A. P. Bartók, M. C. Payne, R. Kondor, and G. Csányi, Gaussian Approximation Potentials: The Accuracy of Quantum Mechanics, without the Electrons, *Phys. Rev. Lett.* **104**, 136403 (2010).

[62] A. Thompson, L. Swiler, C. Trott, S. Foiles, and G. Tucker, Spectral neighbor analysis method for automated generation of quantum-accurate interatomic potentials, *J. Comput. Phys.* **285**, 316 (2015).

[63] J. Korringa, On the calculation of the energy of a Bloch wave in a metal, *Physica* **13**, 392 (1947).

[64] P. Soven, Coherent-Potential Model of Substitutional Disordered Alloys, *Phys. Rev.* **156**, 809 (1967).

[65] D. W. Taylor, Vibrational Properties of Imperfect Crystals with Large Defect Concentrations, *Phys. Rev.* **156**, 1017 (1967).

[66] G. M. Stocks, W. M. Temmerman, and B. L. Gyorffy, Complete Solution of the Korringa-Kohn-Rostoker Coherent-Potential-Approximation Equations: Cu-Ni Alloys, *Phys. Rev. Lett.* **41**, 339 (1978).

[67] Z. Lin, L. V. Zhigilei, and V. Celli, Electron-phonon coupling and electron heat capacity of metals under conditions of strong electron-phonon nonequilibrium, *Phys. Rev. B - Condens. Matter Mater. Phys.* **77**, 1 (2008).

[68] J. M. Cowley, An Approximate Theory of Order in Alloys, *Phys. Rev.* **77**, 669 (1950).

[69] R. Kikuchi, CVM Entropy Algebra, *Prog. Theor. Phys. Suppl.* **115**, 1 (1994).

[70] W. Schweika and H. Haubold, Neutron-scattering and Monte Carlo study of short-range order and atomic interaction in Ni 0.89 Cr 0.11, *Phys. Rev. B* **37**, 9240 (1988).

[71] B. Schönfeld and L. Reinhard, Short-Range Order and Atomic Displacements in Ni-20 at% Cr Single Crystals, *Phys. status solidi* **148**, 457 (1988).

[72] R. Caudron and M. Sarfati, In situ diffuse scattering of neutrons in alloys and application to phase diagram determination, *J. Phys. I Fr.* **2** (1992).

[73] J. F. Ziegler, M. D. Ziegler, and J. P. Biersack, SRIM - The stopping and range of ions in matter (2010), *Nucl. Instruments Methods Phys. Res. Sect. B Beam Interact. with Mater. Atoms* **268**, 1818 (2010).

[74] R. E. Stoller, M. B. Toloczko, G. S. Was, A. G. Certain, S. Dwaraknath, and F. A. Garner, On the use of SRIM for computing radiation damage exposure, *Nucl. Instruments Methods Phys. Res. Sect. B Beam Interact. with Mater. Atoms* **310**, 75 (2013).

[75] S. Baroni, S. De Gironcoli, A. Dal Corso, and P. Giannozzi, Phonons and related crystal properties from density-functional perturbation theory, *Rev. Mod. Phys.* **73**, 515 (2001).

[76] G. D. Samolyuk, L. K. Béland, G. M. Stocks, and R. E. Stoller, Electron–phonon coupling in Ni-based binary alloys with application to displacement cascade modeling, *J. Phys. Condens. Matter* **28**, 175501 (2016).

[77] HPaul, *Own work, CC BY-SA 3.0*, `https://commons.wikimedia.org/w/index.php?curid=1674656`.

[78] J. Patterson and B. Bailey, *Solid State Physics* (Springer Berlin Heidelberg, Berlin, Heidelberg, 2007), 1st ed., ISBN 978-3-540-24115-7.

[79] W. H. Butler, H. G. Smith, and N. Wakabayashi, Electron-phonon contribution to the phonon linewidth in Nb: Theory and experiment, *Phys. Rev. Lett.* **39**, 1004 (1977).

[80] D. Mason, Incorporating non-adiabatic effects in embedded atom potentials for radiation damage cascade simulations, *J. Phys. Condens. Matter* **27**, 145401 (2015).

Publications

I

Reprinted with permission from R. E. Stoller, A. Tamm, L. K. Beland, G. D. Samolyuk, G. M. Stocks, A. Caro, L. V. Slipchenko, Yu. N. Osetsky, A. Aabloo, M. Klintenberg, and Y. Wang, The Impact of Short-range Forces on Defect Production from High-energy Collisions, Journal of Chemical Theory and Computation 12, 2871-2879, 2016. Copyright 2016 American Chemical Society.

JCTC Journal of Chemical Theory and Computation
Article
pubs.acs.org/JCTC

Impact of Short-Range Forces on Defect Production from High-Energy Collisions

R. E. Stoller,*[†] A. Tamm,[‡,§] L. K. Béland,[†] G. D. Samolyuk,[†] G. M. Stocks,[†] A. Caro,[§] L. V. Slipchenko,[∥] Yu. N. Osetsky,[†] A. Aabloo,[‡] M. Klintenberg,[⊥] and Y. Wang[#]

[†]Materials Science and Technology Division, Oak Ridge National Laboratory, Oak Ridge, Tennessee 37831, United States
[‡]IMS Lab, Institute of Technology, University of Tartu, 50411 Tartu, Estonia
[§]Materials Science and Technology Division, Los Alamos National Laboratory, Los Alamos, New Mexico 87544, United States
[∥]Department of Chemistry, Purdue University, West Lafayette, Indiana 47906, United States
[⊥]Department of Physics and Astronomy, Uppsala University, SE-75120 Uppsala, Sweden
[#]Pittsburgh Supercomputer Center, Carnegie-Mellon University, Pittsburgh, Pennsylvania 15213, United States

Supporting Information

ABSTRACT: Primary radiation damage formation in solid materials typically involves collisions between atoms that have up to a few hundred keV of kinetic energy. During these collisions, the distance between two colliding atoms can approach 0.05 nm. At such small atomic separations, force fields fitted to equilibrium properties tend to significantly underestimate the potential energy of the colliding dimer. To enable molecular dynamics simulations of high-energy collisions, it is common practice to use a screened Coulomb force field to describe the interactions and to smoothly join this to the equilibrium force field at a suitable interatomic spacing. However, there is no accepted standard method for choosing the parameters used in the joining process, and our results prove that defect production is sensitive to how the force fields are linked. A new procedure is presented that involves the use of *ab initio* calculations to determine the magnitude and spatial dependence of the pair interactions at intermediate distances, along with systematic criteria for choosing the joining parameters. Results are presented for the case of nickel, which demonstrate the use and validity of the procedure.

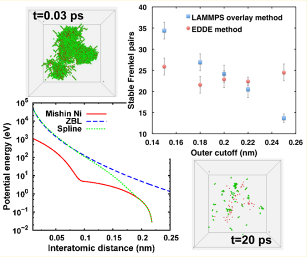

1. INTRODUCTION

Molecular dynamics (MD) simulations are widely used to investigate atomistic and molecular phenomena including applications from biology[1] to materials science.[2,3] Although MD simulations can be used to elucidate the details of many processes on this scale, the primary limitation of the approach is the accuracy with which the force field (alternately interatomic potential) describes the relevant phenomena.[2,4,5] This is a particularly difficult issue when the application of interest involves atoms that are far from their equilibrium positions because the force fields are typically determined by material properties at or near equilibrium. Among the most common properties used in fitting force fields for metals are the lattice parameter, elastic constants, and point and extended defect formation energies.

When metals and alloys are exposed to irradiation by high-energy particles, a process known as a displacement cascade can be initiated.[6] Most simply, this cascade can be visualized as a series of elastic collisions that proceeds after a given atom has been struck by an incident ion (or high-energy neutron in the case of fission reactor materials). The initial atom, which is called the primary knock-on atom (PKA), will recoil with a given amount of kinetic energy, which it dissipates in a sequence of collisions with other atoms. These secondary knock-on atoms will in turn lose energy to third and subsequently higher order knock-ons until all of the energy initially imparted to the PKA has been dissipated. This simple description ignores the fraction of the energy that may be transferred to the electrons in the material. Although the physics is slightly different, similar events are commonly observed on billiard tables. In this context, the most important difference between a rack of billiard balls and atoms in a crystalline solid is the binding forces that arise from the presence of the electrons and other atoms. As a result, a certain minimum kinetic energy must be transferred to an atom before it can be displaced from its lattice site. This is referred to as the displacement threshold energy and is in the range of 20 to 40 eV for most metals.[7]

The collisions of interest to most ion implantation and radiation damage studies involve PKA kinetic energies up to at least a few hundred keV. Collisions at such energies bring atoms very close together, with the colliding dimer eventually reaching potential energies of a few 100 eV. This is well above

Received: December 17, 2015
Published: April 25, 2016

ACS Publications © 2016 American Chemical Society

DOI: 10.1021/acs.jctc.5b01194
J. Chem. Theory Comput. 2016, 12, 2871−2879

the energy range corresponding to equilibrium bonding, which is a few (negative) eV. Force fields fitted to equilibrium properties do not accurately describe the interactions at these short distances and high energies, substantially underestimating the potential energy of the two colliding atoms. At those short distances, collisions may be considered binary, in the sense that most of the potential energy of the system comes from the colliding dimer, with negligible contributions from the other adjacent atoms.[5] In the context of modern many-body force fields used for MD simulations, this fact justifies describing the short-range part of the force field with a pair interaction part alone, with little or no contribution from the many-body embedding term. For example, see the description of the embedded atom model (EAM) or the Finnis-Sinclair force fields.[9] This pair contribution has to be extrapolated from the equilibrium distances where it was fitted to properties of the solid to shorter distances where it has to reproduce a binary collision potential. Figure 1 illustrates this concept with the example of two repulsive pair components from commonly used force fields for iron[9,11] and nickel[10] along with the binary screened-Coulomb "universal" potential obtained by Ziegler, Biersack, and Littmark (ZBL), which is considered an accurate function for high energy collisions.[12]

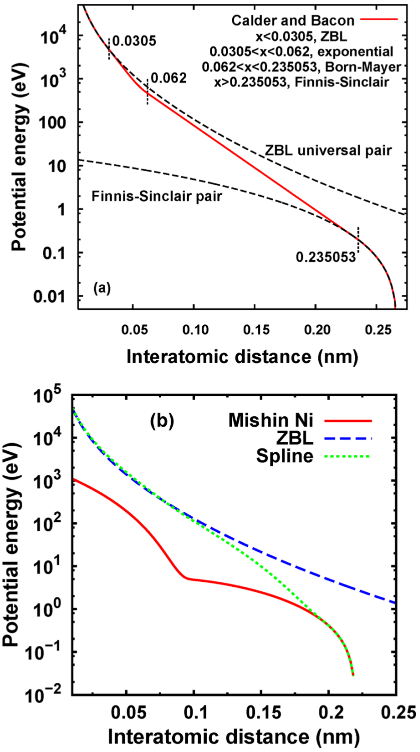

Figure 1. Comparison of screened Coulomb potential by Ziegler, Biersack, and Littmark[10] with repulsive pair term of force fields for (a) iron[8] and (b) nickel.[9] Joining by Calder and Bacon is shown in (a),[11] and a curve labeled Spline in (b) illustrates the LAMMPS overlay method for joining the repulsive term to the ZBL.

It is common practice to smoothly join the ZBL potential to the equilibrium pair force field in order to adequately describe the whole range of distances and energies. The procedure used by Calder and Bacon[11] is illustrated in Figure 1(a) in which two functions were used in this intermediate region join the Finnis-Sinclair and ZBL pair potentials. The curve labeled Spline in Figure 1(b) was obtained using the so-called overlay function in LAMMPS as described in the Supporting Material. The purpose of this paper is to show that one of the most important results of molecular dynamics simulations of high-energy collision cascades, i.e. stable defect production, significantly depends on the value of the repulsive force field precisely in the matching region between ZBL and equilibrium distances. By comparing results obtained in the conventional way and using our newly developed procedure that is based on fitting accurate first-principles energy evaluations in this spatial domain, the necessity of using particular care in this matching region is demonstrated. A procedure which involves the use of *ab initio* calculations to determine the spatial dependence of the close-pair atomic interactions is described, and systematic criteria are defined for choosing the parameters needed to join the equilibrium force field to a ZBL potential. Results are presented for the case of nickel, which demonstrate the use and validity of the procedure. The revised force field provides the same values for equilibrium properties, notably interstitial defects, as the initial one, but the energy and forces obtained for closely spaced pairs of atoms that arise in radiation damage studies are improved. Moreover, the procedure provides a systematic approach that can be followed for any metal or alloy force field.

2. HIGH ENERGY COLLISIONS

In order to determine the interatomic spatial domain explored during a collision cascade, a series of MD simulations were carried out over a wide range of energies and temperatures using a version of the Finnis-Sinclair iron force field[9] which was modified by Calder and Bacon[11] to link with the ZBL. The results shown in Figure 2 demonstrate that for PKA up to 100 keV at 1200K the minimum interatomic distance approaches

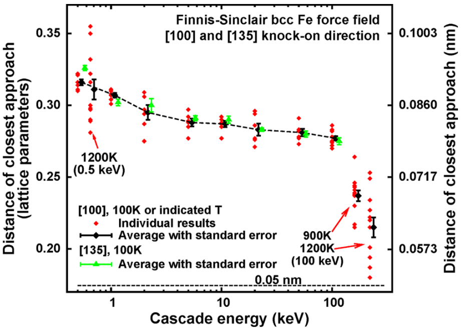

Figure 2. Distance of closest approach for iron atoms as a function of displacement cascade energy and temperature using the modified version of the Finnis-Sinclair force field for iron.[9,11]

0.05 nm. Comparing these values with Figure 1(b), it is clear that many collisions occur in the transition region between the equilibrium and the ZBL components. It is to be expected then that the value of the force field in this region would affect the outcome of the simulation. Previous work involving low energy (<1 keV) events in silicon found relatively little dependence of the repulsive pair interactions on Frenkel pair formation,[13] while limited studies of higher-energy cascade simulations in iron and nickel indicate that defect formation can be sensitive to how the joining is done.[14−17] The most detailed study in ref 17 reported finding a correlation between the number of stable Frenkel pair formed and the stiffness of the force field in the range where the potential energy is a few tens of eV. This is in the transition region between the equilibrium and the ZBL potentials, and they described the joining process as "largely arbitrary". Recently, we have demonstrated the significance to damage production of the high lattice pressures obtained as a consequence of the supersonic shock wave generated in collision cascades.[18] However, there has been no systematic investigation of the impact of the joining methodology on defect production in high-energy MD simulations for metals, and as alluded to in ref 17, there is presently no accepted or standard method for specifying how the two force fields should be joined. Different functional forms such as high-degree polynomials or multiple splines have been used, with different values specified for the spatial domain over which the joining is accomplished. Adding to these limitations, the ZBL potential does not appear to be consistent with *ab initio* calculations in some cases.[19,20]

3. METHODS

The energetics of a Ni dimer were investigated as a function of the distance between the two atoms, both in vacuum and embedded in a crystalline Ni lattice. In the case of the Ni lattice, the energy was obtained by starting from a perfect crystal with the equilibrium lattice parameter and then moving a Ni atom along a ⟨110⟩ direction toward its nearest neighbor, while the rest of the atoms were maintained in perfect lattice positions. The equation of state, EOS, for pure Ni was determined as a function of interatomic distance (pressure) using uniform compression. Several first-principles methods were used to determine this energetics. First, density functional theory (DFT)[21] was used with the PBE exchange-correlation functional.[22] The interaction of valence electrons with ions was described by pseudopotentials with a plane wave basis set as implemented in VASP[23−26] and in Quantum Espresso (QE).[27] Because of the limitations of using pseudopotentials for short distances, similar calculations were performed using two additional methods, namely the Korring-Kohn-Rostoker (KKR) method[28] as implemented within the Locally Self-consistent Multiple Scattering (LSMS) approach[29] for the EOS and an all-electron quantum chemical approach as implemented in Q-Chem 4.2 electronic structure software[30,31] for the dimer in vacuum.

3.1. Calculations Using DFT with Pseudopotentials.

Three types of DFT calculations were performed, namely the following: 1) bulk Ni under extreme compression, 2) a Ni dimer contained in a supercell of Ni atoms, and 3) a Ni dimer in free space. The projector augmented-wave pseudopotential[32,33] for nickel was used in VASP. The selected pseudopotential included the 3p semicore states as valence electrons, which improves the accuracy for short-distance calculations. Two energy cutoff values were used for the plane waves, 350 and 700 eV, to verify energy convergence. The resulting difference in energies was about 2 meV. The Methfessel-Paxton smearing method of the first order[34] with a smearing width of 0.1 eV was applied in all VASP calculations. EOS calculations were done using a conventional cell consisting of 4 atoms with the Monkhorst−Pack method[35] used for Brillouin zone integration on a 28 × 28 × 28 grid. Dimer calculations in bulk material were done using two different supercells of size 2 × 2 × 2 and 3 × 3 × 3 with 32 and 108 atoms in the simulation cell, respectively. The Brillouin zone integration was done on an 8 × 8 × 8 grid for the smaller supercell and 3 × 3 × 3 grid for the larger one. The Ni−Ni dimer in vacuum calculation was done in a simulation cell with a side length of 2.0 nm and used only one gamma point. The use of these parameters resulted in converged total energies.

The QE calculations were done using a plane-wave basis set and an ultrasoft[36] Ni pseudopotential[37] (ni_pbe_v1.uspp.-F.UPF from GBRV database).[38] This potential includes both the 3s and 3p semicore states in the valence electron set. The Brillouin zone summations were carried out over a 24 × 24 × 24 and 8 × 8 × 8 grid in two different sets of calculations. Electronic smearing with a width of 0.272 eV (0.02 Ry) was applied according to the Methfessel-Paxton method.[34] The Kohn−Sham orbitals were expanded in plane waves up to a kinetic-energy cutoff of 1414 eV (104 Ry), whereas plane waves up to 5658 eV (416 Ry) were used to represent the charge density. The 20% increase of cutoff energy changes the energy by less than 0.3 eV for two atoms in an fcc lattice separated by a distance of 0.0353 lattice parameters. Two types of calculations were performed with this code: one to determine the EOS and the other for the Ni dimer energy in a supercell. The EOS was obtained by calculating the total energy as a function of lattice parameter for values between 0.37 and 0.12 nm. In this range, the nearest neighbor distance changes from 0.262 to 0.085 nm. The second type of calculation computed the energy of a Ni−Ni dimer in a supercell containing 2 × 2 × 2 cubic unit cells with the equilibrium lattice parameter.

These plane-wave-based codes have two shortcomings related to the use of pseudopotentials, because the core electrons are not included in the electronic structure calculations. For the short interatomic distances which occur during a displacement cascade, the core electron wave functions of two atoms may overlap, and an all-electron approach is needed. The second shortcoming arises from the fact that the pseudopotential is different than the actual potential at distances shorter that a specified cutoff radius. Thus, at short distances, the electron density is not accurately described, even with so-called "hard" pseudopotentials where this cutoff radius is about 7.94×10^{-11} m (1.5 Bohr radii). This is not important for the modeling of the equilibrium properties of Ni or even the energy of self-interstitial atoms but is significant for cascade modeling. For this reason calculations were also carried out using two all-electron techniques

3.2. KKR Calculations.

The all-electron DFT Korring-Kohn-Rostoker (KKR) method[28] as implemented within the multiple scattering theory (MST) Green's function Locally Self-consistent Multiple Scattering (LSMS) codes[29,39] was used for the calculations of highly compressed fcc Ni. These codes permit the MST Green's function to be calculated using either real or reciprocal space techniques. For this work, the reciprocal space calculation was used to obtain the EOS with the standard KKR band structure method for periodic solids. For all lattice parameters, the lower limit of the energy integration used to calculate the KKR-Green's function, and hence the charge density, was set to include *3s* and *3p* semicore levels. At the equilibrium lattice spacing these states are at approximately −90.2 eV (−6.63 Ry) (*3s*) and −53.3 eV (−3.92 Ry) (*3p*) relative to crystal potential zero and are essentially localized, while at ~55% compression these levels have risen to −41.3 eV (−3.04 Ry) (*3s*) and −7.1 eV (−0.52 Ry) (*3p*) due to their overlap and have a significant bandwidth. The energies and charge densities of the more tightly bound core states were obtained using an atomic-solver. The calculations were performed with a maximum angular momentum cut off of $l_{\max} = 3$. This was then increased to as high as $l_{\max} = 10$ to ensure convergence of the total energy at the smallest lattice parameters. The Brillouin-zone integrations to obtain the KKR scattering-path matrix were performed using a 20 × 20 × 20 k-point mesh. Since a spherical (muffin-tin) approximation to the crystal potential was used, this approach could only be applied for the EOS calculations, because the accuracy of a dimer calculation would be compromised by nonspherical, shear deformations.

3.3. Quantum Chemistry Calculations.

To further verify the energies of the atomic configurations, calculations were also performed for the Ni−Ni dimer in vacuum using the many body techniques of quantum chemistry. These calculations were performed using the coupled cluster with single, double, and perturbative triple excitations method (CCSD(T))[40] with an all-electron 6-31G* basis set[41] with the contraction scheme (22s16p4d1f)/[5s4p2d1f]. The lowest singlet and triplet states were calculated for Ni−Ni separations in the range of 0.05−0.2 nm. The calculations were performed using the Q-Chem 4.2 electronic structure software.[30,31] The unrestricted Hartree−Fock reference was used for describing triplet states. A $^1\Sigma_g^+$ singlet state with the $(d\sigma_g)^2(d\pi_u)^4(d\delta_g)^4(d\delta_u^*)^4(d\pi_g^*)^4(s\sigma_g)^2$ electronic configuration was taken as a reference state. As shown in previous studies of the Ni−Ni dimer, there are many close-lying triplets as well as higher multiplicity states around the equilibrium Ni−Ni separation.[42,43] However, considering that the triplets are expected to be more destabilized than the singlets at shorter Ni−Ni distances and the difficulty of accurately modeling the electronic states of Ni−Ni with single-reference methods, a detailed investigation of electronic structure of the Ni−Ni dimer is left to other studies.

4. RESULTS OF *AB INITIO* CALCULATIONS

First, the results for the total energy of the Ni−Ni dimer in vacuum as a function of interatomic distance obtained from the quantum chemistry methods are presented. As shown in Figure 3, at these short distances and high energies there is essentially no difference observed between the energies of the single and triplet states nor between the HF and the CCSD(T) results. Therefore, the HF results will be used as a basis for comparison with DFT methods in the following discussion.

Figure 4 shows the potential energy of the Ni dimer using different calculation methods as a function of the dimer separation in both vacuum (denoted Ni_2) and embedded in the Ni lattice. The results from two sets of DFT calculations (VASP and QuantumEspresso) for the dimer in the Ni lattice are in good agreement in the range of distances explored, despite the different semicore configurations. At the shorter distances the Ni−Ni dimer energies from DFT are consistent with values from the ZBL universal screened Coulomb potential and the quantum chemistry calculations. The increasing difference between the energies of the dimer in vacuum and the dimer in the lattice as the dimer distance increases is to be expected because it reflects the transition in the collision behavior from being primarily binary to many-bodied. It is evident that the pairwise interaction is dominant for energies above 10 to 100 eV and using the ZBL potential is justified in this range. Below this energy there is a much larger deviation from ZBL, suggesting that values should be obtained from first-principles calculations to describe the interatomic interactions at these larger distances. The figure also suggests that the simpler pseudopotential methods are as accurate at all distances of interest as the more sophisticated methods. This last observation is consistent with the results of Pruneda et al.[20] that showed pseudopotential-based calculations can produce relatively trustworthy results at distances as small as 0.07 nm.

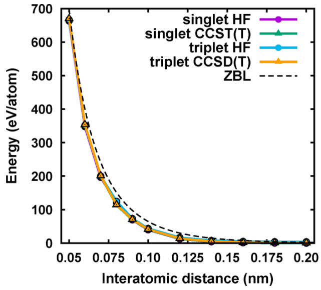

Figure 3. Total energy of Ni−Ni dimer obtained from Q-Chem calculations compared with ZBL pair potential.

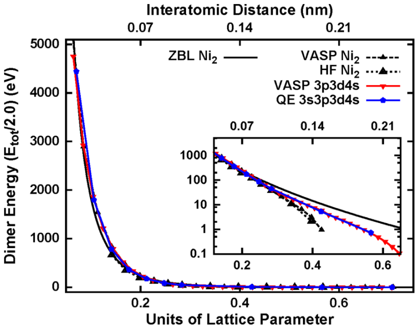

Figure 4. Ni−Ni dimer energy in the fcc Ni lattice and isolated in vacuum (denoted Ni_2).

The EOS for bulk fcc Ni under compression as calculated using the plane wave codes and KKR is shown in Figure 5. The EOS obtained by Rose et al.[44] and Birch−Murnaghan[45] are also included in the figure for comparison. The Rose EOS is based on the experimental lattice parameter, cohesive energy, and bulk modulus, whereas the Birch−Murnaghan equation was fitted to DFT values. Both curves agree well with the calculated values for compressions up to about 20%. Although going beyond this level of compression may be of little relevance for MD simulations, it is important in the development of empirical force fields to avoid unexpected behavior in extreme conditions.

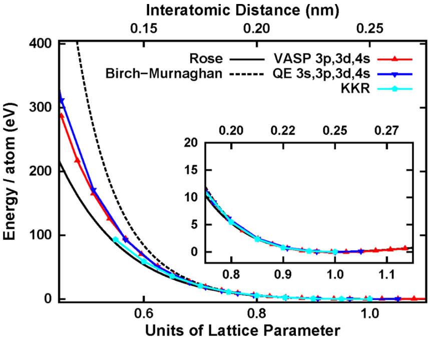

Figure 5. Equation of state for fcc Ni structure.

5. FITTING THE EMPIRICAL FORCE FIELD

In the previous section, results were presented from a diversity of first-principles electronic structure calculation methods applied to the study of the energetics at close separation distance between two atoms both isolated in vacuum and in crystalline lattice. In this section, these results are used to develop an empirical force field capable of capturing both the short and the equilibrium distance behavior. The discussion uses an EAM[8] type of many-body force field as an example, but the method can also be applied using other force field models. The Ni force field by Mishin et al.[10] was selected to illustrate the fitting procedure. The procedure is illustrated in the flowchart shown in Figure 6 and described in the following paragraphs. The Supporting Material provides additional information for computing the EOS and the dimer energy in the EAM formalism.

First, an effective transformation is applied to the EAM force field. This transformation takes advantage of an internal symmetry property of the EAM formalism that allows modifying the embedding energy and the repulsive pair terms simultaneously, without affecting any prediction of the resulting force field. The advantage of the effective transformation is that it creates a force suitable for mixing with other pure element force fields to create alloy force fields. The basic outcome of this transformation is that the density at the equilibrium lattice parameter is unity, and the first derivative of the embedding energy at equilibrium is zero. This transformation is described in more detail elsewhere.[46]

Next, modifications are made to the many-body part of the EAM, namely the density and the embedding functions. The aim is to have the repulsive pair interaction term of the EAM play the major role in describing the resulting energetics as the distance between two atoms decreases. For that to happen the embedding energy term has to become negligible by either becoming constant or very small. There are many ways to achieve this objective, as exemplified in the literature. Here, the density function, $\rho(r)$, is simply modified so that it goes smoothly to zero for $r = 0$. A cubic spline interpolation was used to create a smooth transition from the original density function at $r_\rho = 0.15$ nm to zero. This modification reduces the contribution of the many-body embedding energy term as an atom closely approaches a neighbor and provides the freedom to define the pair interaction term as needed to reproduce the target energetics shown in Figures 4 and 5. To this end the original pair interaction term of the EAM needs to be replaced or modified in two regions: (1) at very short distances, $r < 0.02$ nm, the total energy has to match the ZBL potential and (2) at intermediate distances between $r \geq 0.02$ nm and $r < r_c$, it has to match the target values for the dimer energy in crystalline Ni obtained from DFT calculations. For $r > r_c$ the force field needs to be equal to the original one in order to preserve all its properties. The value of r_c has to be selected with care so that initial equilibrium and defect properties of the pure element force field are not modified, and it is usually chosen to be slightly smaller than the shortest interatomic distance in the saddle point for interstitial migration. In this work, multiple values for r_c were used to test the influence of this parameter on the outcome of collision cascade simulations, as discussed below.

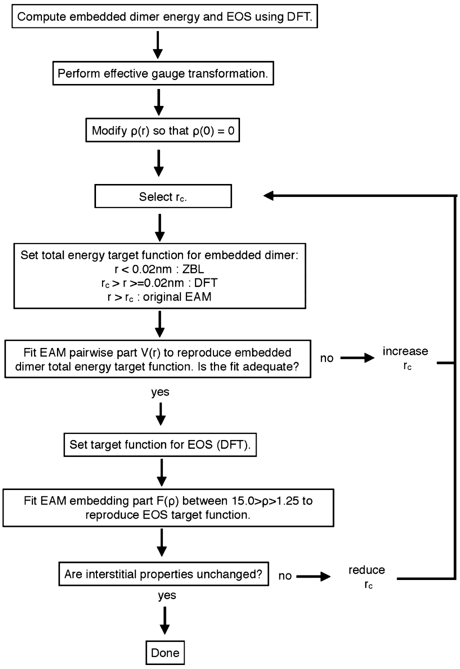
Compute embedded dimer energy and EOS using DFT.
Perform effective gauge transformation.
Modify ρ(r) so that ρ(0) = 0
Select rc.
Set total energy target function for embedded dimer:
r < 0.02nm : ZBL
rc > r >=0.02nm : DFT
r > rc : original EAM
Fit EAM pairwise part V(r) to reproduce embedded dimer total energy target function. Is the fit adequate?
no
increase rc
yes
Set target function for EOS (DFT).
Fit EAM embedding part F(ρ) between 15.0>ρ>1.25 to reproduce EOS target function.
Are interstitial properties unchanged?
no
reduce rc
yes
Done

Figure 6. Flowchart illustrating the newly developed force field fitting procedure described in the text.

The procedure used to obtain the modified version of the repulsive pair interaction over the complete range of interest can be summarized as follows. First, a cubic spline was used to fit the 12 DFT energy values between 0.04 and 0.25 nm, and values were extracted for a set of knot points with a step size of 0.1 nm between 0.04 nm and (r_c-0.02) nm. Then, the appropriate ZBL function was tabulated from 0 to 0.02 nm with a step size of 0.001 nm. Next, the pair component of the original EAM potential was tabulated using the same step size between r_c and the cutoff radius of the potential (0.65 nm for the Mishin Ni). Finally, a cubic spline interpolation was used to fit the energy values over the entire range of the tabulated ZBL points, DFT-fitted knot points, and tabulated EAM points from 0 to the 0.65 nm EAM potential cutoff. The need to match different functions and their first derivatives at a given point requires defining a transition region around that point where there is an arbitrary function with at least four degrees of freedom (two function values and two first derivatives). Although a simple cubic spline was used demonstrate the methodology in this paper, it would be appropriate to use a higher order spline in practice to maintain the continuity of the second derivative at the joining points, particularly when the Verlet method is used to integrate the equations of motion. In order to match the ZBL and DFT values, one knot was specified in the region between 0.02 and 0.04 nm. Similarly, one knot was specified in the matching region between DFT and EAM, *i.e.* between r_c and $(r_c\text{-}0.02)$ nm. An example of the results obtained by this fitting procedure is shown in Figure 7 for r_c = 0.2 nm; the knot points for the cubic spline are listed in Table 1. Finally, to correctly reproduce the EOS as given by the DFT calculations shown in Figure 5, a correction to the embedding function $F(\rho)$ was introduced without further modification of the pair term. The $F(\rho)$ function was smoothly joined to the EOS using cubic splines in the region $1.25 < \rho < 15.0$.

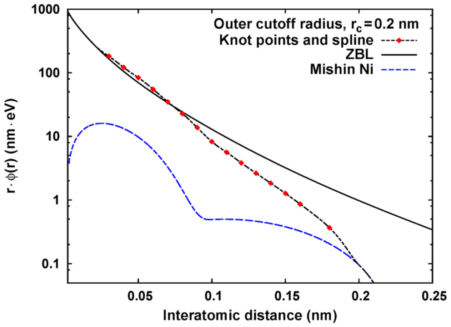

Figure 7. Knot points used to obtain DFT-based cubic spline fit joining repulsive ZBL and Mishin pair potentials, see Table 1 for knot point values.

Fitting of the force fields was done using the software package *octave*[47] with the cost function to be minimized defined as

$$f = \sum_{i=1}^{N} \sqrt{|E_{DFT}(r_i) - E_{EAM}(r_i)|} \tag{1}$$

The term $E_{DFT}(r_i)$ in eq 1 is either the dimer or the EOS energy at separation r_i, and $E_{EAM}(r_i)$ is the energy given by the EAM force field evaluated analytically. Minimization was done in two steps; first, a global minimization with a controlled random search with local mutations[48] algorithm, and second, a local minimization with the BOBYQA[49] algorithm. Both, algorithms were provided by the *nlopt* package.[50]

6. DEFECT PRODUCTION

In order to assess the impact of the different force fields on defect production, MD simulations of 10 keV displacement cascades were performed using the software package LAMMPS.[51] The primary knock-on atom was given this initial kinetic energy with velocity in the ⟨1 3 5⟩ direction in a simulation cell of 40 × 40 × 40 a_o^3 (256,000 atoms). Runs were performed in the NVE ensemble. Prior to the cascade, the system was equilibrated at 300 K and zero pressure. A variable time step was used to maintain the required accuracy when integrating the atomic equations of motion. The momentum in the outer layers of the simulation cell was periodically reset to zero during the simulation to prevent drift in response to the energy input from the PKA. Defects were identified using a Wigner-Seitz analysis after the displacement cascade event was complete at ∼20 ps, well after the number of defects has stabilized.[6]

Five force fields were generated to provide a basis of comparison in these simulations. Two different methods were employed with different outer cutoff radii r_c to reproduce the DFT dimer energy as well as the EOS. One method employed the "overlay" function of LAMMPS[52] to join the ZBL potential to the Mishin Ni EAM, and the second method is the one developed for this work and described above. The cutoff radii used were 0.15, 0.18, 0.20, 0.22, and 0.25 nm. Selection of these

Table 1. Knot Points Used To Obtain a Cubic Spline Fit Joining the ZBL Potential and the Repulsive Pair Component of the Mishin Ni EAM Force Field

interatomic distance (nm)	r_c = 0.15 nm	r_c = 0.18 nm	r_c = 0.20 nm
0.30	1838.33294982888	1838.31649327955	1820.22954714512
0.40	1218.05081969406	1218.04960771924	1214.50276956392
0.50	836.163674505376	836.164080148673	836.820573806760
0.60	551.866516156028	551.8.68157033055	551.951588102543
0.70	348.671359126630	348.639132989473	348.639125254940
0.80	227.100588117360	227.100892683067	227.162921150792
0.90	137.420547993645	137.400611108088	137.513053051492
1.00	82.6828351738512	82.7297523191666	82.6806394078697
1.10	56.4812921897848	56.0356985870809	56.1492920892016
1.20		38.2689909285101	38.2789943639836
1.30	19.0500680138810	26.3581592073729	26.3690768994141
1.40			18.3864402991851
1.50		12.5545167549024	12.7103709552707
1.60			8.61297228349303
1.80			3.65754272432989

values does not affect the fitting of the EOS but has a major impact on the dimer energy as can be seen in Figure 8. For the Ni system the best value for r_c was found to be 0.20 nm. With this value, the force field provides good agreement with the DFT dimer energies while at the same time not altering the interstitial defect energies predicted by the initial EAM force field. An inner cutoff radius of 0.04 nm was used in all cases. This led to ten different variants of the Ni force field that were used in the MD simulations.

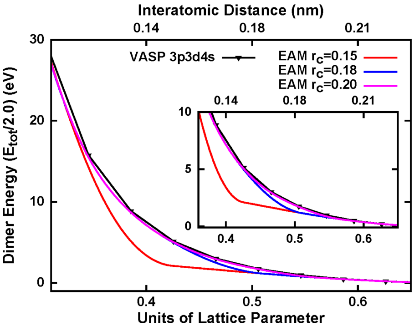

Figure 8. Fitting results obtained with different values of the cutoff radius r_c compared to the target function from VASP.

The results are summarized in Table 2 and shown in Figure 9 where the indicated uncertainty and error bars are the standard error based on 15 runs for each case. Two observations can readily be made from this figure and the data in Table 2. First is that matching the ZBL to EAM with an arbitrary function in an arbitrary distance window can change the defect production by almost a factor of 3. Second is that a proper choice of the energy function for the intermediate region between ZBL and EAM, based on *ab initio* results using the method proposed in this work, gives a number of defects that is nearly independent of the outer cutoff radius for the matching region. It should be noted that the data in Table 2 indicates that the change in the number of stable defects produced does not arise from a change in the interstitial formation energy. Only for the largest value of r_c is there a significant change in this formation energy.

Table 2. Average Number of Stable Frenkel Pair Produced by 10 keV Displacement Cascades with Different Hardening Methods and Parameters[a]

outer cutoff radius (nm)	LAMMPS overlay[52]	EDDE method
0.15	34.4 ± 2 (3.97 eV)	25.9 ± 2 (3.98 eV)
0.18	26.9 ± 2 (3.97 eV)	21.6 ± 2 (3.98 eV)
0.20	24.2 ± 2 (3.97 eV)	22.9 ± 2 (3.98 eV)
0.22	20.5 ± 2 (4.07 eV)	22.4 ± 1 (4.10 eV)
0.25	13.7 ± 1 (7.16 eV)	24.5 ± 2 (3.70 eV)

[a] Corresponding interstitial formation energy is noted in parentheses.

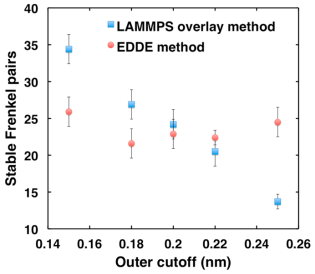

Figure 9. Average number of stable Frenkel pair produced by 10 keV displacement cascades with different hardening methods and parameters, error bars denote standard error.

7. DISCUSSION AND CONCLUSIONS

The force fields or interatomic potentials, such as the commonly used EAM, that are generally designed to describe the bulk, equilibrium properties of metals do not accurately predict the high-energy interactions that are encountered when materials are irradiated with energetic particles. For these high energy collisions, the interatomic separation of the colliding dimer can be much less than the equilibrium lattice parameter and the repulsive pair term has to be "hardened" to reproduce the scattering potential corresponding to the atomic species colliding. This has traditionally been done by matching the pair term of the full force field to the ZBL potential at a specified interatomic spacing. This matching is implemented with an arbitrary function within an arbitrary region of space, with the constraint that the function has to provide enough freedom to match the equilibrium force field and its derivatives at the edges of the matching region (e.g., the ZBL at the lower limit and EAM at the upper limit) and has to leave the properties predicted by the original force field unperturbed beyond the upper limit. This work has demonstrated that the atomic collisions taking place within the matching region play a significant role in determining the number of defects that are ultimately created and has shown that using first-principles techniques makes it possible to accurately calculate the energy of interatomic interactions in this transition.

Therefore, a new procedure has been developed that maintains the accuracy of the equilibrium force fields in their relevant domain while providing a bridge to the very short atomic separation distances where interatomic forces can be obtained from a screened Coulomb potential (e.g., the ZBL universal potential[12]). This procedure involves the use of *ab initio* calculations to determine the magnitude and spatial dependence of the pair interactions at intermediate distances, along with a systematic approach to choosing the appropriate criteria for joining the different components of the force field. The criteria include providing consistency with the *ab initio* results while maintaining the predictions of the equilibrium force field for the properties of interstitial defects. The results shown for the case of an EAM nickel and the ZBL demonstrate the use and validity of the procedure which will be suitable for other metals and alloys. Since the focus of this work is displacement damage production in the lattice, the dimer energy in the lattice was used in the fitting process. However, the data in Figure 4 demonstrate that for dimer energies greater than about 10 eV there is little difference between the dimer in the lattice and in vacuum. This suggests that the procedure adopted here should also be suitable for the energetic collisions associated with ion irradiation.

With our new procedure, two matching regions need to be defined: one between the ZBL and the first-principles results and one between the first-principles results and the EAM. The results presented here have shown that by reducing the arbitrariness of the energy function in the region between ZBL and EAM, a force field that is minimally dependent on the points where the matching is made can be obtained, giving more confidence on the accuracy of the simulation results. Unfortunately, there are no experimental data available on defect production from these short-time (~20 ps) collision processes that can be used to directly validate the models. However, it is generally valid to assume that the more physics-based input a model has, the more accurate its predictions are expected to be.

■ ASSOCIATED CONTENT

Ⓢ Supporting Information

The Supporting Information is available free of charge on the ACS Publications website at DOI: 10.1021/acs.jctc.5b01194.

> Description of a material's equation of state and the dimer energy in the context of the embedded atom model for the interatomic force fields and description of the LAMMPS overlay method for joining an equilibrium force field to a short-ranged, screened-Coulomb potential (PDF)

■ AUTHOR INFORMATION

Corresponding Author

*E-mail: rkn@ornl.gov.

Notes

The authors declare no competing financial interest.

■ ACKNOWLEDGMENTS

This work was supported as part of the Energy Dissipation to Defect Evolution (EDDE), an Energy Frontier Research Center funded by the U.S. Department of Energy, Office of Science, Basic Energy Sciences. L.K.B. acknowledges additional support from a fellowship awarded by the Fonds Québécois de recherche Nature et Technologies. L.V.S. acknowledges support for computational resources provided by Information Technology at Purdue University, West Lafayette, Indiana.

■ REFERENCES

(1) Piana, S.; Klepeis, J. J.; Shaw, D. E. *Curr. Opin. Struct. Biol.* **2014**, *24*, 98−105.

(2) Massobrio, C.; Blandin, P. Classical and First Principles Molecular Dynamics Simulations in Material Science: Application to Structural and Dynamical Properties of Free and Supported Clusters. In *Stability of Materials*; Gonis, A., Turchi, P. E. A., Kudrnovský, J., Eds.; NATO Science Series B: 355, Plenum Press: New York, 1996; pp 295−324.

(3) Cai, W.; Li, J.; Yip, S. Molecular Dynamics. In *Comprehensive Nuclear Materials*, Konings, R. J. M., Allen, T. R., Stoller, R. E., Tamanaka, S., Eds.; Elsevier Ltd.: Amsterdam, 2012; pp 249−265.

(4) Finnis, M. W. *Interatomic Forces in Condensed Matter*; Oxford University Press: Oxford, 2003; pp 129−154, 253−262.

(5) Ackland, G. J. Interatomic Potential Development. In *Comprehensive Nuclear Materials*; Konings, R. J. M., Allen, T. R., Stoller, R. E., Tamanaka, S., Eds.; Elsevier Ltd.: Amsterdam, 2012; pp 267−291.

(6) Stoller, R. E. Primary Radiation Damage Formation. In *Comprehensive Nuclear Materials*; Konings, R. J. M., Allen, T. R., Stoller, R. E., Tamanaka, S., Eds.; Elsevier Ltd.: Amsterdam, 2012; pp 293−332.

(7) ASTM E521, *Standard Practice for Neutron Radiation Damage Simulation by Charged Particle Irradiation*; Annual Book of ASTM Standards, Vol. *12.02*, ASTM International: West Conshohocken, PA, DOI: 10.1520/E0521-96R09E02.

(8) Daw, M. S.; Baskes, M. I. *Phys. Rev. B: Condens. Matter Mater. Phys.* **1984**, *29*, 6443−6453.

(9) Finnis, M. W.; Sinclair, J. E. *Philos. Mag. A* **1984**, *50*, 45−54; Erratum. *Philos. Mag. A* **1986**, *53*, 161.

(10) Mishin, Y.; Farkas, D.; Mehl, M. J.; Papaconstantopoulos, D. A. *Phys. Rev. B: Condens. Matter Mater. Phys.* **1999**, *59*, 3393−3407.

(11) Calder, A. F.; Bacon, D. J. *J. Nucl. Mater.* **1993**, *207*, 25−45.

(12) Ziegler, J. F.; Biersack, J. P.; Littmark, U. *The Stopping and Range of Ions in Solids*, 1st ed.; Pergamon Press: New York, 1985; pp 41−67.

(13) Nordlund, K.; Keinonen, J.; Kuronen, A. *Phys. Scr.* **1994**, *T54*, 34−37.

(14) Becquart, C. S.; Domain, C.; Legris, A.; Van Duysen, J. C. *J. Nucl. Mater.* **2000**, *280*, 73−85.

(15) Malerba, L. *J. Nucl. Mater.* **2006**, *351*, 28−38.

(16) Terentyev, D.; Lagerstedt, C.; Olsson, P.; Nordlund, K.; Wallenius, J.; Becquart, C. S.; Malerba, L. *J. Nucl. Mater.* **2006**, *351*, 65−77.

(17) Yao, Z.; Caturla, M. J.; Schäublin, R. *J. Nucl. Mater.* **2007**, *367−370*, 298−304.

(18) Béland, L. K.; Osetsky, Yu. N.; Stoller, R. E. Atomistic material behavior at extreme pressures. *npj Computational Materials*, accepted April 2016, DOI: 10.1038/npjcompumats.2016.7.

(19) Nordlund, K.; Runeberg, N.; Sundholm, D. *Nucl. Instrum. Methods Phys. Res., Sect. B* **1997**, *132*, 45−54.

(20) Pruneda, J. M.; Artacho, E. *Phys. Rev. B: Condens. Matter Mater. Phys.* **2004**, *70*, 0401265:1−0401265:7.

(21) Kohn, W.; Sham, L. J. *Phys. Rev.* **1965**, *140*, A1133−A1138.

(22) Perdew, J. P.; Burke, K.; Ernzerhof, M. *Phys. Rev. Lett.* **1996**, *77*, 3865−3868.

(23) Kresse, G.; Hafner, J. *Phys. Rev. B: Condens. Matter Mater. Phys.* **1993**, *47*, 558−561.

(24) Kresse, G.; Hafner, J. *Phys. Rev. B: Condens. Matter Mater. Phys.* **1994**, *49*, 14251−14269.

(25) Kresse, G.; Furthmüller, J. *Comput. Mater. Sci.* **1996**, *6*, 15−50.

(26) Kresse, G.; Furthmüller, J. *Phys. Rev. B: Condens. Matter Mater. Phys.* **1996**, *54*, 11169−11186.

(27) Giannozzi, P.; Baroni, S.; Bonini, N.; Calandra, M.; Car, R.; Cavazzoni, C.; Ceresoli, D.; Chiarotti, G. L.; Cococcioni, M.; Dabo, I.; DalCorso, A.; Fabris, S.; Fratesi, G.; de Gironcoli, S.; Gebauer, R.; Gerstmann, U.; Gougoussis, C.; Kokalj, A.; Lazzeri, M.; Martin-Samos, L.; Marzari, N.; Mauri, F.; Mazzarello, R.; Paolini, S.; Pasquarello, A.; Paulatto, L.; Sbraccia, C.; Scandolo, S.; Sclauzero, G.; Seitsonen, A. P.; Smogunov, A.; Umari, P.; Wentzcovitch, R. M. *J. Phys.: Condens. Matter* **2009**, *21*, 395502.

(28) Korringa, J. *Physica* **1947**, *13*, 392−400.

(29) Wang, Y.; Stocks, G. M.; Shelton, W. A.; Nicholson, D. M.; Szotek, Z.; Temmerman, W. *Phys. Rev. Lett.* **1995**, *75*, 2867−2870.

(30) Shao, Y.; Molnar, L. F.; Jung, Y.; Kussmann, J.; Ochsenfeld, C.; Brown, S. T.; Gilbert, A. T. B.; Slipchenko, L. V.; Levchenko, S. V.; O'Neill, D. P.; DiStasio, R. A., Jr.; Lochan, R. C.; Wang, T.; Beran, G. J. O.; Besley, N. A.; Herbert, J. M.; Lin, C. Y.; Van Voorhis, T.; Chien, S. H.; Sodt, A.; Steele, R. P.; Rassolov, V. A.; Maslen, P. E.; Korambath, P. P.; Adamson, R. D.; Austin, B.; Baker, J.; Byrd, E. F. C.; Dachsel, H.; Doerksen, R. J.; Dreuw, A.; Dunietz, B. D.; Dutoi, A. D.; Furlani, T. R.; Gwaltney, S. R.; Heyden, A.; Hirata, S.; Hsu, C.-P.; Kedziora, G.; Khalliulin, R. Z.; Klunzinger, P.; Lee, A. M.; Lee, M. S.; Liang, W.; Lotan, I.; Nair, N.; Peters, B.; Proynov, E. I.; Pieniazek, P. A.; Rhee, Y. M.; Ritchie, J.; Rosta, E.; Sherrill, C. D.; Simmonett, A. C.; Subotnik, J. E.; Woodcock, H. L., III; Zhang, W.; Bell, A. T.; Chakraborty, A. K.; Chipman, D. M.; Keil, F. J.; Warshel, A.; Hehre, W. J.; Schaefer, H. F., III; Kong, J.; Krylov, A. I.; Gill, P. M.; Head-Gordon, M. *Phys. Chem. Chem. Phys.* **2006**, *8*, 3172−3191.

(31) Shao, Y.; Gan, Z.; Epifanovsky, E.; Gilbert, A. T. B.; Wormit, M.; Kussmann, J.; Lange, A. W.; Behn, A.; Deng, J.; Feng, X.; Ghosh, D.; Goldey, M.; Horn, P. R.; Jacobson, L. D.; Kaliman, I.; Khaliullin, R. Z.;

Kus, T.; Landau, A.; Liu, J.; Proynov, E. I.; Rhee, Y. M.; Richard, R. M.; Rohrdanz, M. A.; Steele, R. P.; Sundstrom, E. J.; Woodcock, H. L., III; Zimmerman, P. M.; Zuev, D.; Albrecht, B.; Alguire, E.; Austin, B.; Beran, G. J. O.; Bernard, Y. A.; Berquist, E.; Brandhorst, K.; Bravaya, K. B.; Brown, S. T.; Casanova, D.; Chang, C.-M.; Chen, Y.; Chien, S. H.; Closser, K. D.; Crittenden, D. L.; Diedenhofen, M.; DiStasio, R. A., Jr.; Do, H.; Dutoi, A. D.; Edgar, R. G.; Fatehi, S.; Fusti-Molnar, L.; Ghysels, A.; Golubeva-Zadorozhnaya, A.; Gomes, J.; Hanson-Heine, M. W. D.; Harbach, P. H. P.; Hauser, A. W.; Hohenstein, E. G.; Holden, Z. C.; Jagau, T.-C.; Ji, H.; Kaduk, B.; Khistyaev, K.; Kim, J.; Kim, J.; King, R. A.; Klunzinger, P.; Kosenkov, D.; Kowalczyk, T.; Krauter, C. M.; Lao, K. U.; Laurent, A. D.; Lawler, K. V.; Levchenko, S. V.; Lin, C. Y.; Liu, F.; Livshits, E.; Lochan, R. C.; Luenser, A.; Manohar, P.; Manzer, S. F.; Mao, S.-P.; Mardirossian, N.; Marenich, A. V.; Maurer, S. A.; Mayhall, N. J.; Neuscamman, E.; Oana, C. M.; Olivares-Amaya, R.; O'Neill, D. P.; Parkhill, J. A.; Perrine, T. M.; Peverati, R.; Prociuk, A.; Rehn, D. R.; Rosta, E.; Russ, N. J.; Sharada, S. M.; Sharma, S.; Small, D. W.; Sodt, A.; Stein, T.; Stuck, D.; Su, Y.-C.; Thom, A. J. W.; Tsuchimochi, T.; Vanovschi, V.; Vogt, L.; Vydrov, O.; Wang, T.; Watson, M. A.; Wenzel, J.; White, A.; Williams, C. F.; Yang, J.; Yeganeh, S.; Yost, S. R.; You, Z.-Q.; Zhang, I. Y.; Zhang, X.; Zhao, Y.; Brooks, B. R.; Chan, G. K. L.; Chipman, D. M.; Cramer, C. J.; Goddard, W. A., III; Gordon, M. S.; Hehre, W. J.; Klamt, A.; Schaefer, H. F., III; Schmidt, M. W.; Sherrill, C. D.; Truhlar, D. G.; Warshel, A.; Xu, X.; Aspuru-Guzik, A.; Baer, R.; Bell, A. T.; Besley, N. A.; Chai, J.-D.; Dreuw, A.; Dunietz, B. D.; Furlani, T. R.; Gwaltney, S. R.; Hsu, C.-P.; Jung, Y.; Kong, J.; Lambrecht, D. S.; Liang, W.; Ochsenfeld, C.; Rassolov, V. A.; Slipchenko, L. V.; Subotnik, J. E.; Van Voorhis, T.; Herbert, J. M.; Krylov, A. I.; Gill, P. M. W.; Head-Gordon, M. *Mol. Phys.* **2015**, *113*, 184−215.

(32) Blöchl, P. E. *Phys. Rev. B: Condens. Matter Mater. Phys.* **1994**, *50*, 17953−17979.

(33) Kresse, G.; Joubert, D. *Phys. Rev. B: Condens. Matter Mater. Phys.* **1999**, *59*, 1758−1775.

(34) Methfessel, M.; Paxton, A. T. *Phys. Rev. B: Condens. Matter Mater. Phys.* **1989**, *40*, 3616−3621.

(35) Monkhorst, H.; Pack, J. *Phys. Rev. B* **1976**, *13*, 5188−5192.

(36) Vanderbilt, D. *Phys. Rev. B: Condens. Matter Mater. Phys.* **1990**, *41*, 7892−7895.

(37) Garrity, K. F.; Bennett, J. W.; Rabe, K. M.; Vanderbilt, D. *Comput. Mater. Sci.* **2014**, *81*, 446−452.

(38) GBRV High-throughput Pseudopotentials. http://www.physics.rutgers.edu/gbrv/ (accessed Dec 15, 2015).

(39) Faulkner, J. S.; Stocks, G. M. *Phys. Rev. B: Condens. Matter Mater. Phys.* **1980**, *21*, 3222−3244.

(40) Raghavachari, K.; Trucks, G. W.; Pople, J. A.; Head-Gordon, M. *Chem. Phys. Lett.* **1989**, *157*, 479−483.

(41) Rassolov, V.; Pople, J. A.; Ratner, M.; Windus, T. L. *J. Chem. Phys.* **1998**, *109*, 1223−1229.

(42) Yanagisawa, S.; Tsuneda, T.; Hirao, K. *J. Chem. Phys.* **2000**, *112*, 545−553.

(43) Pou-AméRigo, R.; Merchán, M.; Nebot-Gil, I.; Malmqvist, P.-Å.; Roos, B. O. *J. Chem. Phys.* **1994**, *101*, 4893−4902.

(44) Rose, J. H.; Ferrante, J.; Smith, J. R. *Phys. Rev. Lett.* **1981**, *47*, 675−678.

(45) Birch, F. *Phys. Rev.* **1947**, *71*, 809−824.

(46) Caro, A.; Crowson, D.; Caro, M. *Phys. Rev. Lett.* **2005**, *95*, 075702:1−075702:4.

(47) Gnu octave. http://www.gnu.org/software/octave (accessed Dec 15, 2015).

(48) Kaelo, P.; Ali, M. M. *J. Optim. Theory Appl.* **2006**, *130*, 253−264.

(49) Powell, M. J. D. *The BOBYQA Algorithm for Bound Constrained Optimization without Derivatives*; Tech. Rep.; Department of Applied Mathematics and Theoretical Physics, Cambridge University: 2009. http://www6.cityu.edu.hk/rcms/publications/preprint26.pdf (accessed Dec 15, 2015).

(50) Johnson, S. G. *The nlopt Nonlinear-Optimization Package.* http://ab-initio.mit.edu/nlopt (accessed Dec 15, 2015).

(51) Plimpton, S. *J. Comput. Phys.* **1995**, *117*, 1−19.

(52) http://lammps.sandia.gov/doc/pair_hybrid.html, http://lammps.sandia.gov/doc/pair_zbl.html, http://lammps.sandia.gov/doc/pair_gromacs.html (accessed Dec 15, 2015).

II

Reprinted from A. Tamm, A. Aabloo, M. Klintenberg, M. Stocks, and A. Caro, Atomic-scale properties of Ni-based FCC ternary, and quaternary alloys, Acta Materiala 99, 307-312, 2015. Copyright 2016, with permission from Elsevier.

Acta Materialia 99 (2015) 307–312

Contents lists available at ScienceDirect

Acta Materialia

journal homepage: www.elsevier.com/locate/actamat

Atomic-scale properties of Ni-based FCC ternary, and quaternary alloys

Artur Tamm [a,b,*], Alvo Aabloo [b], Mattias Klintenberg [c], Malcolm Stocks [d], Alfredo Caro [a]

[a] Materials Science and Technology Division, Los Alamos National Laboratory, Los Alamos, NM 87544, USA
[b] IMS Lab, Institute of Technology, University of Tartu, 50411 Tartu, Estonia
[c] Department of Physics and Astronomy, Uppsala University, SE-75120 Uppsala, Sweden
[d] Oak Ridge National Laboratory, Oak Ridge, TN 54321, USA

ARTICLE INFO

Article history:
Received 28 April 2015
Revised 10 August 2015
Accepted 10 August 2015
Available online 26 August 2015

Keywords:
High entropy alloy
Density functional theory
Monte Carlo
Short-range order
Ni based alloys

ABSTRACT

The aim of this study is to characterize some atomic-scale properties of Ni-based FCC multicomponent alloys. For this purpose, we use Monte Carlo method combined with density functional theory calculations to study short-range order (SRO), atomic displacements, electronic density of states, and magnetic moments in equimolar ternary NiCrCo, and quaternary NiCrCoFe alloys. According to our study, the salient features for the ternary alloy are a negative SRO parameter between Ni–Cr and a positive between Cr–Cr pairs as well as a weakly magnetic state. For the quaternary alloy we predict negative SRO parameter for Ni–Cr and Ni–Fe pairs and positive for Cr–Cr and Fe–Fe pairs. Atomic displacements for both ternary and quaternary alloys are negligible. In contrast to the ternary, the quaternary alloy shows a complex magnetic structure. The electronic structure of the ternary and quaternary alloys shows differences near the Fermi energy between a random solid solution and the predicted structure with SRO. Despite that, the calculated EXAFS spectra does not show enough contrast to discriminate between random and ordered structures. The predicted SRO has an impact on point-defect energetics, electron–phonon coupling and thermodynamic functions and thus, SRO should not be neglected when studying properties of these two alloys.

© 2015 Acta Materialia Inc. Published by Elsevier Ltd. All rights reserved.

1. Introduction

In the search of better materials needed in many different industries, such as energy production, scientists have started to explore unconventional concepts of material design. Some examples of these are engineered nanostructures and alloys with many different elements. Instead of consisting of two or three principal elements, as is the case with traditional alloys, high entropy alloys (HEA) [1] have five or more elements in close to equimolar ratios that form simple solid solution phases in FCC, HCP, or BCC structures. Recent studies have shown that HEA's have many improved properties compared to conventional alloys or to the pure elements they are made of [2]. For example, high strength, high ductility, better resistance to wear and corrosion.

The core effects that are considered to affect the microstructure and properties of HEA's are [3]: high entropy, sluggish diffusion, severe lattice distortion, and cocktail effect. The high number of principal elements increases the contribution to the free energy from the configurational entropy term, which stabilizes the random solid solution phase with respect to competing phases. The large fluctuations of the lattice potential between different lattice sites hinder the diffusion of atoms by creating a distribution of activation energies. Also, many low potential lattice sites act as traps and further decrease diffusivity. This has been observed in NiCrCoFeMn HEA [4] where the activation energies were higher than in pure elements and ternary alloys consisting of same elements. Due to differences in atomic sizes and bonding the lattice becomes distorted, increasing hardness and strength and making these properties insensitive to temperature. Lastly, the cocktail effect provides guidelines for manipulating material properties by adding or removing elements, which stabilize BCC or FCC phases, or improve hardness.

When creating ternary and higher element phase diagrams it is often assumed that the solid solution phases are random. This simplifying assumption is due to the lack of experimental data as is the case for NiCrCo ternary [5] or NiCrCoFe quaternary alloys. Experimental phase diagram determinations show that the equimolar NiCrCo alloy is a solid solution in FCC phase [6–8], but no information on the detailed ordering of atoms is available. In fact, short-range order (SRO) has been observed in the binary NiCr alloy at various compositions and temperatures [9–11], which

---

* Corresponding author at: IMS Lab, Institute of Technology, University of Tartu, 50411 Tartu, Estonia.

E-mail address: artur.tamm@ut.ee (A. Tamm).

http://dx.doi.org/10.1016/j.actamat.2015.08.015
1359-6454/© 2015 Acta Materialia Inc. Published by Elsevier Ltd. All rights reserved.

suggests that ordering between Ni–Cr pairs might also occur in the ternary and quaternary alloy. This kind of ordering could lower the configurational entropy from its maximum value, which corresponds to a random alloy, and change the expressions for the free energy and the low-T phase diagram. SRO also decreases the enthalpy of the system, affecting defect energetics.

Computer simulations is a powerful technique to study structure and properties of a material with such an accuracy that for many systems prior experimental knowledge is not needed. It allows screening different structures and studying stability and other properties, without costly experiments. Recently, a hybrid Monte Carlo (MC) and molecular dynamics (MD) method combined with density functional theory calculations (DFT) [12] was used to study refractory HEA [13]. It was shown that the method could be used to study ordering in an alloy at temperatures as low as 300 K.

In this work we explore the short-range order of ternary and quaternary Ni based high entropy alloys using MC combined with *ab initio* energetic calculations. We first use lattice MC to find the equilibrium structure of the alloys, and then we use MD to allow for atomic relaxations. With this information we study formation energy, electronic density of states (DOS), magnetic moments and configurational entropy for both random alloy and the structure with the SRO for which no experimental results are available.

2. Methodology

A rule of thumb in MC calculations suggests that a number as high as 10^4 MC steps per atom have to be attempted in order to approach thermodynamic equilibrium. MC simulations based on *ab initio* energetics cannot reach such a number of steps, implying that the results are not necessarily converged and must be interpreted with caution. Particularly, we observe clear tendencies for the energetics and SRO, but the values we obtain can not be taken as converged values; longer simulations may results in even larger degrees of order and lower formation energies. Along similar arguments, the combination of MC and MD gives thermodynamic equilibrium structures including relaxations; however, and in order to accelerate convergence, we have verified *a posteriori* that relaxations account for a small amount of energy, and have therefore conducted lattice MC followed by MD relaxation only at the end of the MC runs.

The systems studied were equimolar $Ni_{0.33}Cr_{0.33}Co_{0.33}$ ternary, and $Ni_{0.25}Cr_{0.25}Co_{0.25}Fe_{0.25}$ quaternary alloys in the FCC phase. The temperatures investigated were 500, 800 and 1200 K. Energy calculations were conducted using DFT with the VASP software package [14–17]. The supercell used consisted of 108 atoms. The plane wave cut-off energy in all calculations was 269 eV which is the value recommended for Ni by software manual and is the highest recommended cut-off for the elements under consideration. Methfessel–Paxton smearing method of the first order [18] with a smearing width of 0.1 eV was used, and integration in the Brillouin zone was performed with a mesh created using Monkhorst–Pack [19] method with $2 \times 2 \times 2$ points. Core electrons were described with projector augmented-wave pseudopotentials [20,21] provided by VASP package. The number of valence electrons were 10, 6, 9, and 8 for Ni, Cr, Co, and Fe respectively. Generalized gradient approximation as described by Perdew–Burke–Ernzerhof (PBE) [22] was used for describing exchange–correlation of electrons. All calculations done were spin-polarized.

Additionally, the calculations to investigate formation energy, structure relaxations, and DOS were conducted with higher number of *k*-points ($3 \times 3 \times 3$) to increase the accuracy. Convergence studies were made to determine the best calculation parameters needed for accurate results. The energies obtained from the selected parameters have an average error of about 0.2 meV per atom. The X-ray absorption fine structure spectrum for the NiCrCoFe HEA was calculated using *ab initio* real space multiple scattering calculations as described in [23–25].

Lattice MC simulations included swap of atomic type trials with the acceptance probability based on the Metropolis - Hastings sampling [26]. In some cases, ionic relaxations at intermediate steps during the simulation were done to assess the change in energy from relaxation. As the atoms are of similar size the resulting changes were of the order of 5 meV per atom, a value that we consider small compared to the gain obtained from chemical ordering, which typically is ten times larger. A special quasi-radom structure (SQS) [27] was selected as an initial starting point in all calculations.

The Warren-Cowley SRO parameter [28] was used to quantify the chemical ordering around an atomic species. The SRO α_{ij}^{v} was calculated using Eq. (1), where p_{ij}^{v} is the probability of finding atomic species j around an atom of type i in the v's neighboring shell and c_j is the atomic concentration of type j. The SRO $\alpha = 0.0$ corresponds to a random solution. Positive values show a tendency to decrease the number of i,j pairs, while negative values correspond to the opposite.

$$\alpha_{ij}^{v} = 1 - \frac{p_{ij}^{v}}{c_j}. \tag{1}$$

The SQS structures were created by swapping element species randomly in an initial randomly generated sample until a SRO as close as possible to that of a random alloy up to the third nearest neighbor would be found. In this approach a cost function defined as the sum of SRO squares was minimized to find a structure that would be as close as possible to an ideal random solution for this small sample size.

The configuration entropy of a system with non-zero SRO can be estimated using the cluster variation method (CVM) in the pair approximation [29] using the following equation:

$$S = k_B\left((z-1)\sum_i (c_i \ln c_i - c_i) - z/2\sum_{ij}(y_{ij}\ln y_{ij} - y_{ij}) + (z/2-1)\right), \tag{2}$$

where z is the number of nearest-neighbors, c_i is the concentration of type i and y_{ij} is the probability of finding an i,j pair.

Formation energies were calculated using Eq. (3), where E_{tot} is the total energy per atom of the mixed system, c_i is the concentration of element i and $E_{i,ref}$ is the energy per atom of the reference phase of element i. Summation goes over all the elements in the alloy. The reference energies were calculated in the ground state phases of Ni, Cr, Co, and Fe, which are FCC, BCC, HCP, and BCC respectively, including magnetism. The lattice constants used for the pure element reference energies are obtained from the equation of state minima predicted by DFT. The calculated magnetic moments of pure element ground states agree well with similar calculations from the literature.

$$\Delta E_f = E_{tot} - \sum_i^N c_i E_{i,ref}. \tag{3}$$

3. Results and discussion

3.1. Ternary NiCrCo

Lattice MC simulations for the NiCrCo equimolar alloy at three temperatures 500 K, 800 K, and 1200 K were performed. The simulations started from a SQS structure using the 3.56 Å experimental lattice parameter [30]. The simulation at 500 K lasted for 1500 steps, which represents 14 swap trials per atom. Higher temperatures were run for 1000 MC steps. The resulting final structure with SRO at 500 K and initial SQS structure were later relaxed keeping the volume constant at 0 K and analyzed.

At 500 K the most significant trends in the development of SRO's as well as potential energy are shown in Fig. 1. Although, the number of swap trials per atom is relatively small compared to classical MC simulations the potential energy curve seems to be relatively converged. Our finding is that major deviations from a random solid solution appear for the Ni–Cr and Cr–Cr pairs. The average number of Cr–Cr neighbors is reduced by ~40%, from 4 for the random case to about 2.3, and the number of Ni–Cr pairs is increased to 5. Additionally, the number of Ni–Ni pairs is decreased and Cr–Co pairs increased slightly. All the other pairs are close to the values of the random solution. With increasing temperature the SRO parameters approach the value of random solid solutions, with the exception of Cr–Cr pairs, which still remains significantly high, but somewhat lower than for the 500 K case. The final averaged SRO parameter values are shown in Table 1.

Table 1
Short-range order parameter of the NiCrCo ternary FCC system averaged over last steps of the lattice MC simulation at three temperatures.

Pair	500 K	800 K	1200 K
Ni–Ni	0.12	0.03	0.07
Ni–Cr	−0.27	−0.15	−0.12
Ni–Co	0.15	0.13	0.05
Cr–Cr	0.42	0.28	0.14
Cr–Co	−0.16	−0.12	−0.03
Co–Co	0.01	0.00	−0.03

The appearance of the SRO reduces the free energy mainly by lowering the formation energy, which changes from 93 to 47 meV per atom. Furthermore, atomic relaxation reduces the energy by no more than 5 meV per atom. Positive formation energy implies a tendency to phase separation at low temperature, but for this small sample size MC is not an adequate technique to explore this phase boundary. The experimental phase diagram at 800 °C for the ternary NiCrCo alloy suggests that at the equimolar ratio the system forms an FCC solid solution [5]. We note that the presence of SRO may influence the location of phase boundaries, because of the lower formation energy and configurational entropy.

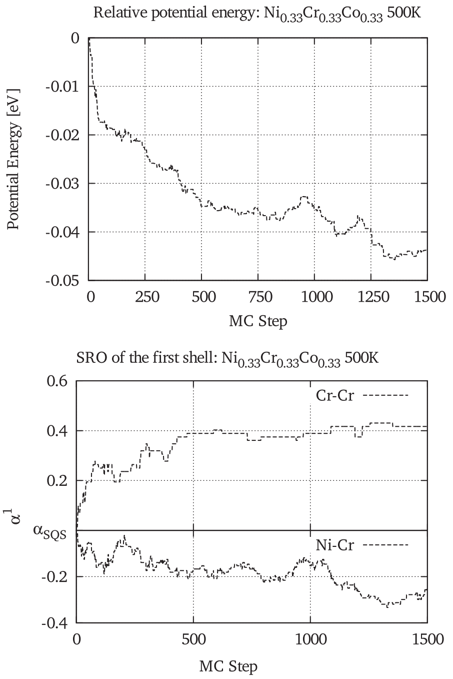

Fig. 1. Evolution of potential energy and SRO in the lattice MC simulation of NiCrCo ternary alloy at 500 K. Plotted is the relative potential energy (top) and SRO parameter in the first neihgbor shell for Cr–Cr and Ni–Cr (bottom) pairs.

The large positive value of SRO for Cr–Cr pairs might be related to a similar effect observed in Fe–Cr BCC alloy [31]. The change in SRO in that system is related to a strong Cr–Cr repulsion when at nearest neighbor positions originated in the magnetic frustration resulting from Cr atoms forced to align ferromagnetically.

The atomic displacements with respect to perfect lattice positions are found to be in the range of 0.04 Å which are comparable to the magnitude associated to thermal fluctuations and thus are negligible for both the SQS and SRO structures. The largest displacements were mostly related to Cr atoms. This justifies the use of lattice MC for the ternary system.

The DOS, for the random alloy and the predicted SRO structure are shown in Fig. 2. DOS is not significantly affected by SRO, the largest difference being near the Fermi energy, which has implications for both electric and thermal transport properties, and on the electron–phonon interaction.

The system with SRO has a lower mean magnetic moment than in the case of SQS, as shown in Table 2. The mean magnetic moments of both Ni and Co are lower and mean magnetic moment of Cr is higher compared to SQS. In the analysis of individual magnetic moments, which are shown in Fig. 3, it can be seen that the main change occurs in the amplitude of the magnetic moments of Cr atoms. In the case of SQS, the values are closer to a random distribution than in the case of the structure with SRO. Also, magnetic moments of Cr atoms are not in the same direction, whereas the moments of Ni and Co are mostly pointing in the same directions.

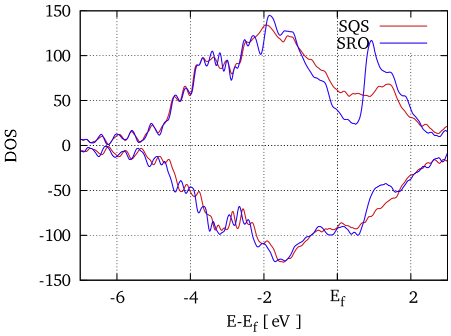

Fig. 2. Electronic density of states for the initial quasi-random structure (SQS) and the structure predicted by lattice MC simulation (SRO) of NiCrCo ternary system relaxed at 0 K.

Table 2
Properties of NiCrCo ternary and NiCrCoFe quaternary systems for the special quasirandom structure (SQS) and structure with ordering (SRO) as predicted by lattice MC simulations at 500 K. The values are obtained for 0 K relaxed structures at constant volume.

System	Ordering	$E_f \left[\frac{meV}{atom}\right]$	$S_{conf} \left[\frac{k_B}{atom}\right]$	Δr_{rms} [Å]	$\langle\mu\rangle$ $[\mu_B]$	$\langle\mu_{Ni}\rangle$ $[\mu_B]$	$\langle\mu_{Cr}\rangle$ $[\mu_B]$	$\langle\mu_{Co}\rangle$ $[\mu_B]$	$\langle\mu_{Fe}\rangle$ $[\mu_B]$
NiCrCo	SQS	93.0	1.099	0.044	0.332	0.193	−0.229	1.031	
	SRO	47.3	0.944	0.035	0.080	0.098	−0.857	0.999	
NiCrCoFe	SQS	76.7	1.386	0.057	0.668	0.319	−0.903	1.173	2.083
	SRO	15.8	1.097	0.031	0.537	0.296	−1.461	0.983	2.330

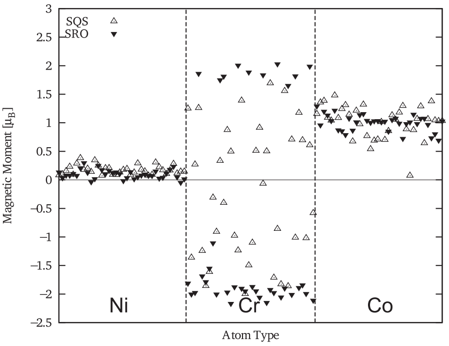

Fig. 3. Magnetic moments of individual atoms in quasi-random structure (SQS) and structure with short-range order (SRO) as predicted by lattice MC at 500 K for the equimolar NiCrCo alloy.

Finally, we find that the configurational entropy of the alloy with SRO is about 10% lower than the value of a random solid solution, as reported in Table 2.

3.2. Quaternary NiCrCoFe

Similar lattice MC simulations were done with the quaternary NiCrCoFe alloy. The simulations started from SQS structure with an experimental lattice parameter of 3.57 Å [30] and the 500 K case ran for 2000 steps resulting in 18 swap trials per atom. The higher temperature runs lasted for 1500 steps. The final SRO parameters at three temperatures are provided in Table 3. Also, the evolution of potential energy and major trends in the evolution of SRO are plotted in Fig. 4. Here again the evolution of potential energy suggests that the simulation has been long enough to show a clear trend. The final structure from the 500 K simulations was relaxed at 0 K without changing the volume and analyzed.

Table 3
Short-range order parameter of the NiCrCoFe quaternary FCC system averaged over last steps of the lattice MC simulation at three temperatures.

Pair	500 K	800 K	1200 K
Ni–Ni	0.30	0.16	0.13
Ni–Cr	−0.18	−0.21	−0.22
Ni–Co	0.14	0.10	0.12
Ni–Fe	−0.27	−0.04	−0.04
Cr–Cr	0.59	0.54	0.65
Cr–Co	−0.31	−0.18	−0.26
Cr–Fe	−0.10	−0.14	−0.17
Co–Co	0.33	0.13	0.11
Co–Fe	−0.16	−0.05	0.03
Fe–Fe	0.54	0.23	0.17

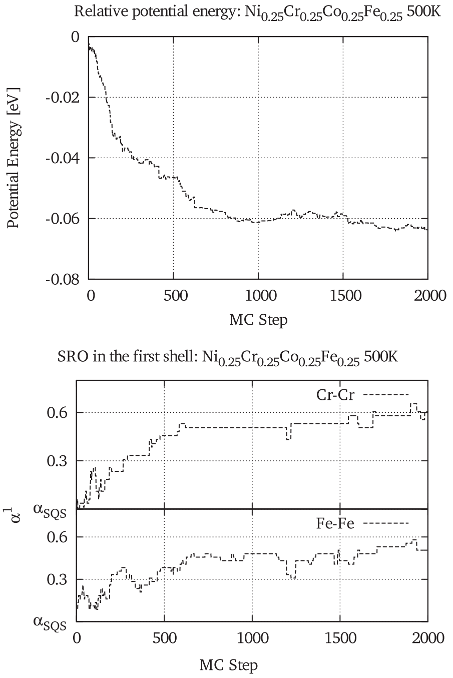

Fig. 4. Development of potential energy and SRO in the lattice MC simulation of NiCrCoFe quaternary alloy at 500 K. Plotted is the relative potential energy (top) and SRO parameter in the first neihgbor shell for Cr–Cr and Fe–Fe pairs (bottom).

Similar trends as in the case of ternary alloy are clearly present. The number of Cr–Cr pairs is reduced by ~50%, and the number of Ni–Cr is increased, when compared to a random alloy. Additionally, the number of Fe–Fe pairs is significantly reduced and number of Ni–Fe, Cr–Co, and Co–Fe pairs is increased. Also, there is quite a large reduction of Ni–Ni and Co–Co pairs, where the number of same type neighbors is reduced to 2 atoms instead of 3. Similarly to the case of the ternary alloy, the increase in temperature reduces the SRO values of all pairs, while the value for the Cr–Cr pairs is still significantly large.

The deviation of SRO for Cr–Cr pairs is even larger for the quaternary case than for the ternary. Investigation of SRO for second and third shells in the 1200 K case revealed that most of the Cr atoms are at the second nearest neighbor locations, implying the formation of an ordered structure with simple cubic Cr sublattice.

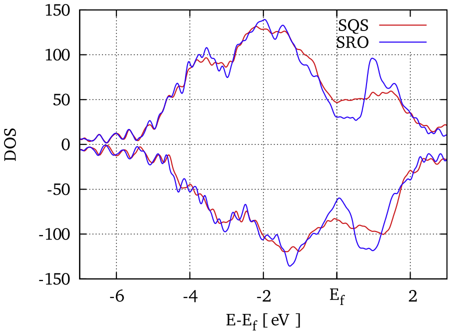

Fig. 5. Electronic density of states for the initial quasi-random structure (SQS) and the structure predicted by lattice MC simulation (SRO) of NiCrCoFe quaternary system relaxed at 0 K.

As for the ternary alloy, the magnetic frustration of Cr atoms leads to structure where every Cr atom is surrounded by ferromagnetic elements. The inclusion of Fe into alloy enhances this kind of driving force even more.

As in the case of ternary alloy, the development of SRO involves a lowering of formation energy by about 60 meV per atom, from 76 to 16. Atomic relaxation changes the energy from its initial value about 5 meV per atom. Although there is a large reduction of formation energy, it still remains positive and thus phase separation should occur at low temperatures.

Furthermore, the DOS at the Fermi level differs significantly from the random alloy, as seen in Fig. 5. The lower density of states near the Fermi energy would decrease the electron–phonon coupling as it is proportional to DOS.

The magnetic moments of the structure with SRO have a much smaller spread and, as in the ternary alloy, those of Cr atoms are mostly antiferromagnetically aligned with respect to all other elements (see Fig. 6). SRO also increases the absolute value of mean magnetic moments.

Similarly with the ternary alloy, SRO results in a sizable change of the configurational entropy in relation to the random solution, of about 26% as calculated from the CVM model. This would significantly change the locations of phase boundaries.

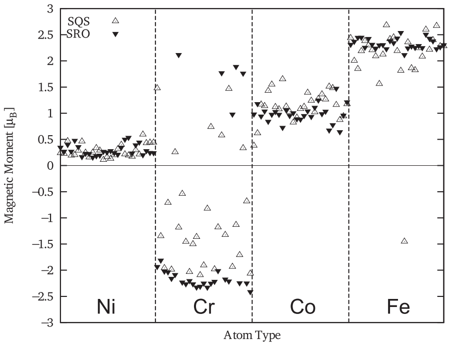

Fig. 6. Magnetic moments of individual atoms in quasi-random structure (SQS) and structure with short-range order (SRO) as predicted by lattice MC at 500 K for the equimolar NiCrCoFe alloy.

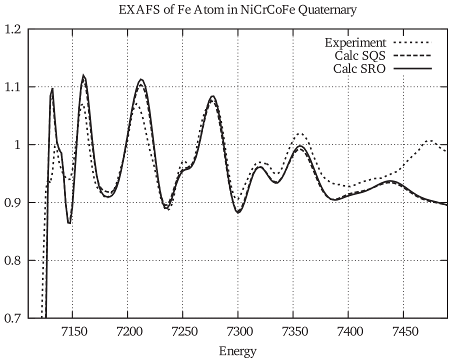

Fig. 7. Calculated EXAFS of quasi-random (SQS) and structure predicted by lattice MC simulation (SRO) for the equimolar NiCrCoFe alloy in comparison with experimental data.

Next, during the atomic relaxation at 0 K the atoms move only slightly and the mean atomic displacement is around 0.06 Å. As with the ternary alloy the largest displacements are for Cr atoms.

Finally, the EXAFS spectra was calculated for the quaternary case for both SQS and SRO structures. The results are shown in Fig. 7. These results agree quite well with experimental results, but there is no significant difference between the SQS and SRO spectra, which suggests that X-ray methods do not show enough contrast between these elements to detect the changes in SRO that we predict from lattice MC simulations.

4. Conclusions

In summary, lattice MC simulations were conducted to study SRO in Ni based ternary and quaternary alloys, as a preliminary study aiming at Ni-based HEA's. Our main conclusion is that, contrary to the common assumption that HEA's are random solid solutions, equimolar NiCrCo HEA alloy shows a significant degree of short range order involving a ~40% decrease in the number of Cr–Cr pairs together with an increase in Ni–Cr and Cr–Co pairs with respect to random distributions. For the NiCrCoFe quaternary alloy a similar behavior was found, namely an even larger decrease in the number of Cr–Cr and Fe–Fe pairs and a moderate increase in Ni–Cr, Ni–Fe, Cr–Co, and Co–Fe pairs as well as a decrease of Ni–Ni and Co–Co pairs. We also show that this SRO affects properties such as alloy formation energy, atomic mean square displacements, electronic density of states, and configurational entropy. Ordering lowers the formation energy in several tenths of meV per atom and reduces the configurational entropy by ~20%, enough to change the values of the free energy of the solution phase affecting the location of phase boundaries by significant amounts. Additionally, SRO defines the energy landscape for defects in both their formation and migration energies. Lastly, the change in DOS near the Fermi energy due to SRO influences transport properties and the electro-phonon coupling.

Acknowledgements

This work was supported by the Energy Deposition to Defect Evolution (EDDE), an Energy Frontier Research Center funded by the U.S. Department of Energy, Office of Science, Basic Energy

Sciences (Award Number 2014 ORNL 1026) at Oak Ridge and Los Alamos National Laboratories. AT was partially funded by the European Social Fund's Doctoral Studies and Internationalization Programme DoRa, which is carried out by Foundation Archimedes and Estonian Research Council grant IUT20-24.

References

[1] J.W. Yeh, Y.L. Chen, S.J. Lin, S.K. Chen, High-entropy alloys – a new era of exploitation, Mater. Sci. Forum 560 (2007) 1–9, http://dx.doi.org/10.4028/www.scientific.net/MSF.560.1.
[2] Y. Zhang, T.T. Zuo, Z. Tang, M.C. Gao, K.A. Dahmen, P.K. Liaw, Z.P. Lu, Microstructures and properties of high-entropy alloys, Prog. Mater. Sci. 61 (2014) 1–93, http://dx.doi.org/10.1016/j.pmatsci.2013.10.001.
[3] J.-W. Yeh, Alloy design strategies and future trends in high-entropy alloys, JOM 65 (12) (2013) 1759–1771, http://dx.doi.org/10.1007/s11837-013-0761-6.
[4] K.-Y. Tsai, M.-H. Tsai, J.-W. Yeh, Sluggish diffusion in Co–Cr–Fe–Mn–Ni high-entropy alloys, Acta Mater. 61 (13) (2013) 4887–4897, http://dx.doi.org/10.1016/j.actamat.2013.04.058.
[5] S. Yang, M. Jiang, H. Li, Y. Liu, L. Wang, Assessment of Co–Cr–Ni ternary system by CALPHAD technique, Rare Metals 31 (1) (2012) 75–80, http://dx.doi.org/10.1007/s12598-012-0466-y.
[6] S. Rideout, W.D. Manly, E.L. Kamen, B.S. Lement, P.A. Beck, Intermediate phases in ternary alloy systems of transition elements, Trans. AIME 191 (1951) 872–876.
[7] G.P. Zhmurko, E.G. Kabanova, V.N. Kuznetsov, A.V. Leonov, Phase equilibria in the Co–Cr–Ni system, Moscow Univ. Chem. Bull. 63 (4) (2008) 234–235, http://dx.doi.org/10.3103/S0027131408040135.
[8] T. Omori, J. Sato, K. Shinagawa, I. Ohnuma, K. Oikawa, R. Kainuma, K. Ishida, Experimental determination of phase equilibria in the Co–Cr–Ni system, J. Phase Equilib. Diffus. 35 (2) (2014) 178–185, http://dx.doi.org/10.1007/s11669-014-0292-z.
[9] W. Schweika, H. Haubold, Neutron-scattering and Monte Carlo study of short-range order and atomic interaction in Ni 0.89 Cr 0.11, Phys. Rev. B 37 (16) (1988) 9240–9248.
[10] B. Schönfeld, L. Reinhard, Short-range order and atomic displacements in Ni-20 at% Cr single crystals, Phys. Status Solidi 148 (1988) 457–471.
[11] R. Caudron, M. Sarfati, In situ diffuse scattering of neutrons in alloys and application to phase diagram determination, J. Phys, I Fr. 2.
[12] W. Kohn, L.J. Sham, Self-consistent equations including exchange and correlation effects, Phys. Rev. 140 (1965) A1133, http://dx.doi.org/10.1103/PhysRev. 140.A1133.
[13] M. Widom, W.P. Huhn, S. Maiti, W. Steurer, Hybrid Monte Carlo/molecular dynamics simulation of a refractory metal high entropy alloy, Metall. Mater. Trans. A 45 (1) (2013) 196–200, http://dx.doi.org/10.1007/s11661-013-2000-8.
[14] G. Kresse, J. Hafner, Ab initio molecular dynamics for liquid metals, Phys. Rev. B 47 (1) (1993).
[15] G. Kresse, J. Hafner, Ab initio molecular-dynamics simulation of the liquid–metal-amorphous-semiconductor transition in germanium, Phys. Rev. B 49 (1994) 14251.
[16] G. Kresse, J. Furthmuller, Efficiency of ab-initio total energy calculations for metals and semiconductors using a plane-wave basis set, Comput. Mater. Sci. 6 (1996) 15.
[17] G. Kresse, J. Furthmüller, Efficient iterative schemes for ab initio total-energy calculations using a plane-wave basis set, Phys. Rev. B. Condens. Matter 54 (16) (1996) 11169–11186.
[18] M. Methfessel, A.T. Paxton, High-precision sampling for Brillouin-zone integration in metals, Phys. Rev. B 40 (6) (1989) 3616–3621.
[19] H. Monkhorst, J. Pack, Special points for Brillouin-zone integrations, Phys. Rev. B 13 (1976) 5188–5192.
[20] P.E. Blöchl, Projector augmented-wave method, Phys. Rev. B 50 (1994) 17953, http://dx.doi.org/10.1103/PhysRevB.50.17953.
[21] G. Kresse, D. Joubert, From ultrasoft pseudopotentials to the projector augmented-wave method, Phys. Rev. B 59 (1999) 1758.
[22] J.P.J. Perdew, K. Burke, M. Ernzerhof, Generalized gradient approximation made simple, Phys. Rev. Lett. 77 (18) (1996) 3865.
[23] A.L. Ankudinov, B. Ravel, J.J. Rehr, S.D. Conradson, Real-space multiple-scattering calculation and interpretation of x-ray-absorption near-edge structure, Phys. Rev. B 58 (1998) 7565–7576.
[24] J.J. Rehr, R.C. Albers, Theoretical approaches to X-ray absorption fine structure, Rev. Mod. Phys. 72 (2000) 621.
[25] J.J. Rehr, J.J. Kas, M.P. Prange, A.P. Sorini, Y. Takimoto, F.D. Vila, Ab initio theory and calculations of X-ray spectra, C. R. Phys. 10 (6) (2009) 548–559.
[26] W.K. Hasting, Monte Carlo sampling methods using Markov chains and their applications, Biometrica 57 (1970) 97.
[27] A. Zunger, S.H. Wei, L.G. Ferreira, J.E. Bernard, Special quasirandom structures, Phys. Rev. Lett. 65 (3) (1990) 353–356.
[28] J.M. Cowley, An approximate theory of order in alloys, Phys. Rev. 77 (5) (1950) 669–675, http://dx.doi.org/10.1103/PhysRev. 138.A1384.
[29] R. Kikuchi, CVM entropy algebra, Prog. Theor. Phys. Suppl. 115 (1994) 1–26.
[30] M. Stocks, private communication.
[31] A. Caro, M. Caro, P. Klaver, B. Sadigh, The computational modeling of alloys at the atomic scale: from ab initio and thermodynamics to radiation-induced heterogeneous precipitation, J. Miner. Metal Mater. Soc. 59 (April) (2007) 52, http://dx.doi.org/10.1007/s11837-007-0055-y.

III

Reprinted with permission from A. Caro, A. A. Correa, A. Tamm, G. Samolyuk, and M. Stocks, Adequacy of damped dynamics to represent the electron-phonon interaction in solids, Physical Review B, 92, 144309, 2015.
Copyright 2016 by the American Physical Society.

PHYSICAL REVIEW B **92**, 144309 (2015)

Adequacy of damped dynamics to represent the electron-phonon interaction in solids

A. Caro,[1,*] A. A. Correa,[2] A. Tamm,[1] G. D. Samolyuk,[3] and G. M. Stocks[3]
[1]*Materials Science and Technology Division, Los Alamos National Laboratory, Los Alamos, New Mexico 87545, USA*
[2]*Quantum Simulations Group, Lawrence Livermore National Laboratory, Livermore, California 94550, USA*
[3]*Materials Science and Technology Division, Oak Ridge National Laboratory, Oak Ridge, Tennessee 54321, USA*

(Received 3 June 2015; revised manuscript received 1 September 2015; published 16 October 2015)

Time-dependent density functional theory and Ehrenfest dynamics are used to calculate the electronic excitations produced by a moving Ni ion in a Ni crystal in the case of energetic MeV range (electronic stopping power regime), as well as thermal energy meV range (electron-phonon interaction regime). Results at high energy compare well to experimental databases of stopping power, and at low energy the electron-phonon interaction strength determined in this way is very similar to the linear response calculation and experimental measurements. This approach to electron-phonon interaction as an electronic stopping process provides the basis for a unified framework to perform classical molecular dynamics of ion-solid interaction with *ab initio* type nonadiabatic terms in a wide range of energies.

DOI: 10.1103/PhysRevB.92.144309 PACS number(s): 79.20.Rf, 79.20.Ap, 81.40.Wx, 83.10.Mj

I. INTRODUCTION

The Born-Oppenheimer approximation (BOA) [1] is the keystone to describe ionic motion in condensed matter. This approximation, in which ions move classically under the forces derived from the electronic ground-state energy, proved to be useful to describe nuclear stopping power for low-energy ions in solids, S_n. However, for ion energies approaching the Fermi velocity of electrons in the target, electronic loses, or nonadiabatic effects, become increasingly relevant. The rate of energy transfer to electrons can be cast in the form of an electronic stopping power S_e that, together with S_n, are the two mechanisms of energy dissipation for energetic ions colliding with a target material. As part of the BOA, S_n and S_e are customarily assumed to be independent of each other; however, in the presence of nonadiabatic energy exchanges, actual materials' response is beyond the BOA.

For projectile velocities below the target Fermi velocity, S_n and S_e are both relevant, creating a complex nonequilibrium situation that can be studied with a diversity of theoretical approaches. To a large extent, computational studies of radiation damage have ignored the dynamic response of the electrons to such perturbation; the majority has been done within the BOA, or with classical potentials, ignoring electron dynamics. From the early days, authors noticed the necessity to go beyond this approximation, ranging from collision cascades [2–11] and rapid shocks [12] to current-induced forces [13].

In addition to the phenomena related to stopping power (S_n and S_e), the electron-phonon (e-ph) interaction is also important, since it is responsible for the return to thermal equilibrium between the nuclear and electronic subsystems. In this work the expression electron-phonon interaction refers to both, the interaction of electrons with well-defined collective ionic motion excitations characterized by wave and polarization vectors, and the local picture of ions moving individually. Hybrid models combine different aspects of the problem in an *ad hoc* manner; these include two-temperature models (TTM) [2,3], phenomenological stopping based in the local density [4], collective excitations in a Coulomb explosion [5–8], and thermal spike approaches [2,3,9,10]. In general, these approaches consider a classical "electronic thermal" field evolving via heat transport equations, and coupled to ions via Langevin dynamics [11].

In the state-of-the-art implementations of classical molecular dynamics (MD) with two temperatures, such as Duffy's [11,14–16], a viscous damping term (βv) and a random force (ξ) are added to the Newton equations of motion of each ion: $F = -\beta v + \xi(t)$, where β is a piecewise function known in two limits: (i) $\beta = \beta_{S_\mathrm{e}} + \beta_\text{e-ph}$ for $v_0 < v < v_\mathrm{F}$ and (ii) $\beta = \beta_\text{e-ph}$ for $v < v_0$ [17], where v_0 is a threshold velocity related to a cutoff kinetic energy chosen arbitrarily in the range of ~10–100 eV. The parameters β_{S_e} and $\beta_\text{e-ph}$ have different values, since they are considered as being originated in different physical processes. For example, the authors of Ref. [18] assume "that the e–ph coupling process is not initiated until 0.3 ps after the initiation of the collision process, as the lattice temperature is ill-defined before this. Until this time of the simulation only the electron stopping mechanism is active, while there is a time-frame when both the electronic stopping and e–ph interaction mechanisms are active."

As examples of this way of approaching the problem, we mention the works of Sand *et al.* on damage of W [19] using $\tau_{S_\mathrm{e}} = m/\beta_{S_\mathrm{e}} = 1$ ps for the electronic stopping (with m the mass of the ions) and no e-ph term; of Zarkadoula *et al.* on Fe [18], who used a value of $\tau_{S_\mathrm{e}} = 1$ ps for stopping power and $\tau_{S_\text{e-ph}} = 1.54$ ps for the e-ph regime; and of Zhurkin and Kolesnikov in a study of cluster impacts on metals [20], who used $\tau_\text{e-ph} = 1$ ps for Ni and $\tau_\text{e-ph} = 1.7$ ps for Al. Caro and Victoria and Proennecke *et al.* considered $3.4 < \tau_\text{e-ph} < 10$ ps and $0.27 < \tau_{S_\mathrm{e}} < 2.5$ ps for Cu [4,21]. It can be concluded that in the literature there is a diversity of values but always $\tau_{S_\mathrm{e}} > \tau_\text{e-ph}$ by a factor between ~1.5 and ~10.

The aim of this work is to show that the electronic stopping power has a complex dependence on both the ion velocity and the local electronic density, which are both related to the local electronic density of states (LDOS). For a projectile to lose energy to target electrons two conditions are required, first that target electrons have to be where the projectile is and second that there have to filled states where electrons can be taken from

---

[*] caro@lanl.gov

©2015 American Physical Society

and empty states they can fill in; both conditions are related to the structure of the LDOS. The projectile velocity provides an energy scale around the Fermi energy, similar to thermal energy $k_B T$, which determines what electrons participate in the nonadiabatic process. It is known that for the uniform electron gas the stopping power is linear in velocity for projectile velocities less than the Fermi velocity, $S_e = \beta v$, and that β has a complex density dependence [22,23], but for more realistic density of states the situation changes, as has recently been shown for the case of protons and He in Au [24].

Besides the velocity dependence, the reason that makes β_{S_e} and $\beta_{\text{e-ph}}$ different is the local electronic density (ρ) of the target, which an energetic particle can explore in different energy domains: a particle undergoing electronic stopping is an energetic particle that visits many regions in a solid, with different electronic density, while a particle moving in a phononlike mode, i.e., with meV of energy, visits regions close to their equilibrium lattice positions, where the electronic density of the host matrix has a minimum. By making explicit the β dependence on ρ we describe here the e-ph interaction as a special case of electronic stopping process at very low energies. By comparing the strength of the so determined e-ph coupling to fully quantum-mechanical treatments, we assess the validity of the Langevin equation to represent this nonadiabatic phenomenon. The main approximation we make is the assumption of classical motion for the ions at thermal energies, which is presumably valid for kinetic energies above the Debye temperature.

It is important to mention that this local-density dependence of the damping term representing the electronic stopping power was proposed by us years ago [4], but the high degree of empiricism in the functional form proposed for this dependence prevented it from being adopted as a standard approximation. Here we give the initial steps towards a functional form with *ab initio* type accuracy.

Additionally, within the framework of time-dependent tight-binding theory, Race *et al.* [17] reported results providing evidence that, for tight-binding molecular-dynamics simulations, the strength of the coupling depends on the electronic density at the crystalline location of the moving ion, giving support to this work in that the stopping mechanisms appearing in time-dependent electronic structure calculations could account for both S_e and e-ph interaction.

II. METHOD: NONADIABATIC CALCULATION

Using time-dependent density functional theory (TD-DFT) [25] to follow the energy transfer from (classical) ions to (quantum) electrons we analyze the ability of the proposed technique to calculate both the electronic stopping of an energetic projectile traveling along a channeling direction and the the e-ph interaction parameter for the case of a single representative vibrational mode, the Einstein oscillator. Both types of simulations were performed on a supercell with 108 Ni atoms (Γ-only sampling) on a fcc lattice with a lattice parameter of 3.52 Å. Norm-conserving pseudopotentials and an energy cutoff of 150 Ry for a plane-wave basis were used. The calculations included semicore states, were nonmagnetic, and used the adiabatic LDA exchange-correlation (XC) potential. For details on the implementation of TD-DFT in QBOX, see Ref. [26].

Previous work by Pruneda *et al.* and by others on nonadiabatic dynamics in insulators [27], and of Correa and coworkers on H in Al [28,29], proved that TD-DFT gives accurate results for S_e at high (i.e., $E \gg 1$ eV) energies. By accurate we mean in good agreement with the SRIM database, considered to be the standard reference for this property [30,31]. For one particular case studied in this work, namely, a Ni projectile into a Ni target at an energy of 1.5 MeV, SRIM reports a stopping of 148.2 eV/Å while our calculations for the center of a $\langle 100 \rangle$ channel give 42.5 eV/Å. This discrepancy can easily be removed by taking into consideration that experimental values represent averages of actual trajectories and, as discussed in Refs. [29,32], either running off-center channel simulations or random direction trajectories, bring the results into excellent agreement with SRIM.

In this work, we evaluate the electronic stopping for an atom in two different environments: (i) an energetic projectile in channeling conditions and (ii) an atom vibrating with thermal energies around its equilibrium position. We determine a scalar β for both cases, and relate it to the local density seen by the moving atom, which we assume is the main characteristic that distinguishes between the two environments. To this end we first evaluated the time evolution of the total electronic energy of a system composed of a Ni projectile traveling along the center of a $\langle 100 \rangle$ channel in the Ni fcc crystal. Details of these calculations will be published elsewhere; here we show in Fig. 1 the general aspect of these curves.

For the case of an atom vibrating with thermal energies around its equilibrium position, we aim at calculating the stopping power at much lower velocities, corresponding to energies in the meV region. We then face the time-scale limitations imposed by the computational cost of TD-DFT. We adopt then the following strategy: to determine if the sample size (number of electrons in the supercell calculations) is large enough in the sense that the small gaps appearing between the electronic eigenvalues are not affecting the results of the calculation, we propagate the projectile in a uniform electron gas, jellium, with the same parameters used to represent Ni in the DFT calculations, meaning the same XC functional, cutoff,

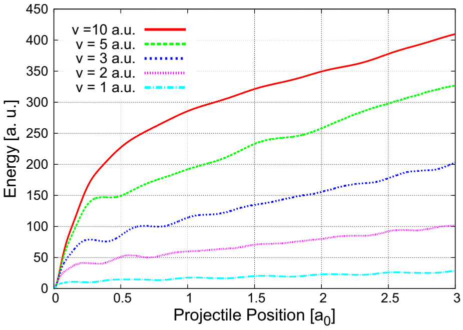

FIG. 1. (Color online) Total energy vs position of the Ni projectile across the $\langle 100 \rangle$ channel in a fcc Ni at different velocities (from 1.5 to 150 MeV). We obtained the electronic stopping power from the slope of these curves, after an initial transient.

box size, etc. The ground state of a jellium with electron density in the range we want to study (0–1.5 $e/\text{Å}^3$) is constructed with a single additional Ni atom. In the time-dependent simulation the Ni ion is then moved at constant velocity. The energy-versus-time curves show a behavior similar to that of the crystalline target, including the transient and excitation of charge oscillations that it originates, but without the periodic oscillations due to the crystalline structure [29].

Comparing the losses corresponding to Ni traveling into crystalline Ni at the center of the $\langle 100\rangle$ channel with those of Ni traveling in jellium we conclude that, on average, Ni travels in the fcc Ni channel producing the same dissipation as if in a homogeneous medium of electronic density $\rho = 0.75\ e/\text{Å}^3$. For a velocity of 1 a.u. (1.5 MeV for Ni) the dissipation in the channel is 45 eV/Å, and β (in $S_e = \beta v$) is 2.06×10^{-3} eV ps/Å^2. This friction can be expressed in time units, as $\tau = m/\beta$, which measures the characteristic relaxation time for excess energy in the ionic system decaying into the electronic system; the relaxation time is 3.5 ps.

We use then jellium to explore the low-velocity regime because it lacks crystalline structure, which implies the need of much shorter trajectories to extract the slope representing the losses, and we can therefore determine the stopping for velocities over several orders of magnitude. Figure 2 shows S_e for a Ni projectile in jellium at a density $\rho = 1.5\ e/\text{Å}^3$ over four orders of magnitude of velocity, or equivalently eight orders of magnitude in energy, from 1.5 MeV (in the electronic stopping power regime) down to 15 meV (in the thermal phonon energy regime). The known linear dependence on the velocity is clearly confirmed (in the range of densities of interest), implying $S_e = \beta(\rho)v$. While the result shown in Fig. 2, namely, that S_e is proportional to velocity for $v < v_F$ in a uniform electron gas, is known, this figure validates the computational approach regarding sample size and emphasizes the fact that the concept of electronic stopping is valid even at thermal energies. It justifies the use of high-velocity results to study low-velocity dissipation, provided a proper treatment of the DOS at E_F for real materials is given. Going to even lower velocities in jellium should still give a linear relation, down to some limit where the discrete structure of the density of states due to the finite sample size would introduce departures from linearity, similar to those reported for insulators [27].

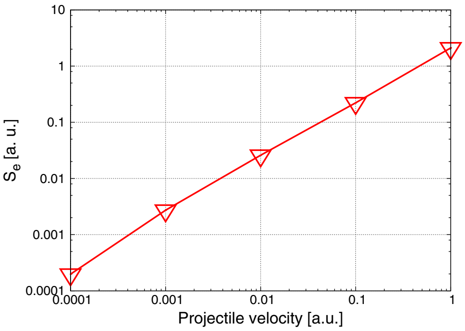

FIG. 2. (Color online) Electronic stopping S_e corresponding to Ni in jellium at metallic electron densities ($\rho = 1.5\ e/\text{Å}^3$) for different velocities covering eight orders of magnitude in kinetic energy, from 1.5 MeV (in the electronic stopping power regime) to 15 meV (corresponding to typical thermal phonon energies). The slope 1 indicates a stopping linearly proportional to velocity.

While jellium gives a stopping proportional to velocity, it is only an approximation to real materials and in particular to Ni, in the sense that it neglects the detailed structure of the electronic density of states (DOS) close to the Fermi energy (E_F), which translates into a velocity dependence to the coupling. We come back to this point at the Discussion section.

III. RESULTS: CONNECTION BETWEEN ELECTRONIC STOPPING POWER AND ELECTRON-PHONON COUPLING

To analyze next the connection between an energetic ion traveling along a channel and an Einstein oscillator, we study the electronic density at different locations in a Ni crystal. Figure 3 shows $\rho(x)$ along two trajectories, one along the center of a $\langle 100\rangle$ channel, where $\rho(x)$ varies between 0.23 and 0.3 $e/\text{Å}^3$, and the other also along the $\langle 100\rangle$ direction but across the perfect lattice sites, i.e., across the nuclei of Ni atoms. We have included in this trajectory a vacancy in the position $a_0 = 2$, to evaluate the density of Ni at a vacant site because we will picture an Einstein oscillator as a "projectile" moving around a vacant site. The figure also displays as vertical shadowed areas the size of the atom cores as given by the cutoff radius of the pseudopotential for $2p$ electrons.

Two conclusions emerge from Fig. 3. One is that the density at the center of the channel (~0.23–0.30 $e/\text{Å}^3$), is similar but smaller than the equivalent jellium density giving the same stopping, $\rho = 0.75\ e/\text{Å}^3$ as discussed earlier. It implies that for a nonhomogeneous system, such as a crystal lattice, not only the density at the location of the nucleus of the projectile

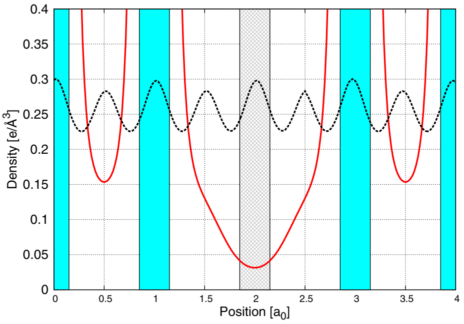

FIG. 3. (Color online) Electronic density in a fcc Ni target along two directions, the $\langle 100\rangle$ channeling direction at its center, and along a $\langle 100\rangle$ direction going across four atoms at positions zero, one, three, and four a_0, with a_0 the lattice parameter, and a vacancy at position $2a_0$. Note the factor of almost 10 between electronic density in the channel and at the vacant site.

is relevant, but also the density around that position. That is, the finite size of the projectile atom with its bound electrons samples regions of the target around its trajectory in a way that on average crystalline Ni stops a Ni ion traveling along the center of the channel as homogeneous jellium at $\sim 0.75\ e/\text{Å}^3$ density does. The second conclusion is that at a vacant site the electronic density is approximately ten times smaller than at the center of a channel. This fact, together with the order-of-magnitude difference in ion velocities at thermal energies, is precisely what will give rise to a different stopping for energetic projectiles than for atoms vibrating thermally around their lattice sites.

To establish the connections between S_e and e-ph interaction, we analyze now the energy dissipation of a Ni ion moving in a Ni crystal in a trajectory along a $\langle 100 \rangle$ direction passing on top of a perfect lattice site that is vacant, at two different constant velocities, namely, $v = 0.1$ and 0.05 a.u., corresponding to 15 and 3.75 keV, respectively. Phonon energies would require this study to be done at two orders of magnitude lower velocities, something that is computationally very demanding. To recover the dissipation under the real oscillatory dynamics, we will use the results for β obtained at $v = 0.05$ a.u. and plug it into the actual equation of motion of the damped harmonic oscillator at an amplitude corresponding to room temperature.

Figure 4 shows the potential energy for the BOA together with the energy according to TD-DFT for the atom moving from $x = -1.1$ to 1.1 Å, measured from the perfect crystal position where the vacancy sits, for the case $v = 0.1$ a.u. The ion in TD-DFT was set into motion at a distance from the vacancy larger than $|-1.1|$ Å, in order to reach that position well after the transient has disappeared. For visualization purposes, both curves have been vertically shifted to have equal value at $x = -1.1$ Å. Finally Fig. 4 also shows the difference between the two curves, i.e., the dissipated energy, whose slope is the stopping power or, in this interpretation, the e-ph interaction. As it is apparent, the slope of the curve, i.e., βv, is not constant but position dependent, reflecting the fact that β is a function of the density. The curves for $v = 0.05$ a.u. are slightly different, giving a larger β.

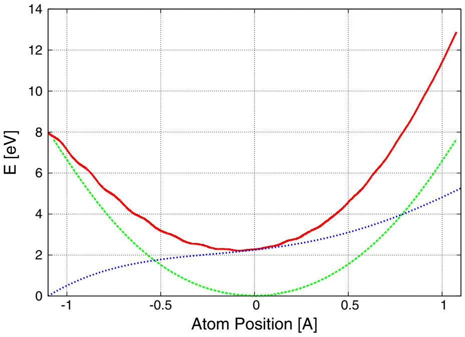

FIG. 4. (Color online) Energy vs position for an atom moving from left to right at constant velocity of $v = 0.1$ a.u. across its equilibrium position in the lattice at $x = 0$ according to both the Born-Oppenheimer approximation (dashed green curve), and nonadiabatic TD-DFT (solid-red curve). For visualization purposes, energy values have been made to coincide at $x = -1.1$ Å. The losses are given by the derivative of the curve representing the energy difference between the two approximations (dotted blue curve).

From the curvature of the BO curve in Fig. 4 we determine the equation of motion of the Einstein oscillator by extracting Hooke's constant κ of the parabolic potential, getting $\kappa = 13.076\ \text{eV}/\text{Å}^2$. This constant determines an oscillation frequency of 7.379 THz, or a period $T_0 = 0.136$ ps. This value is to be compared with the maximum phonon frequency in Ni, which is $\sim$9 THz [33], reminding us that the Einstein oscillator is generally in the upper side of the phonon spectrum. From the slope of the energy difference between the adiabatic and nonadiabatic calculation reported in Fig. 4 we extract the instantaneous β as a function of position x; from the curves in Fig. 3 we obtain the density as a function of position. We can then represent β as a function of density; these functions at the two velocities considered are shown in Fig. 5. For the small variations of density considered here corresponding to displacements compatible with room-temperature excitations, the function $\beta(\rho)$ is linear in density.

This result, namely, that β is different at different velocities, clearly shows that the damping is not simply proportional to the velocity at low velocities as is the case for jellium, Fig. 2. This velocity dependence is similar to the case reported in Ref. [24] for Au. Interesting to note is the fact that the velocity dependence for Ni is just the opposite to that of Au; while in Au the coupling decreases for low velocity, in Ni it increases. The reasons for that are to be found in the structure of the DOS close to the Fermi level: while in Au increasing the width around E_F increases the number of electrons involved, in Ni it is the opposite because the Fermi level sits on a high and narrow peak. For details see Figs. 4(d) and 5(d) in Ref. [34].

The motion of a damped harmonic oscillator of mass m and damping β is exponentially attenuated with a characteristic time $\tau_A = 2m/\beta$, while the energy decays with $\tau_E = m/\beta$. We find $\tau_E = 12.7$ ps for β determined at $v = 0.1$ a.u. and $\tau_E =$

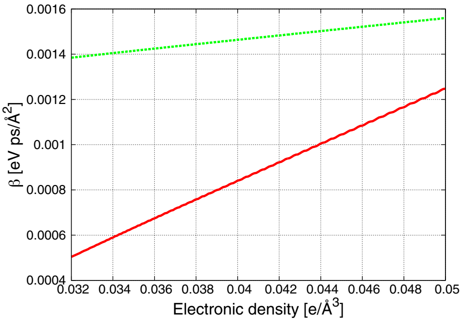

FIG. 5. (Color online) Instantaneous stopping power coefficient β vs local electronic density at the location of the projectile for a Ni atom moving along the $\langle 100 \rangle$ direction in Ni across a vacant site at 0.1 (green dashed curve) and 0.05 (red solid curve) a.u. of velocity.

4.4 ps for $v = 0.05$ a.u. We can expect that if β is calculated for lower velocities the characteristic relaxation time will be even smaller.

How does this value compare with the relaxation time for a 1.5-MeV ($v =$ 1-a.u.) Ni particle traveling at the center of a $\langle 100\rangle$ channel in fcc Ni? To make this comparison we will assume that for velocities between 0.1 and 1 a.u. the linear dependence of stopping with velocity is valid, which is not the case for velocities below 0.1 a.u., as we just discussed. Under this assumption, the relaxation time in a channel, namely, 3.5 ps, is 4.5 times shorter that the relaxation time around a vacancy. In terms of β for a particle traveling in a channel, $\beta(\rho = 0.25\ e/\text{Å}^3) = 2.06 \times 10^{-3}$ eV ps/Å^2, while for an atom traveling around its equilibrium position $\beta(\rho = 0.03\ e/\text{Å}^3) = 4.57 \times 10^{-4}$ eV ps/Å^2. In short, a variation of the host electronic density by a factor of $\sim$9 produces a variation of the strength of the coupling by a factor of $\sim$4.5.

This result partially solves the difficulty presented in the Introduction about the use of a piecewise function for β. However the precise relation between β and ρ at all densities, which is of relevance for practical implementations of TTM in classical MD simulations, requires also a dependence on velocity and/or on the structure of the DOS around E_{F}, a complex problem that still needs to be solved and is beyond the purpose of this paper.

IV. COMPARISON WITH THE PERTURBATIVE APPROACH

Finally, how does the e-ph relaxation time from TD-DFT compare with the value obtained using standard Bloch-Boltzmann-Peierls expression [35] describing the rates of change of electron and phonon distribution due to electron-phonon collision? In such approximation, the electron energy dissipation caused by the difference in electron and lattice temperatures is described by the theory developed by Allen [36]:

$$c_{\text{e}}\frac{dT_{\text{e}}}{dt} = -\pi\hbar k_{\text{B}}\lambda\langle\omega^2\rangle N(E_{\text{F}})(T_{\text{e}} - T_{\text{l}}) = -g(T_{\text{e}} - T_{\text{l}}) \quad (1)$$

where c_{e} is the electronic specific-heat capacity, $\langle\omega^2\rangle$ is the average value of phonon frequency, $N(E_{\text{F}})$ is the electronic density of states (DOS) per spin at Fermi energy, λ is the coupling constant, and T_{e} and T_{l} are electron and lattice temperatures, respectively.

The rigid muffin-tin potential approach (RMTA) proposed by Gaspari and Gyorffy [37] significantly simplifies the calculation of λ. It was used to calculate the Hopfield parameter $\eta = \lambda/(m\langle\omega^2\rangle)$, where m is atomic mass. Thus, the zero-temperature expression for the e-ph coupling is defined as

$$g = \pi\hbar k_{\text{B}}\eta N(E_{\text{F}})/m. \quad (2)$$

The electronic scattering phase shifts and electronic density of states, $N(E_{\text{F}})$, needed to calculate η, are obtained from the atomic sphere approximation of the Korringa-Kohn-Rostoker (KKR) [38,39] calculation. Within RMTA the spherically averaged part of the Hopfield parameter is equal (in Rydberg units) to

$$\eta = 2N(E_{\text{F}})\sum_{\ell}(\ell+1)M^2_{\ell,\ell+1}\frac{f_\ell}{2\ell+1}\frac{f_{\ell+1}}{2\ell+3}, \quad (3)$$

where f_ℓ is a relative partial DOS,

$$f_\ell = \frac{N_\ell(E_{\text{F}})}{N(E_{\text{F}})}, \quad (4)$$

and $M_{\ell,\ell+1}$ is the electron-phonon matrix element

$$M_{\ell,\ell+1} = \int_0^S R_\ell\frac{dV}{dr}R_{\ell+1}r^2dr, \quad (5)$$

where the gradient of the one-electron potential $V(r)$ and the radial solution of the Schrödinger equation, R_ℓ and $R_{\ell+1}$, were used. $M_{\ell,\ell+1}$ can be written [37] in terms of the phase shifts δ_ℓ or in terms of logarithmic derivatives of $D_\ell = rR'_\ell/R_\ell$ evaluated at the boundary of the atomic sphere [40–42]:

$$\begin{aligned} M_{\ell,\ell+1} = {} & -\phi_\ell(E_{\text{F}})\phi_{\ell+1}(E_{\text{F}})\{[D_\ell(E_{\text{F}}) - \ell] \\ & \times [D_{\ell+1}(E_{\text{F}}) + \ell + 2] + [E_{\text{F}} - V(S)]S^2\}, \quad (6) \end{aligned}$$

where $\phi_\ell(E_{\text{F}})$ is the amplitude of the ℓ partial wave.

Since both η and g are proportional to $N(E_{\text{F}})$, the resulting value strongly depends on the magnetic ordering in the material, namely, $\eta = 2.6$ eV/Å^2 for nonmagnetic Ni and $\eta = 2.1$ eV/Å^2 for the magnetic one. This difference is mainly caused by much higher $N(E_{\text{F}})$ for nonmagnetic Ni compared to the magnetic one. The corresponding coupling values, g, are equal to 14.9×10^{17} and 9.6×10^{17} W/m^3 K. According to Lin *et al.* [34], the highest value of g, 10.5×10^{17} W/m^3 K, is measured in transient thermoreflectance experiments [43]. The electron temperature in this experiment does not exceed 100 K. The phonon relaxation is obtained using the expression $\tau_{\text{ph}} = c_{\text{l}}/g$, where c_{l} is the lattice specific-heat capacity. The resulting phonon relaxation times at temperature equal to 300 K are 3.1 ps for nonmagnetic Ni and 4.8 ps for the magnetic one, where the temperature dependence was included following the approach proposed by Wang *et al.* [44]. This approach allows us to include scattering of phonons on electrons away from the Fermi surface. Following Wang *et al.* and Lin *et al.* [34] the temperature-dependent electron-phonon coupling was calculated using

$$g(T_{\text{e}}) = \pi\hbar k_{\text{B}}\frac{\eta}{M}N(E_{\text{F}})\int_{-\infty}^{\infty}dE\left[\frac{N(E)}{N(E_{\text{F}})}\right]^2\left[-\frac{\partial f}{\partial E}\right], \quad (7)$$

where $-\frac{\partial f}{\partial E}$ is the derivative of the equilibrium Fermi distribution function. At low electronic temperatures, T_{e}, this function reduces to a delta function, and the expression for g reduces to Eq. (2). Figure 6 shows the calculated $g(T_{\text{e}})$ together with available experimental data obtained in transient thermoreflectance experiments [43] and pump-probe transmission experiments [45] and deduced from the two-temperature model for surface melting [46] (see detailed discussion in the paper by Lin *et al.* [34]). The calculated dependence is in very reasonable agreement with experiment.

V. DISCUSSION

The e-ph interaction represented in terms of a relaxation time has then been calculated with two different approaches, namely, in a semiclassical way, as the low-velocity limit of electronic stopping, producing a value for an Einstein oscillator of $\tau = 12.7$ ps for β calculated at $v = 0.1$ a.u and

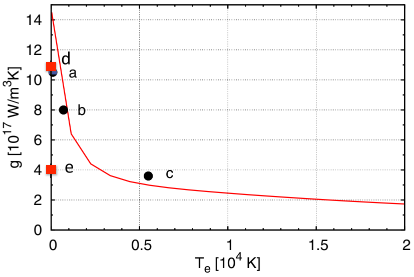

FIG. 6. (Color online) Calculated (red line) and experimental (blue dots) electron-phonon coupling as a function of electron temperature. The data point at "a" is from Ref. [43], at "b" is from Ref. [45], and at "c" is from Ref. [46]. Also shown are the points calculated as stopping power, with an instantaneous stopping power coefficient β determined with a projectile traveling at $v = 0.05$ a.u. of velocity (point d), and at $v = 0.1$ a.u. (point e). For details see text.

$\tau = 4.4$ ps for β calculated at $v = 0.05$ a.u, and as given by linear-response theory, producing a value of $\tau = 3.5$ ps at 0 K. The similarity of these results is surprising if we consider how different the two approaches are. To mention some, the e-ph interaction seen as an electronic stopping process uses Ehrenfest dynamics, which is known to misrepresent some dissipation channels [47]. Also, our calculation is for an Einstein mode, a highly localized superposition of all normal modes, while the quantum-mechanical calculation involves a thermal population of phonons. In addition, the quantum-mechanical calculation is very sensitive to the electronic DOS at the Fermi level, a usual source of numerical inaccuracy. However, the main assumption is the velocity proportionality of the stopping, as represented in Fig. 2 for jellium: the βs used for the calculation of the attenuation of an Einstein oscillator were obtained at $v = 0.1$ and 0.05 a.u., while the velocity of an atom moving in the phonon regime is in the range of $v \sim 0.0001$ a.u., implying that an even larger value of β may be found if the velocity is further reduced.

In a recent paper, Zeb *et al.* showed that, for protons on Au, where the Fermi level is in the *s* band close to the upper limit of the *d* band, the experimentally reported nonlinear behavior of stopping power versus velocity (lower slope of the stopping at lower velocities) is due to a gradual crossover as excitations tail into the *d* electron spectrum [24]. Using a similar argument for our case of Ni in Ni, we find a justification for the opposite behavior, namely, an increase in the slope of the stopping as the velocity decreases, as shown in Fig. 6. Our calculated dependence of the e-ph coupling on electronic temperature in Ni, as well as the work by Lin *et al.* [34], show a strong negative dependence in the temperature regime relevant for high-energy laser pulses, i.e., electronic temperatures up to 10^4 K. As the electronic temperature increases, electrons in a window of width $k_B T$ around E_F start to participate in the coupling and since in Ni the $N(E_F)$ is very high and decreases at both sides of E_F the coupling has a strong negative temperature dependence.

The e-ph interaction seen as a stopping process can be analyzed with the same argument, namely, the electrons that participate in the stopping are those around E_F with a width that increases with projectile velocity. Using a semiclassical argument we see that for a given projectile velocity v electrons in a range $E_F \pm 2\hbar k_F v$ become relevant for the nonadiabatic energy exchange. Therefore a meaningful comparison between electronic stopping and e-ph coupling can be made when $v \sim k_B T/(2\hbar k_F)$, with T the electronic temperature. So, for example, an electronic temperature of 5000 K corresponds, in this analogy, to a projectile velocity of 0.011 a.u. (counting ten valence electrons per nickel ion) or 0.006 a.u. (two *s* electrons per nickel ion). This argument is a good candidate to explain why the e-ph and stopping power calculations agree when both theories are compared at the appropriate limits, i.e., when both approaches effectively probe the same range of DOS around E_F.

At high electronic temperature (or in the presence of defects affecting the band structure) the exact value of $N(E_F)$ of the perfect crystal becomes less relevant, and is replaced by an average in the range $E_F \pm k_B T$. In fact, for disordered alloys, liquid phase, or high temperature, we expect that the semiclassical stopping method to the two-temperature model could become a practical and accurate approach.

VI. CONCLUSION

In summary, using TD-DFT we simulated an oscillatory ion motion with thermal energies subject to the damping created by electronic excitations, as well as an energetic ion traveling in a channel direction in a crystal. We interpreted both damping processes as being two aspects of the same physical phenomenon, differentiated only by the density of the target that the moving particle is able to explore at different energy ranges. This connection between the two processes is not new in molecular physics: Several years ago a similar assumption was made by Persson and Hellsing [48,49] to explain the attenuation of oscillating molecules or adatoms on the surface of a metal. In this paper we give a full quantitative evaluation of the process for a metal with *ab initio* accuracy. Finally, in a recent paper by Mason [50] an explicit form is given for the damping coefficient in terms of a damping tensor derived from a tight-binding model, adding more complexity to our simple scalar damping term. Still Mason's model considers S_n and S_e as distinct phenomena acting at different energy scales. Perhaps a combination of both approaches may give the most complete description on nonadiabatic phenomena in solids.

The classical trajectory is not only a technical shortcut but also makes the connection with state-of-the-art molecular-dynamics simulations. The proposition presented in this paper of calculating the e-ph interaction as a particular case of an electronic stopping process provides a simple solution to the empiricism present today in molecular-dynamics simulations of nonadiabatic processes in energetic ion-solid interactions, by attributing the differences in value of the damping coefficient β at different ion energies to the different values of the host electronic density found by moving particles when in the high-energy regime or in the thermal energy regimes. A practical implementation of this approach in a MD simulation would require an on-the-fly determination of the electronic density, obtained, for example, by superposition of spherical atomic densities (as it is currently feasible in the embedded atom method), and a precise functional form relating β to ρ as obtained with the presented method.

ACKNOWLEDGMENTS

Work was performed at the Energy Dissipation to Defect Evolution Center, an Energy Frontier Research Center funded by the U.S. Department of Energy (Grant No. 2014ORNL1026) at Los Alamos and Oak Ridge National Laboratories. This research used resources provided by the LANL Institutional Computing Program. LANL, an affirmative action/equal opportunity employer, is operated by Los Alamos National Security, LLC, for the National Nuclear Security Administration of the U.S. Department of Energy under Contract No. DE-AC52-06NA25396. Work by A.A.C. was performed under the auspices of the U.S. Department of Energy by Lawrence Livermore National Laboratory under Contract No. DE-AC52-07NA27344.

---

[1] M. Born and R. Oppenheimer, Ann. Phys. (Leipzig) **389**, 457 (1927).
[2] F. Seitz and J. S. Koehler, Solid State Phys. **2**, 305 (1956).
[3] I. M. Lifshitz, M. I. Kaganov, and L. V. Tanatarov, J. Nucl. Energy **A12**, 69 (1960).
[4] A. Caro and M. Victoria, Phys. Rev. A **40**, 2287 (1989).
[5] R. Fleischer, P. Price, and R. Walker, J. Appl. Phys. **36**, 3645 (1965).
[6] D. Lesueur and A. Dunlop, Radiat. Eff. Defects Solids **126**, 163 (1993).
[7] G. Schiwietz, P. Grande, B. Skogvall, J. P. Biersack, R. Koehrbruck, K. Sommer, A. Schmoldt, P. Goppelt, I. Kadar, S. Ricz *et al.*, Phys. Rev. Lett. **69**, 628 (1992).
[8] J. Rzadkiewicz, A. Gojska, O. Rosmej, M. Polasik, and K. Slabkowska, Phys. Rev. A **82**, 012703 (2010).
[9] C. Dufour, A. Audouard, F. Beuneu, J. Dural, J. P. Girard, A. Hairie, M. Levalois, E. Paumier, and M. Toulemonde, J. Phys. Condens. Matter **5**, 4573 (1993).
[10] E. M. Bringa and R. E. Johnson, Phys. Rev. Lett. **88**, 165501 (2002).
[11] D. M. Duffy and A. M. Rutherford, J. Phys. Condens. Matter **19**, 016207 (2007).
[12] F. Gygi and G. Galli, Phys. Rev. B **65**, 220102 (2002).
[13] D. Dundas, E. McEniry, and T. Todorov, Nature Nanotech. **4**, 99 (2009).
[14] A. M. Rutherford and D. M. Duffy, J. Phys. Condens. Matter **19**, 496201 (2007).
[15] I. T. Todorov, B. Smith, K. Trachenko, and M. T. Dove, Capab. Comput. **6**, 12 (2005).
[16] I. T. Todorov, B. Smith, M. T. Dove, and K. Trachenko, J. Mater. Chem. **16**, 1911 (2006).
[17] C. P. Race, D. R. Mason, M. W. Finnis, W. M. C. Foulkes, A. P. Horsfield, and A. P. Sutton, Rep. Prog. Phys. **73**, 116501 (2010).
[18] E. Zarkadoula, S. L. Daraszewicz, D. M. Duffy, M. A. Seaton, I. T. Todorov, K. Nordlund, M. T. Dove, and K. Trachenko, J. Phys. Condens. Matter **26**, 085401 (2014).
[19] A. E. Sand, S. L. Dudarev, and K. Nordlund, Europhys. Lett. **103**, 46003 (2013).
[20] E. E. Zhurkin and A. S. Kolesnikov, Nucl. Instrum. Methods Phys. Res. B **202**, 269 (2003).
[21] S. Proennecke, A. Caro, and M. Victoria, J. Mater. Res. **6**, 483 (1990).
[22] M. J. Puska and R. M. Nieminen, Phys. Rev. B **27**, 6121 (1983).
[23] P. M. Echenique, R. M. Nieminen, and R. H. Ritchie, Solid State Commun. **37**, 779 (1981).
[24] M. A. Zeb, J. Kohanoff, D. Sánchez-Portal, A. Arnau, J. I. Juaristi, and E. Artacho, Phys. Rev. Lett. **108**, 225504 (2012).
[25] E. Runge and E. K. U. Gross, Phys. Rev. Lett. **52**, 997 (1984).
[26] A. Schleife, E. W. Draeger, Y. Kanai, and A. A. Correa, J. Chem. Phys. **137**, 22A546 (2012).
[27] J. M. Pruneda, D. Sanchez-Portal, A. Arnau, J. I. Juaristi, and E. Artacho, Phys. Rev. Lett. **99**, 235501 (2007).
[28] A. A. Correa, J. Kohanoff, E. Artacho, D. Sanchez-Portal, and A. Caro, Phys. Rev. Lett. **108**, 213201 (2012).
[29] A. Schleife, Y. Kanai, and A. A. Correa, Phys. Rev. B **91**, 014306 (2015).
[30] J. F. Ziegler, Nucl. Instr. Meth. B **219–220**, 1027 (2004).
[31] J. F. Ziegler, SRIM-2003, http://www.srim.org/SRIM/SRIMPICS/STOP02/STOP0213.gif.
[32] A. Ojanpera, A. V. Krasheninnikov, and M. Puska, Phys. Rev. B **89**, 035120 (2014).
[33] M. Kresch, O. Delaire, R. Stevens, J. Y. Y. Lin, and B. Fultz, Phys. Rev. B **75**, 104301 (2007).
[34] Z. Lin, L. Zhigilei, and V. Celli, Phys. Rev. B **77**, 075133 (2008).
[35] J. M. Ziman, *Electrons and Phonons* (Oxford University, London, 1960).
[36] P. B. Allen, Phys. Rev. Lett. **59**, 1460 (1987).
[37] G. D. Gaspari and B. L. Gyorffy, Phys. Rev. Lett. **28**, 801 (1972).
[38] J. Korringa, Physica **13**, 392 (1947).
[39] G. M. Stocks, W. M. Temmerman, and B. L. Gyorffy, Phys. Rev. Lett. **41**, 339 (1978).
[40] D. G. Pettifor, J. Phys. F **6**, 1009 (1977).
[41] D. Glötzel, D. Rainer, and H. R. Schober, Z. Phys. B **35**, 317 (1979).
[42] H. L. Skriver and I. Mertig, Phys. Rev. B **32**, 4431 (1985).
[43] A. P. Caffrey, P. E. Hopkins, J. M. Klopf, and P. M. Norris, Microscale Thermophys. Eng. **9**, 365 (2005).
[44] X. Y. Wang, D. M. Riffe, Y. S. Lee, and M. C. Downer, Phys. Rev. B **50**, 8016 (1994).
[45] E. Beaurepaire, J.-C. Merle, A. Daunois, and J.-Y. Bigot, Phys. Rev. Lett. **76**, 4250 (1996).
[46] S.-S. Wellershoff, J. Güdde, J. Hohlfeld, J. G. Müller, and E. Matthias, Proc. SPIE **3343**, 378 (1998).
[47] A. P. Horsfield *et al.*, Comp. Mat. Sci. **44**, 16 (2008).
[48] M. Persson and B. Hellsing, Phys. Rev. Lett. **49**, 662 (1982).
[49] B. Hellsing and M. Persson, Phys. Scr. **29**, 360 (1984).
[50] D. Mason, J. Phys. Condens. Matter **27**, 145401 (2015).

IV

Reprinted with permission from A. Tamm, G. Samolyuk, A. A. Correa, M. Klintenberg, A. Aabloo, and A. Caro, The electron-phonon interaction within classical molecular dynamics, Physical Review B, 2016. Copyright 2016 by the American Physical Society.

The electron-phonon interaction within classical molecular dynamics

A.Tamm[1,2], G. Samolyuk[3], A. A. Correa[4], M. Klintenberg[5], A. Aabloo[2], and A. Caro[1]
1-Materials Science and Technology Division, Los Alamos National Laboratory, Los Alamos, NM 87545, USA
2-IMS Lab, Institute of Technology, University of Tartu, 50411 Tartu, Estonia
3-Materials Science and Technology Division, Oak Ridge National Laboratory, Oak Ridge, TN 54321, USA
4-Lawrence Livermore National Laboratory, Livermore CA, 94550, USA and
5-Department of Physics and Astronomy, Uppsala University, 75120 Uppsala, Sweden

We present a model for non-adiabatic classical molecular dynamics simulations that captures with high accuracy the wave-vector $q-$dependence of the phonon lifetimes, in agreement with quantum mechanics calculations. It is based on a local view of the e-ph interaction where individual atom dynamics couples to electrons via a damping term that is obtained as the low velocity limit of the stopping power of a moving ion in a host. The model is parameter free, as its components are derived from *ab initio*-type calculations, is readily extended to the case of alloys, and is adequate for large scale molecular dynamics computer simulations. We also show how this model removes some oversimplifications of the traditional ionic damped dynamics commonly used to describe situations beyond the Born-Oppenheimer approximation.

Keywords:

I. INTRODUCTION

Computational materials science is one of the fastest growing areas in physics and chemistry. Scientists have long used computers to model materials and their performance; but today, with ever-growing supercomputers, which employ millions of microprocessors to tackle simulations once considered intractable, the accuracy of some simulations are able to reliably predict properties of new materials without testing. However, material properties often depend on phenomena that take place over several scales, from nanometers to meters, from billionth of a second to years. No computer in the near future will be able to solve such challenges within a single theoretical framework, for example, quantum mechanics at the atomic scale.

To bypass this limitation, scientists have for years been developing the concept of multi-scale modeling. This approach combines different models in order to cover the full range of length and time scales of interest for a particular problem. The most common approach to multi-scale modeling is called information passing. In this method simulations of matter at one scale are based on the results of simulations at a lower (more finely detailed) scale. The challenge to perform a coherent simulation of a material lies on building robust connections between such different scales.

One of the most difficult connections is between the electronic and the atomic scales, specifically, between quantum mechanics, QM, for electrons and classical mechanics for the ions, because classical mechanics is not a coarser view of QM. One of the best examples of success in this area is the development of the so called 'classical many body potentials' [1, 2] to describe ion-ion interactions, done 30 years ago. It describes the potential energy of an ensemble of atoms as a simple non linear function of the sum of pair interactions. This assumption captures the essence of metallic cohesion, which in a tight binding language says that bonding is a function of band width, which itself is a function of wave-function overlaps, and it does that at an insignificant computational cost compared to any QM model for the electrons. This model gives materials scientists a tremendous power to predict atomic scale behavior in many metals and alloys and represents a seminal contribution to computational materials science, and probably the most successful connection between scales in the multi-scale paradigm.

In this work we present a classical mechanics model that captures the essence of another QM phenomenon namely the electron-phonon, e-ph, interaction, and does so also at an insignificant computational cost. The model presented here captures with high accuracy the wave-vector q dependence of the phonon lifetimes in agreement with sophisticated QM calculations. It is based on a local and instantaneous view of the e-ph interaction where individual atom dynamics couples to electrons via a damping term that is obtained as the low velocity limit of the stopping power of a moving ion in a material. Moreover, the model is parameter free, as its components are derived from *ab initio*-type calculations.

In a recent paper [3] we calculated the e-ph interaction as a particular case of an electronic stopping process, providing a simple solution to the empiricism present today in molecular dynamics simulations of non-adiabatic processes [4, 5].

The inclusion of electronic effects into classical MD simulations is usually achieved using Langevin dynamics, where a friction term, $-\beta v$, added to the Newton equations of motion, removes energy from moving atoms, while a random force term simulates the stochastic thermalizing collisions with electrons. The approach proposed years ago by Caro *et al.* [6], treats the β term as a function of the local electronic density of the host, and the electronic system as a large heat bath at a constant temperature. Today, that simple approach has been largely improved by treating the energetics of the elec-

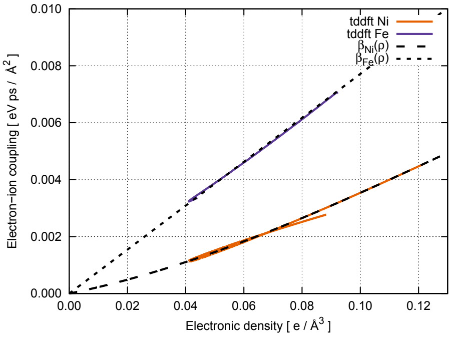

Figure 1: Damping term β in the Langevin equations as a function of local electronic density calculated using TDDFT for Ni and Fe projectiles moving across a vacancy site in an fcc Ni crystal. Also plotted is the fitted quadratic function for $\beta(\rho)$ that was used in MD simulations.

tronic system as a continuum described by a specific heat and a thermal conductivity, whose thermal state is solved via the heat equation on a mesh, simultaneously with the ionic equations of motion. This approach, known as the Two Temperature hybrid MD Model, TTM-MD, represents the state of the art for non-adiabatic MD simulations of radiation damage [5], although it is important to mention that in most cases, the β term is assumed constant. When it is assumed to be a function of the local electronic density, it has been proven to give a much better agreement with quantum mechanical calculations [7].

In Ref. [3] we describe β as a specific function of the local host electronic density, as seen by the moving atom. This simplifying assumption naturally accounts for the differences in β values seen by energetic projectiles visiting regions of high electronic density of the host, and slow, thermal, atoms moving around their equilibrium positions, where the density contributed by the other, host, atoms is at its minimum. We refer the reader to that paper for the introductory discussion to the subject.

II. METHOD

In this paper we first use time dependent density functional theory, TD-DFT, to evaluate $\beta(\rho)$ for both a Ni atom moving around its equilibrium position in a Ni lattice, *i.e.* $\beta_{\mathrm{Ni}}(\rho)$, and an Fe atom substituting a Ni one in the same Ni lattice, *i.e.* $\beta_{\mathrm{Fe}}(\rho)$. This last case provides the information needed to describe the e-ph interaction in NiFe alloys. With these functions we then evaluate the phonon lifetime that results from the e-ph interaction; we compare these results with QM calculations based on perturbation theory.

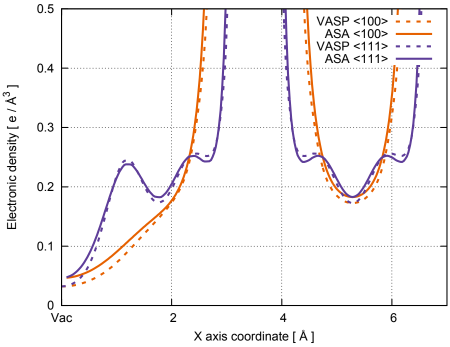

Figure 2: Electronic density in Ni crystal with a single vacancy along $\langle 100\rangle$ (red) and $\langle 110\rangle$ (blue) directions. The solid line is obtained with ASA method and dashed calculated using VASP. The symbol Vac shows the location of a vacancy in Ni crystal.

Our model is a modified version of the Langevin equations of motion describing an ensemble of classical degrees of freedom (Boltzmann statistics) in contact with a heat reservoir, in our case, the electrons, namely,

$$\mathbf{F}_I = -\boldsymbol{\nabla}_I U(\{\mathbf{R}_J\}_J) - \beta_I(\rho^*(\mathbf{R}_I))\mathbf{v}_I^* + \boldsymbol{\eta}_I \tag{1}$$

$$\rho^*(\mathbf{R}_I) = \sum_{J\neq I} \rho_J(R_{IJ}) \tag{2}$$

$$\mathbf{v}_I^* = \frac{1}{\rho^*(\mathbf{R}_I)} \sum_{J\neq I} \rho_J(R_{IJ})(\mathbf{v}_I - \mathbf{v}_J) \tag{3}$$

with each component of the random force $\boldsymbol{\eta}_I$ defined by,

$$\langle \eta_I^{(i)}(t)\rangle = 0 \tag{4}$$

$$\langle \eta_I^{(i)}(t)\eta_I^{(j)}(t')\rangle = \delta_{ij}\delta(t-t')2\beta_I(\rho(\mathbf{R}_I))k_{\mathrm{B}}T_{\mathrm{e}}(\mathbf{R}_I) \tag{5}$$

where $\mathbf{F}_I$ is the force acting on atom I, $U(\{\mathbf{R}\}_J)$ is the potential energy of the system that depends on the coordinate of all the atoms and is given by an empirical potential or by a *ab initio* ground state total energy calculation; $\beta_I(\rho(\mathbf{R}_I))$ is the viscous damping force or ion-electron coupling strength function, which depends on the chemical nature of the atom I, and its argument $\rho(\mathbf{R}_I)$ is the electronic density of the host at the position where atom I is positioned, defined in Eq. 2, $\mathbf{v}_I^*$ is the relative velocity between atom I and the host electronic density, as defined by Eq. II, and η_I is a random force defined by its mean value, Eq. 4, and its variance, Eq. , where k_{B} is the Boltzmann constant, $T_{\mathrm{e}}(\mathbf{R}_I)$ is the electronic temperature at position $\mathbf{R}_I$, and M_I is the mass of ion I.

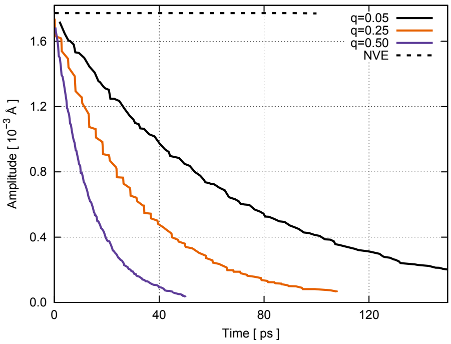

Figure 3: The amplitude decay during the e-ph MD simulation of the phonon longitudinal modes in fcc Ni crystal along $\langle 100 \rangle$ direction with wave-vectors 0.05, 0.25 and 0.50 (in units of $2\pi/a$). The simulation contains 32000 atoms in a cubic supercell. Horizontal dotted line, shows the result when dissipative term in Eq. 1 is turned off (and energy is conserved as in a normal NVE simulation.)

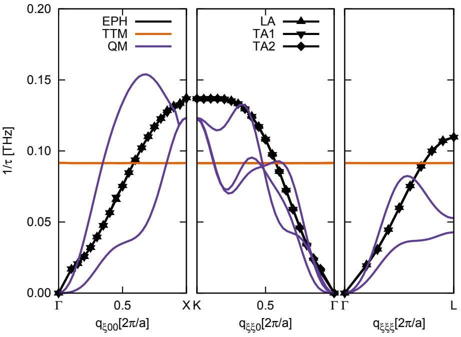

Figure 4: Inverse phonon lifetimes in a fcc Ni crystal along $\langle 100 \rangle$, $\langle 110 \rangle$, $\langle 111 \rangle$ directions. The polarization vectors investigated are shown in the legend. Results are shown for the model described in the text, for a perturbative QM calculation, and for the standard two temperature model.

Note the way we have written the density $\rho^*(\mathbf{R})$ at position $\mathbf{R}$ in Eq. 2; it is defined as the sum of spherical atomic densities $\rho_J(\mathbf{R}_{IJ})$ of neighboring atoms, which carry the information about the chemical nature of atoms at positions $\mathbf{R}_J$ that contributes to the density at position $\mathbf{R}_I$. $\rho(\mathbf{r})$ itself does not depend explicitly upon the chemical nature of the atoms contributing to it. This atomic sphere approximation, ASA, is similar to that at the basis of the embedded atom model, EAM [1, 2], providing a fast algorithm to calculate it on-the-flight. Also note that, according to Eq. the velocity $\mathbf{v}_I^*$ is the velocity of atom I *relative* to the velocity of the electronic density. This point has been so far overlooked in the standard implementation of the TTM-MD in the popular MD code LAMMPS [8] or DL-POLY [9], and has significant consequences on the wave vector dependence of phonon lifetimes, as we show below, and on the presence of an artificial damping for a solid under rigid motion.

The function $\beta_I(\rho)$ is found in a two-step process. First, $\beta_I(\mathbf{R})$ is obtained along a TD-DFT simulations of a low (thermal) velocity atom moving across a vacant site in the crystal. From the total electronic energy in the simulation an instantaneous electronic stopping power, $S_\mathrm{e}(\mathbf{R})$ is obtained, whose slope is $\beta_I(\mathbf{R})$. We used the code Qbox with modifications to perform explicit time-dependent electron dynamics (TD-DFT)[10] and the procedure is similar to that described in [3]. Second, the function $\rho^*(\mathbf{R})$ is obtained using the ASA. The atomic spherically-symmetric densities were obtained from the Opium package [11] for isolated Ni and Fe atoms. VASP calculations [12, 13] for the actual electronic density in bulk fcc Ni show that ASA is in a reasonably good agreement with DFT results (fig. 2), validating the ASA approach for metals. (GGA was used all along the DFT calculations.) In Fig. 2 we see that the largest discrepancy occurs precisely at the location of the vacancy where the actual density is smaller than the ASA value, reflecting the effects of metallic bonding. Finally, relating $\beta_I(\mathbf{R})$ to $\rho(\mathbf{R})$ and eliminating $\mathbf{R}$, the function $\beta(\rho)$ in Eq. 1 is obtained. Figure 1 shows the results for $\beta_\mathrm{Ni}(\rho)$ corresponding to a Ni atom in a fcc Ni lattice, and for $\beta_\mathrm{Fe}(\rho)$ corresponding to an Fe atom in the same Ni lattice. The calculations are not magnetic for simplicity, and also because in the envisioned applications the magnetism can be seen as a small perturbation.

Note in this figure, in particular for the case of the Ni atom in fcc Ni where the simulation ran for a longer trajectory, that the actual value of S_e is not exactly a function of the density at the actual position of the moving atom, namely: S_e for the atom approaching the vacancy is not the same as S_e for the atom departing from it, at symmetrical positions, where the host density is the same. This difference reflects the fact that the stopping is in fact a function of the electronic density of the host as well as that of the moving particle, which lags behind its nucleus or, in general, the stopping is a function of the history. This local density approximation is, nevertheless, an excellent approach for low velocity atoms, as Fig 1 suggests, but is less accurate for projectiles in the MeV range. This is analogous in spirit to the EAM, in this case the friction itself is taken as a function of the environment density. We discuss this subject in a forthcoming publication.

We implemented this model as a new ‘fix’ in the MD

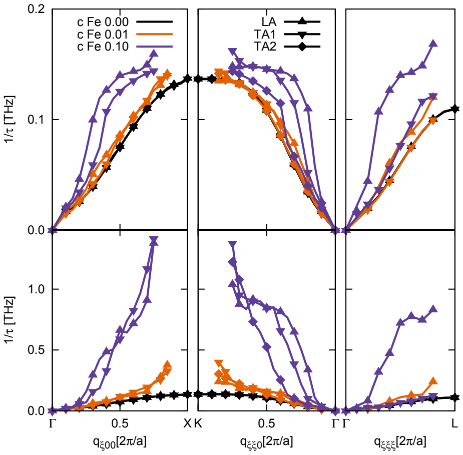

Figure 5: Inverse phonon lifetimes for a NiFe random solid solution in fcc phase as a function of wavevector q, for three polarizations at various number concentrations (c Fe 0.00, 0.01, 0.10). These are obtained with our MD model from the decay of an initial phonon-like excitation characterized by wavevector q along principal directions in the Brillouin zone, and polarization (longitudinal and two transversal). Values reported on the upper panel correspond to the e-ph contribution alone, measure from the energy transferred to the electronic system; those of the lower panel correspond to the actual decay of the mode that contains the e-ph interaction plus the decay produced by the disorder.

code LAMMPS [8] and treated the electronic system as it is usually done in the TTM-MD, namely by solving the heat diffusion equation on a grid. For our purpose in this work of determining phonon lifetimes, only energy removal from the ionic system to the electrons is studied, with the random force in Eq. 1 turned off. Phonon-phonon scattering is contained in the adiabatic potential U and explicit magnon dynamics is still omitted.

III. RESULTS AND DISCUSSION

To study phonon lifetimes we prepared each initial state with displacements corresponding to particular polarizations and wave-vectors $\mathbf{q}$ along high symmetry directions in the Brillouin zone, and monitor their amplitude of each mode as it decreases with time, as shown in Fig. 3.

The initial amplitude is small enough (0.0018 Å) to make anharmonic effects (*i.e.* phonon-phonon interactions) negligible. From a fitting to the exponential decay of its amplitude we obtain the lifetimes, as reported in Fig. 4.

To check the accuracy of these predictions, we evaluate the phonon lifetimes from density-functional perturbation theory [14–16] (DFPT) in a pseudopotential plane-wave approach, as implemented in Quantum Espresso (QE) package [18], using ultrasoft [19] pseudopotential from the QE database. The results are shown in Fig. (4) as well. The electronic structure and phonon dispersion for nonmagnetic Ni were calculated within the Generalized Gradient Approximation (GGA), with the exchange-correlation functional parameterized according to Perdew, Burke, and Ernzerhof [17]. A plane wave kinetic energy cut off of 40 Ry (and charge density cutoff of 240 Ry) give accurate values of phonon dispersion. The integration over the Brillouin zone (BZ) used a smearing of 0.02 Ry. The calculation of phonon lifetime requires an integration of the double delta over the Fermi surface [20] with a high accuracy. BZ summations were carried out over a $30 \times 30 \times 30$ grid for the k-grid electronic integration, smearing equal to 0.005 Ry and $6 \times 6 \times 6$ for the phononic q-grid integration, according to the Monkhorst-Pack scheme. We performed the phononic BZ integration to calculate the electron-phonon coupling constant, λ [20]. The value obtained, $\lambda = 0.24$, is very close to 0.26, obtained previously [3, 21] using a rigid muffin-tin potential approach (RMTA) [22]. This λ value is calculated using value of calculated Hopfield parameter [21] and expression

$$\lambda = \delta/(m\langle\omega^2\rangle), \tag{6}$$

where δ is Hopfield parameter calculated in RMTA, and $\langle\omega^2\rangle$ is averaged value of calculated phonon frequencies. This value are also in reasonable agreement with the $\lambda = 0.31$ obtained by Allen from resistivity experiment [23].

Finally, Fig 4 also gives the lifetime predictions for the standard TTM-MD approach, which assumes a constant β and uses the absolute ion velocity in the term βv. It can be seen that no $\mathbf{q}$-dependence is obtained, and moreover, damping is present even at $\mathbf{q} = 0$, *i.e.* for rigid translation (evidencing that the total linear momentum is not conserved). Three main conclusions emerge from this figure: (i) the classical mechanics e-ph interaction model that we present here predicts phonon lifetimes in remarkably good agreement with quantum mechanical calculations; (ii) the main limitation of the model seems to be the inability to predict different values for longitudinal and transverse polarization; (iii) the typical model used so far to account for non-adiabatic atomic motion, the TTM-MD with constant β and absolute velocities, is unable to give any q-dependence, however it is captured with our method.

The absence of polarization effect in the life-times stems from the simplicity of the model and the scalar character of the dissipation (friction force is always anti-parallel to the velocity). A more general model (including tensorial β or dependence on acceleration) could in principle also recover polarization effects.

The model presented so far is readily extended for alloys; we study the case of NiFe. According to Eqs. 1 the function β_I depends on the chemical identity of atom I, and its argument is the host density at the location of atom I, which is the sum of atomic densities of atoms at sites J, with their own chemical identity that defines such density, Eq. 2. Therefore describing alloys requires the calculation of the electronic stopping power of all the species in consideration in a host that is representative of the alloy. In the case presented here we assume it to be pure Ni, valid for small concentrations in NiFe.

Fig. 1 shows $\beta_{\mathrm{Fe}}(\rho)$ for an Fe atom moving around a vacancy in fcc Ni. Fig. (5) shows the lifetimes resulting from both the e-ph interaction and the phonon scattering produced by the disorder. Clearly the disorder contribution is at least one order of magnitude larger than the e-ph part. To extract the phonon lifetime from the total attenuation we monitor the energy transferred to the electronic system, instead of the decay of the phonon itself. The results are shown in Fig. 5 which show how alloying increases the coupling mostly at the zone edges. We also observe a splitting between longitudinal and transverse branches, absent in the pure Ni case.

In all the phonon lifetime MD calculations an $20 \times 20 \times 20$ fcc simulation box consisting of 32000 atoms was used. Ni-Fe alloys were constructed by substituting the Ni atoms with Fe randomly to obtain the required concentration. All the structures were initially relaxed to obtain the equilibrium lattice parameter. Afterwards different phonon modes used in the study were created by displacing the atoms. The Ni interatomic potential by Mishin *et al.* [24] was used in the phonon lifetime studies for pure Ni crystal and the potential by Bonny *et al.* [25] was used in the case of Ni-Fe alloy.

IV. CONCLUSIONS

We propose a non adiabatic model for classical MD that accurately reproduces e-ph interaction in both strength and **q**-dependence. The model is based on treating the e-ph interaction as a low velocity case of electronic stopping power, and therefore uses a quantum mechanical technique, namely TD-DFT, to evaluate its strength, which becomes then parameter free. Using a local approximation to relate the e-ph coupling to the host electronic density, and complemented with a atomic sphere approximation to obtain the local electronic density at low computational cost, the model is readily extended to alloys. The predictions are validated by comparison to quantum mechanical calculations, showing an excellent agreement. This model represents quantitatively accurate approach to describe non adiabatic aspects of ion-electron dynamics within a classical mechanics framework.

Acknowledgments

Work performed at the Energy Dissipation to Defect Evolution Center, an Energy Frontier Research Center funded by the U.S. Department of Energy (Award Number 2014ORNL1026) at Los Alamos and Oak Ridge National Laboratories. This research used resources provided by the LANL Institutional Computing Program. LANL, an affirmative action/equal opportunity employer, is operated by Los Alamos National Security, LLC, for the National Nuclear Security Administration of the U.S. DOE under contract DE-AC52-06NA25396. Work by AAC performed under the auspices of the U.S. Department of Energy by Lawrence Livermore National Laboratory under Contract DE-AC52-07NA27344.

---

[1] M. S. Daw and M. I. Baskes, Phys. Rev. B 29, 6443 (1984).
[2] M. W. Finnis and J. E. Sinclair, Philos. Mag. A 50, 45 (1984).
[3] A. Caro, A. A. Correa, A. Tamm, G. D. Samolyuk and G. M. Stocks, Phys. Rev. B 92, 144309 (2015).
[4] M. C. Ridgway, T. Bierschenk, R. Giulian, *et al.*, Phys. Rev. Lett. 110, 245502 (2013).
[5] D. M. Duffy and A. M. Rutherford, J. Phys. Condens. Matter 19, 016207 (2007).
[6] A. Caro and M. Victoria, Phys. Rev. A 40, 2287 (1989).
[7] C. P. Race, D. R. Mason, M. W. Finnis, W. M. C. Foulkes, A. P. Horsfield, and A. P. Sutton, Rep. Prog. Phys. 73, 116501 (2010).
[8] S. J. Plimpton, Comput. Phys. 117, 1 (1995).
[9] S.L. Daraszewicz and D.M. Duffy, Nuclear Instruments and Methods in Physics Research Section B: Beam Interactions with Materials and Atoms 303, 112-115 (2013)
[10] A. Schleife, E. W. Draeger, Y. Kanai, and A. A. Correa, J. Chem. Phys. 137, 22A546 (2012).
[11] Opium - pseudopotential generation project, http://opium.sourceforge.net
[12] G. Kresse and J. Hafner, Phys. Rev. B 47, 558 (1993).
[13] G. Kresse and D. Joubert, Phys. Rev. B 59, 1758 (1999).
[14] N. E. Zein, Fiz. Tverd. Tela 26, 3024 (1984)
[15] S. Baroni, P. Giannozzi, and A. Testa, Phys. Rev. Lett. 58, 1861 (1987).
[16] S. Baroni, S. de Gironcoli, A. Dal Corso, and P. Gianozzi, Rev. Mod. Phys. 73, 515 (2001).
[17] J. P. Perdew, K. Burke, and M. Ernzerhof, Phys. Rev. Lett. 77, 3865 (1996).
[18] P. Giannozzi, S. Baroni, N. Bonin *et al.*, J of Physics: Condensed Matter 21 395 (2009).
[19] Vanderbilt, D., Phys. Rev. B 41, 7892 (1990).
[20] P. B. Allen, Phys. Rev. B 6 2577 (1972).
[21] G. D. Samolyuk, L. K. Béland, G. M. Stocks and R. E. Stoller, J. Phys.: Condens. Matter 28 175501 (2016).
[22] G. D. Gaspari and B. L. Gyorffy, Phys. Rev. Lett. 28 801-5 (1972).
[23] P. B. Allen, Phys. Rev. B 36 2920 (1987).
[24] Mishin, Y. and Farkas, D. and Mehl, M. J. and Papaconstantopoulos, D. A., Phys. Rev. B 59 3393 (1999).
[25] Bonny, G. and Pasianot, R.C. and Castin, N. and Malerba, L., Philos. Mag. 89 3531 (2009).

Curriculum Vitae

Name: Artur Tamm
Date of birth: 31.08.1985
Citizenship: Estonian
Address: J. Kuperjanovi 20-26, 50409 Tartu, Estonia
Telephone: +37258603338
E-mail: arturt@ut.ee
Marital status: Married

Education:

2010 - ...	Doctoral student in the field of physics, University of Tartu
2008 - 2010	Master of Science (MSc), Solid-state theory, Physics, University of Tartu
2004 - 2008	Bachelor of Science (BSc), Physics, University of Tartu
2001 - 2004	Tartu Hugo Treffner Gymnasium

Employment:

2011 - 2014	Researcher, RadInterfaces EU FP7 Project, University of Tartu

Teaching:

2016	Smart Solutions, University of Tartu
2016	Digital Signal Processing, University of Tartu
2015	Practical Works in Computer Hardware, University of Tartu
2013 - 2015	Computational Physics, University of Tartu
2011 - 2013	Microprocessors, University of Tartu
2010 - 2012	Practical Training, University of Tartu

Collaborations:

2015	Oak Ridge National Laboratory - Roger E. Stoller
2014 - 2015	Los Alamos National Laboratory - Alfredo Caro
2013	Uppsala University - Mattias Klintenberg
2013	Universidad de Oviedo - Roberto Iglesias
2012	Los Alamos National Laboratory - Alfredo Caro

Publications:

- A. Tamm, G. Samolyuk, A. A. Correa, M. Klintenberg, A. Aabloo, A. Caro, The electron-phonon interaction within classical molecular dynamics, *Physical Review B*, (2016) **accepted**.
- A. Tamm, E. Metsanurk, A. Caro, A. Aabloo, M. Klintenberg, Vacancy clusters at the semicoherent CuNb metallic interface, *submitted to Physical Review B.*
- R. E. Stoller, A. Tamm, L. K. Beland, G. D. Samolyuk, G. M. Stocks, A. Caro, L. V. Slipchenko, Yu. N. Osetsky, A. Aabloo, M. Klintenberg, and Y. Wang, The Impact of Short-range Forces on Defect Production from High-energy Collisions, *Journal of Chemical Theory and Computation* **12**, 2871–2879 (2016).
- A. Caro, A. A. Correa, A. Tamm, G. Samolyuk, M. Stocks, Adequacy of damped dynamics to represent the electron-phonon interaction in solids, *Physical Review B* **92**, 144309 (2015).
- A. Tamm, A. Aabloo, M. Klintenberg, M. Stocks, A. Caro, Atomic-scale properties of Ni-based FCC ternary, and quaternary alloys, *Acta Materiala* **99**, 307–312 (2015).
- E. Metsanurk, A. Tamm, A. Caro, A. Aabloo, M. Klintenberg, First-principles study of point defects at a semicoherent interface, *Scientific Reports* **4**, 7567 (2014).
- L. Bläckberg, E. Metsanurk, A. Tamm, A. Aabloo, M. Klintenberg, Molecular dynamics study of Xenon on an amorphous Al_2O_3 surface, *Nuclear Instruments and Methods in Physics Research A* **759**, 10–15 (2014).
- F. Valk, M. Aints, P. Paris, T. Plank, J. Maksimov, A. Tamm, Measurement of collisional quenching rate of nitrogen states $N_2(C^3\Pi_u, \nu = 0)$ and $N_2^+(B_2\Sigma_g^+, \nu = 0)$, *Journal of Physics D: Applied Physics* **43**, 385202 (2010).

Elulookirjeldus

Nimi:	Artur Tamm
Sünniaeg:	31.08.1985
Kodakondsus:	Eesti
Aadress:	J. Kuperjanovi 20-26, 50409 Tartu, Estonia
Telefon:	+37258603338
E-mail:	arturt@ut.ee
Abieluseis:	Abielus

Haridus:

2010 - ...	Doktorant füüsika erialal, Tartu Ülikool
2008 - 2010	Loodusteaduse magistri kraad (MSc), Tahkiseteooria, Füüsika, Tartu Ülikool
2004 - 2008	Loodusteaduse bakalaureus (BSc), Füüsika, Tartu Ülikool
2001 - 2004	Tartu Hugo Treffneri Gümnaasium

Teenistuskäik:

2011 - 2014	Laborant, RadInterfaces EU FP7 Projekt, Tartu Ülikool

Õppetöö:

2016	Nutilahenduste praktikum, Tartu Ülikool
2016	Digitaalne signaalitöötlus, Tartu Ülikool
2015	Arvutiriistvara praktikum, Tartu Ülikool
2013 - 2015	Kompuuterfüüsika, Tartu Ülikool
2011 - 2013	Mikroprotsessorid, Tartu Ülikool
2010 - 2012	Erialapraktika, Tartu Ülikool

Koostööd:

2015	Oak Ridge National Laboratory - Roger E. Stoller
2014 - 2015	Los Alamos National Laboratory - Alfredo Caro
2013	Uppsala University - Mattias Klintenberg
2013	Universidad de Oviedo - Roberto Iglesias
2012	Los Alamos National Laboratory - Alfredo Caro

Publikatsioonid:

- A. Tamm, G. Samolyuk, A. A. Correa, M. Klintenberg, A. Aabloo, A. Caro, The electron-phonon interaction within classical molecular dynamics, *Physical Review B* (2016) **vastu võetud**.

- A. Tamm, E. Metsanurk, A. Caro, A. Aabloo, M. Klintenberg, Vacancy clusters at the semicoherent CuNb metallic interface, *esitatud ajakirja Physical Review B.*

- R. E. Stoller, A. Tamm, L. K. Beland, G. D. Samolyuk, G. M. Stocks, A. Caro, L. V. Slipchenko, Yu. N. Osetsky, A. Aabloo, M. Klintenberg, and Y. Wang, The Impact of Short-range Forces on Defect Production from High-energy Collisions, *Journal of Chemical Theory and Computation* **12**, 2871–2879 (2016).

- A. Caro, A. A. Correa, A. Tamm, G. Samolyuk, M. Stocks, Adequacy of damped dynamics to represent the electron-phonon interaction in solids, *Physical Review B* **92**, 144309 (2015).

- A. Tamm, A. Aabloo, M. Klintenberg, M. Stocks, A. Caro, Atomic-scale properties of Ni-based FCC ternary, and quaternary alloys, *Acta Materiala* **99**, 307–312 (2015).

- E. Metsanurk, A. Tamm, A. Caro, A. Aabloo, M. Klintenberg, First-principles study of point defects at a semicoherent interface, *Scientific Reports* **4**, 7567 (2014).

- L. Bläckberg, E. Metsanurk, A. Tamm, A. Aabloo, M. Klintenberg, Molecular dynamics study of Xenon on an amorphous Al_2O_3 surface, *Nuclear Instruments and Methods in Physics Research A* **759**, 10–15 (2014).

- F. Valk, M. Aints, P. Paris, T. Plank, J. Maksimov, A. Tamm, Measurement of collisional quenching rate of nitrogen states $N_2(C^3\Pi_u, \nu = 0)$ and $N_2^+(B_2\Sigma_g^+, \nu = 0)$, *Journal of Physics D: Applied Physics* **43**, 385202 (2010).

DISSERTATIONES PHYSICAE UNIVERSITATIS TARTUENSIS

1. **Andrus Ausmees.** XUV-induced electron emission and electron-phonon interaction in alkali halides. Tartu, 1991.
2. **Heiki Sõnajalg.** Shaping and recalling of light pulses by optical elements based on spectral hole burning. Tartu, 1991.
3. **Sergei Savihhin.** Ultrafast dynamics of F-centers and bound excitons from picosecond spectroscopy data. Tartu, 1991.
4. **Ergo Nõmmiste.** Leelishalogeniidide röntgenelektronemissioon kiiritamisel footonitega energiaga 70–140 eV. Tartu, 1991.
5. **Margus Rätsep.** Spectral gratings and their relaxation in some low-temperature impurity-doped glasses and crystals. Tartu, 1991.
6. **Tõnu Pullerits.** Primary energy transfer in photosynthesis. Model calculations. Tartu, 1991.
7. **Olev Saks.** Attoampri diapasoonis voolude mõõtmise füüsikalised alused. Tartu, 1991.
8. **Andres Virro.** AlGaAsSb/GaSb heterostructure injection lasers. Tartu, 1991.
9. **Hans Korge.** Investigation of negative point discharge in pure nitrogen at atmospheric pressure. Tartu, 1992.
10. **Jüri Maksimov.** Nonlinear generation of laser VUV radiation for high-resolution spectroscopy. Tartu, 1992.
11. **Mark Aizengendler.** Photostimulated transformation of aggregate defects and spectral hole burning in a neutron-irradiated sapphire. Tartu, 1992.
12. **Hele Siimon.** Atomic layer molecular beam epitaxy of A^2B^6 compounds described on the basis of kinetic equations model. Tartu, 1992.
13. **Tõnu Reinot.** The kinetics of polariton luminescence, energy transfer and relaxation in anthracene. Tartu, 1992.
14. **Toomas Rõõm.** Paramagnetic H^{2-} and F^+ centers in CaO crystals: spectra, relaxation and recombination luminescence. Tallinn, 1993.
15. **Erko Jalviste.** Laser spectroscopy of some jet-cooled organic molecules. Tartu, 1993.
16. **Alvo Aabloo.** Studies of crystalline celluloses using potential energy calculations. Tartu, 1994.
17. **Peeter Paris.** Initiation of corona pulses. Tartu, 1994.
18. **Павел Рубин.** Локальные дефектные состояния в CuO_2 плоскостях высокотемпературных сверхпроводников. Тарту, 1994.
19. **Olavi Ollikainen.** Applications of persistent spectral hole burning in ultrafast optical neural networks, time-resolved spectroscopy and holographic interferometry. Tartu, 1996.
20. **Ülo Mets.** Methodological aspects of fluorescence correlation spectroscopy. Tartu, 1996.
21. **Mikhail Danilkin.** Interaction of intrinsic and impurity defects in CaS:Eu luminophors. Tartu, 1997.

22. **Ирина Кудрявцева.** Создание и стабилизация дефектов в кристаллах KBr, KCl, RbCl при облучении ВУФ-радиацией. Тарту, 1997.
23. **Andres Osvet.** Photochromic properties of radiation-induced defects in diamond. Tartu, 1998.
24. **Jüri Örd.** Classical and quantum aspects of geodesic multiplication. Tartu, 1998.
25. **Priit Sarv.** High resolution solid-state NMR studies of zeolites. Tartu, 1998.
26. **Сергей Долгов.** Электронные возбуждения и дефектообразование в некоторых оксидах металлов. Тарту, 1998.
27. **Kaupo Kukli.** Atomic layer deposition of artificially structured dielectric materials. Tartu, 1999.
28. **Ivo Heinmaa.** Nuclear resonance studies of local structure in $RBa_2Cu_3O_{6+x}$ compounds. Tartu, 1999.
29. **Aleksander Shelkan.** Hole states in CuO_2 planes of high temperature superconducting materials. Tartu, 1999.
30. **Dmitri Nevedrov.** Nonlinear effects in quantum lattices. Tartu, 1999.
31. **Rein Ruus.** Collapse of 3d (4f) orbitals in 2p (3d) excited configurations and its effect on the x-ray and electron spectra. Tartu, 1999.
32. **Valter Zazubovich.** Local relaxation in incommensurate and glassy solids studied by Spectral Hole Burning. Tartu, 1999.
33. **Indrek Reimand.** Picosecond dynamics of optical excitations in GaAs and other excitonic systems. Tartu, 2000.
34. **Vladimir Babin.** Spectroscopy of exciton states in some halide macro- and nanocrystals. Tartu, 2001.
35. **Toomas Plank.** Positive corona at combined DC and AC voltage. Tartu, 2001.
36. **Kristjan Leiger.** Pressure-induced effects in inhomogeneous spectra of doped solids. Tartu, 2002.
37. **Helle Kaasik.** Nonperturbative theory of multiphonon vibrational relaxation and nonradiative transitions. Tartu, 2002.
38. **Tõnu Laas.** Propagation of waves in curved spacetimes. Tartu, 2002.
39. **Rünno Lõhmus.** Application of novel hybrid methods in SPM studies of nanostructural materials. Tartu, 2002.
40. **Kaido Reivelt.** Optical implementation of propagation-invariant pulsed free-space wave fields. Tartu, 2003.
41. **Heiki Kasemägi.** The effect of nanoparticle additives on lithium-ion mobility in a polymer electrolyte. Tartu, 2003.
42. **Villu Repän.** Low current mode of negative corona. Tartu, 2004.
43. **Алексей Котлов.** Оксианионные диэлектрические кристаллы: зонная структура и электронные возбуждения. Tartu, 2004.
44. **Jaak Talts.** Continuous non-invasive blood pressure measurement: comparative and methodological studies of the differential servo-oscillometric method. Tartu, 2004.
45. **Margus Saal.** Studies of pre-big bang and braneworld cosmology. Tartu, 2004.

46. **Eduard Gerškevitš.** Dose to bone marrow and leukaemia risk in external beam radiotherapy of prostate cancer. Tartu, 2005.
47. **Sergey Shchemelyov.** Sum-frequency generation and multiphoton ionization in xenon under excitation by conical laser beams. Tartu, 2006.
48. **Valter Kiisk.** Optical investigation of metal-oxide thin films. Tartu, 2006.
49. **Jaan Aarik.** Atomic layer deposition of titanium, zirconium and hafnium dioxides: growth mechanisms and properties of thin films. Tartu, 2007.
50. **Astrid Rekker.** Colored-noise-controlled anomalous transport and phase transitions in complex systems. Tartu, 2007.
51. **Andres Punning.** Electromechanical characterization of ionic polymer-metal composite sensing actuators. Tartu, 2007.
52. **Indrek Jõgi.** Conduction mechanisms in thin atomic layer deposited films containing TiO_2. Tartu, 2007.
53. **Aleksei Krasnikov.** Luminescence and defects creation processes in lead tungstate crystals. Tartu, 2007.
54. **Küllike Rägo.** Superconducting properties of MgB_2 in a scenario with intra- and interband pairing channels. Tartu, 2008.
55. **Els Heinsalu.** Normal and anomalously slow diffusion under external fields. Tartu, 2008.
56. **Kuno Kooser.** Soft x-ray induced radiative and nonradiative core-hole decay processes in thin films and solids. Tartu, 2008.
57. **Vadim Boltrushko.** Theory of vibronic transitions with strong nonlinear vibronic interaction in solids. Tartu, 2008.
58. **Andi Hektor.** Neutrino Physics beyond the Standard Model. Tartu, 2008.
59. **Raavo Josepson.** Photoinduced field-assisted electron emission into gases. Tartu, 2008.
60. **Martti Pärs.** Study of spontaneous and photoinduced processes in molecular solids using high-resolution optical spectroscopy. Tartu, 2008.
61. **Kristjan Kannike.** Implications of neutrino masses. Tartu, 2008.
62. **Vigen Issahhanjan.** Hole and interstitial centres in radiation-resistant MgO single crystals. Tartu, 2008.
63. **Veera Krasnenko.** Computational modeling of fluorescent proteins. Tartu, 2008.
64. **Mait Müntel.** Detection of doubly charged higgs boson in the CMS detector. Tartu, 2008.
65. **Kalle Kepler.** Optimisation of patient doses and image quality in diagnostic radiology. Tartu, 2009.
66. **Jüri Raud.** Study of negative glow and positive column regions of capillary HF discharge. Tartu, 2009.
67. **Sven Lange.** Spectroscopic and phase-stabilisation properties of pure and rare-earth ions activated ZrO_2 and HfO_2. Tartu, 2010.
68. **Aarne Kasikov.** Optical characterization of inhomogeneous thin films. Tartu, 2010.
69. **Heli Valtna-Lukner.** Superluminally propagating localized optical pulses. Tartu, 2010.

70. **Artjom Vargunin.** Stochastic and deterministic features of ordering in the systems with a phase transition. Tartu, 2010.
71. **Hannes Liivat.** Probing new physics in e+e− annihilations into heavy particles via spin orientation effects. Tartu, 2010.
72. **Tanel Mullari.** On the second order relativistic deviation equation and its applications. Tartu, 2010.
73. **Aleksandr Lissovski.** Pulsed high-pressure discharge in argon: spectroscopic diagnostics, modeling and development. Tartu, 2010.
74. **Aile Tamm.** Atomic layer deposition of high-permittivity insulators from cyclopentadienyl-based precursors. Tartu, 2010.
75. **Janek Uin.** Electrical separation for generating standard aerosols in a wide particle size range. Tartu, 2011.
76. **Svetlana Ganina.** Hajusandmetega ülesanded kui üks võimalus füüsikaõppe efektiivsuse tõstmiseks. Tartu, 2011
77. **Joel Kuusk.** Measurement of top-of-canopy spectral reflectance of forests for developing vegetation radiative transfer models. Tartu, 2011.
78. **Raul Rammula**. Atomic layer deposition of HfO_2 – nucleation, growth and structure development of thin films. Tartu, 2011.
79. **Сергей Наконечный.** Исследование электронно-дырочных и интерстициал-вакансионных процессов в монокристаллах MgO и LiF методами термоактивационной спектроскопии. Тарту, 2011.
80. **Niina Voropajeva.** Elementary excitations near the boundary of a strongly correlated crystal. Tartu, 2011.
81. **Martin Timusk.** Development and characterization of hybrid electro-optical materials. Tartu, 2012, 106 p.
82. **Merle Lust.** Assessment of dose components to Estonian population. Tartu, 2012, 84 p.
83. **Karl Kruusamäe.** Deformation-dependent electrode impedance of ionic electromechanically active polymers. Tartu, 2012, 128 p.
84. **Liis Rebane.** Measurement of the $W \to \tau\nu$ cross section and a search for a doubly charged Higgs boson decaying to τ-leptons with the CMS detector. Tartu, 2012, 156 p.
85. **Jevgeni Šablonin.** Processes of structural defect creation in pure and doped MgO and NaCl single crystals under condition of low or super high density of electronic excitations. Tartu, 2013, 145 p.
86. **Riho Vendt**. Combined method for establishment and dissemination of the international temperature scale. Tartu, 2013, 108 p.
87. **Peeter Piksarv.** Spatiotemporal characterization of diffractive and non-diffractive light pulses. Tartu, 2013, 156 p.
88. **Anna Šugai.** Creation of structural defects under superhigh-dense irradiation of wide-gap metal oxides. Tartu, 2013, 108 p.
89. **Ivar Kuusik.** Soft X-ray spectroscopy of insulators. Tartu, 2013, 113 p.
90. **Viktor Vabson**. Measurement uncertainty in Estonian Standard Laboratory for Mass. Tartu, 2013, 134 p.

91. **Kaupo Voormansik.** X-band synthetic aperture radar applications for environmental monitoring. Tartu, 2014, 117 p.
92. **Deivid Pugal.** hp-FEM model of IPMC deformation. Tartu, 2014, 143 p.
93. **Siim Pikker.** Modification in the emission and spectral shape of photostable fluorophores by nanometallic structures. Tartu, 2014, 98 p.
94. **Mihkel Pajusalu**. Localized Photosynthetic Excitons. Tartu, 2014, 183 p.
95. **Taavi Vaikjärv.** Consideration of non-adiabaticity of the Pseudo-Jahn-Teller effect: contribution of phonons. Tartu, 2014, 129 p.
96. **Martin Vilbaste.** Uncertainty sources and analysis methods in realizing SI units of air humidity in Estonia. Tartu, 2014, 111 p.
97. **Mihkel Rähn.** Experimental nanophotonics: single-photon sources- and nanofiber-related studies. Tartu, 2015, 107 p.
98. **Raul Laasner.** Excited state dynamics under high excitation densities in tungstates. Tartu, 2015, 125 p.
99. **Andris Slavinskis.** EST Cube-1 attitude determination. Tartu, 2015, 104 p.
100. **Karlis Zalite**. Radar Remote Sensing for Monitoring Forest Floods and Agricultural Grasslands. Tartu, 2016, 124 p.
101. **Kaarel Piip.** Development of LIBS for *in-situ* study of ITER relevant materials. Tartu, 2016, 93 p.
102. **Kadri Isakar.** ^{210}Pb in Estonian air: long term study of activity concentrations and origin of radioactive lead. Tartu, 2016, 107 p.